Modeling core excitations and preserving spin symmetry in molecular systems

Patrick J. Lestrange

A dissertation
submitted in partial fulfillment of the
requirements for the degree of

Doctor of Philosophy

University of Washington

2017

Reading Committee:

Xiaosong Li, Chair

David J. Masiello

Stefan Stoll

Program Authorized to Offer Degree:
Chemistry

University of Washington

Abstract

Modeling core excitations and preserving
spin symmetry in molecular systems

Patrick J. Lestrange

Chair of the Supervisory Committee:
Professor Xiaosong Li
Department of Chemistry

This dissertation details work in two general areas: the modeling of X-ray absorption spectroscopy (XAS) and the spin symmetry in molecular simulations. The first chapter introduces electronic structure theory (EST) techniques used in the later sections and XAS. The following chapter discusses calibration of the energy-specific time-dependent density functional theory approach for modeling core excitations and proposes appropriate functionals and basis sets. The time-resolved X-ray absorption of a nickel porphyrin system is also investigated to understand the relaxation pathway following an initial excitation. The very accurate energy-specific equation of motion coupled cluster approach is introduced next and a solution to the origin dependence problem for quadrupole-allowed transitions is investigated. The final two chapters focuses on the issue of spin symmetry in EST and uses two alternative approaches to preserve this as a symmetry of a molecular wave function. The system can be constrained to a particular spin symmetry in the single-determinant framework and then additional electron correlation can be included through the configuration interaction method. A time-dependent extension of this approach and its application to modeling linear and nonlinear electric properties is presented. Spin symmetry can also be restored to broken symmetry Slater determinants by using a projection operator. An efficient implementation of projected Hartree-Fock is presented in detail.

TABLE OF CONTENTS

LIST OF FIGURES

Figure Number Page

LIST OF TABLES

GLOSSARY

AO: Atomic Orbital

CC: Coupled Cluster

CI: Configuration Interaction

CPP: Complex Polarization Propagator

CSF: Configuration State Function

DFT: Density Function Theory

EDA: Electric Dipole Approximation

EOM: Equation-of-motion

ES: Energy-specific

FCI: Full Configuration Interaction

GHF: Generalized Hartree-Fock

GUGA: Graphical Unitary Group Approach

HF: Hartree-Fock

KS: Kohn-Sham

LCAO: Linear Combination of Atomic Orbitals

LR: Linear Response

MBPT: Many-body Perturbation Theory

MO: Molecular Orbital

MPPT: Møller-Plesset Perturbation Theory

NO: Natural Orbital

OAO: Orthonormal Atomic Orbital

PHF: Projected Hartree-Fock

REW: Restricted Excitation Window

RHF: Restricted Hartree-Fock

ROHF: Restricted open-shell Hartree-Fock

RT: Real-time

SCF: Self-consistent Field

SD: Slater Determinant

SGHF: Spin-projected Generalized Hartree-Fock

TDDFT: Time-dependent Density Functional Theory

TDHF: Time-dependent Hartree-Fock

TDKS: Time-dependent Kohn-Sham

TDSE: Time-dependent Schödinger Equation

TISE: Time-independent Schödinger Equation

UHF: Unrestricted Hartree-Fock

XANES: X-ray Absorption Near-edge Structure

XAS: X-ray Absorption Spectroscopy

ACKNOWLEDGMENTS

Completing a Ph.D. is only possible through the personal and academic support of others. I'd like to thank the many people who have helped me throughout my graduate career.

It's difficult to express the extent of my gratitude to my advisor, Xiaosong Li. His enthusiasm for science is amazingly infectious and has helped sustain me during difficult stretches. I cannot count the number of times I went to Xiaosong's office dejected and dispirited only to leave enthusiastic and excited about a project again. I could never quite figure out how he did it, but it was marvelous. Thank you, Xiaosong.

The Li research group is full of talented scientists that have taught me much over the years. I'm grateful to them all in large and small ways. Craig Chapman, Sean Fischer, Joseph May, and Feizhi Ding advised me through the early years. Josh Goings and David Lingerfelt tolerated me for five years and helped me struggle through difficult times and projects. David Williams-Young allowed me to bounce (sometimes good) ideas off him and has been an invaluable resource to me. Alessio Petrone, Greta Donati, and Franco Egidi have been fantastic advisors and colleagues. I've learned a lot working with the younger students as well. Thank you to Hongbin Liu, Joe Kasper, J. Radler, Shichao Sun, Torin Stetina, and all the people I've been foolish enough to leave out.

I made a terrible first impression on my undergraduate advisor, Jim Foresman. During the second year of my undergraduate career I either slept or played computer games through one of his classes. Despite showing myself to be a less than ideal student, Jim was good enough to give me another chance and took me into his research group. He taught me how to think critically about a problem and ask the appropriate questions to frame a research project. Every now and then I had enough sense to pay attention, but in retrospect that

certainly didn't happen often enough.

I've also been fortunate enough to have the help and guidance of many people outside of my current and former institutions. The researchers at Gaussian (past and present): Mike Frisch, Gary Trucks, Giovanni Scalmani, Marco Caricato, Hrant Hratchian, Jason Sonnenberg, and Fernando Clemente have taught me so much about electronic structure theory and how to think through complicated problems. The generous help from Mark Hoffman and Carlos Jiménez-Hoyos was greatly appreciated and helped spur along difficult projects. I was also lucky enough to have the opportunity to work with Jeppe Olsen in Aarhus. He took a chance on an unknown student and allowed me to benefit from his wealth of experience for which I am very grateful. Thank you all for your time and your help.

I must also thank my family and friends: Mary, Megan, Margaret, Kayla, Thomas, and all the others. Your endless support and encouragement has helped drive me over the years.

And lastly, thank you, Elise. You've tolerated a very stressed graduate student for several years. I can't tell you how much your love and support mean to me.

DEDICATION

For my mother, Mary.

Thanks for giving me the chance to do this.

PREFACE

Scientific research, like all great endeavors, is a collaborative effort. As the work presented in the following chapters is the result of combined efforts with other researchers, I'd like to highlight my contributions to each section.

In Chapter 2, I focus on calibrating energy-specific time-dependent density functional theory to determine which functionals and basis sets are appropriate to model core excitations. This approach was developed by Wenkel Liang to directly model higher energy excitations, but its ability to describe core excitations had not yet been determined.[1] New approximations in density functional theory are always calibrated against a set of experimental observables. The accuracy of a method always needs to be reevaluated if it is to be applied to a phenomena outside of its training data set. My role was to collect a set of experimental X-ray absorption spectra and evaluate the ability of different density functionals to reproduce them, so this approach could be applied with more confidence in the future.

This chapter also describes a collaborative project with experimentalists at Northwestern University and Argonne National Laboratory. We studied the relaxation dynamics of an excited Ni porphyrin with X-ray transient absorption. Several steps in the relaxation pathway had been identified, but additional evidence to characterize each intermediate state was necessary to make more definitive assignments. My role was to model the X-ray absorption spectra of the proposed steps in the relaxation pathway to compare with the experiment. I was able to show which signatures corresponded to different intermediate structures and provide a rational for how the spectra changed over time. Many of the experimental details are left out of this section and readers are referred to Ref. 2 if interested.

Chapter 3 highlights the development of energy-specific equation-of-motion coupled clus-

ter theory. The development of this technique was motivated by my previous work on X-ray absorption spectra and the desire for more accurate approaches. The first author of the resulting paper, Bo Peng, implemented the method while I acted in an advisory role throughout the process. My contribution was to developing benchmarks to compare our new method against and contrast it against other recently developed techniques.

The following section focuses on a more complete description of the light-matter interaction necessary to describe certain high energy excitations. This work built off of the initial presentation of the second-order oscillator strength expression by Bernadotte, Atkins, and Jacob.[3] My work further highlights the utility of their approach by showing the consequences and failings of another commonly used oscillator strength expression. I also present the first instance of negative oscillator strengths using the expression raising doubts on its utility in the future.

Chapter 4 shows how to extract linear and nonlinear properties from time-dependent configuration interaction simulations. I implemented both time-dependent and time-independent versions of the graphical unitary group approach to configuration interaction. This section illustrates how to adiabatically turn on the interaction between an oscillating electric field and an electronic wave function. It also compares different truncations of the configuration interaction space and shows how this affects extracted physical properties.

The final chapter details the implementation spin-projected generalized Hartree-Fock in the Chronus Quantum software package. My implementation has notable improvements over previous implementations including reduced memory requirements and overall efficiency. This is an important step toward developing more advanced projected techniques.

Chapter 1

BASIS THEORIES AND CONCEPTS

1.1 Electronic Structure Theory

As the name implies, electronic structure theory focuses on describing the electrons in a molecular system. In order to focus on the electronic degrees of freedom, they must be separated from the nuclear degrees of freedom. This is done by invoking the Born-Oppenheimer approximation where the nuclei are treated as a static frame that electrons move around since they are so much heavier and slower than electrons. This approximation leads to the non-relativistic time-independent electronic Schrödinger equation (TISE)

$$\hat{H}\Psi = E\Psi \tag{1.1}$$

where Ψ is the electronic wave function, $\hat{H}$ is the non-relativistic electronic Hamiltonian, and E is the electronic energy. The electronic Hamiltonian is written as

$$\hat{H} = -\frac{1}{2}\sum_{i}\nabla_i^2 - \sum_{iA}\frac{Z_A}{r_{iA}} + \sum_{i\neq j}\frac{1}{r_{ij}} + \sum_{AB}\frac{Z_A Z_B}{r_{AB}} \tag{1.2}$$

where the first term describes the kinetic-energy of the electrons, the second term the Coulombic attraction between electrons and nuclei, the third term is Coulombic repulsion between electrons, and the final term in the Coulombic repulsion between nuclei. The indices i, j denote different electrons and A, B denote different nuclei. The nuclear repulsion term is always a constant for static nuclear point charges used in the Born-Oppenheimer approximation, so it's not necessary to discuss it further in the context of electronic structure theory.

1.1.1 Hartree-Fock Theory

Hartree-Fock Theory is a centrally important approximation in EST. Its simplicity helps to develop intuition about molecular systems in terms of orbital theory and it provides a useful starting point for more accurate calculations. A Hartee-Fock (HF) wave function is expressed as an antisymmetrized product of single electron wave functions, known as a Slater determinant

$$\Phi_{HF} = \frac{1}{\sqrt{N!}} \begin{vmatrix} \psi_1(\mathbf{x}_1) & \psi_2(\mathbf{x}_1) & \cdots & \psi_N(\mathbf{x}_1) \\ \psi_1(\mathbf{x}_2) & \psi_2(\mathbf{x}_2) & \cdots & \psi_N(\mathbf{x}_2) \\ \vdots & \vdots & \ddots & \vdots \\ \psi_1(\mathbf{x}_N) & \psi_2(\mathbf{x}_N) & \cdots & \psi_N(\mathbf{x}_N) \end{vmatrix} \tag{1.3}$$

The HF ground-state energy is determined by minimizing the energy functional $E_0 = \langle \Phi_{HF} | \hat{H} | \Phi_{HF} \rangle$ with the constraint that the orbitals remain orthogonal to each other. This is done by setting the linear variation in the following Lagrangian to be zero

$$\mathcal{L} = \langle \Phi_{HF} | \hat{H} | \Phi_{HF} \rangle - \sum_{ij} \epsilon_{ij} (\langle \psi_i \mid \psi_j \rangle - \delta_{ij}) \tag{1.4}$$

where ϵ_{ij} are Lagrange multipliers and $\langle \psi_i \mid \psi_j \rangle$ is the overlap between two orbitals. Evaluating the conditions that make the variation zero leads to a set of one-electron eigenvalue problems

$$\hat{f}(\mathbf{x}_1)\psi_i(\mathbf{x}_1) = \epsilon_i \psi_i(\mathbf{x}_1) \tag{1.5}$$

where the Lagrange multipliers are now diagonal following a unitary transformation and represent spin orbital energies.

The Fock operator introduced above describes the interaction of an electron with the surrounding nuclei and an averaged field due to the other electrons. It is often referred to as a mean-field operator for this reason.

$$\hat{f}(\mathbf{x}_1) = \hat{h}(\mathbf{x}_1) + \hat{J}(\mathbf{x}_1) - \hat{K}(\mathbf{x}_1) \tag{1.6}$$

where the core Hamiltonian $\hat{h}$ is a one-electron operator describing the kinetic-energy of the electron and its attraction to the surrounding nuclei

$$\hat{h}(\mathbf{x}_1) = -\frac{1}{2}\nabla_1^2 - \sum_A \frac{Z_A}{r_{1A}} \tag{1.7}$$

where Z_A is the charge of nucleus A and r_{1A} is the separation between the electron and the nucleus. The Coloumb and exchange operators describe the interaction of an electron with the other electrons in the system

$$\hat{J}(\mathbf{x}_1)\psi_k(\mathbf{x}_1) = \sum_{j=1}^{N} \left[\int d\mathbf{x}_2 \psi_j^*(\mathbf{x}_2) r_{12}^{-1} \psi_j(\mathbf{x}_2) \right] \psi_k(\mathbf{x}_1) \tag{1.8}$$

$$\hat{K}(\mathbf{x}_1)\psi_k(\mathbf{x}_1) = \sum_{j=1}^{N} \left[\int d\mathbf{x}_2 \psi_j^*(\mathbf{x}_2) r_{12}^{-1} \psi_k(\mathbf{x}_2) \right] \psi_j(\mathbf{x}_1) \tag{1.9}$$

Different constraints can be placed on the spin orbitals to restrict the form of the Hartree-Fock problem. The spin orbitals $\psi(\mathbf{x})$ have a spatial $\phi(\mathbf{r})$ and a spin component $\sigma(\omega)$, which can be either α or β or a combination of the two. Restricted HF (RHF) keeps the spatial component the same regardless of the spin component.

$$\text{RHF} : \psi(\mathbf{x}) = \begin{cases} \phi(\mathbf{r})\alpha(\omega) \\ \phi(\mathbf{r})\beta(\omega) \end{cases} \tag{1.10}$$

Restricted open-shell HF (ROHF) enforces the same constraints for doubly occupied orbitals, but not for those that are singly occupied.[4] Unrestricted HF (UHF) relaxes this constraint to allow α and β electrons to have different spatial components[5]

$$\text{UHF} : \psi(\mathbf{x}) = \begin{cases} \phi^\alpha(\mathbf{r})\alpha(\omega) \\ \phi^\beta(\mathbf{r})\beta(\omega) \end{cases} \tag{1.11}$$

The UHF orbitals are still constrained to have one of two spin projections along the z-axis. This constraint is relaxed for Generalized HF (GHF)[6] where each spin orbital is a linear combination of α and β

$$\text{GHF} : \psi(\mathbf{x}) = \phi^\alpha(\mathbf{r})\alpha(\omega) + \phi^\beta(\mathbf{r})\beta(\omega) \tag{1.12}$$

These molecular orbitals are often described as linear combinations of atomic-orbitals (LCAO). The spatial part of the spin orbitals are expanded in a finite set of atomic-orbital (AO) basis functions

$$\phi(\mathbf{r})_k = \sum_{\mu=1}^{M} C_{\mu k}\chi_\mu(\mathbf{r}) \tag{1.13}$$

where $C_{\mu k}$ are molecular orbitals (MO) coefficients and $\chi_\mu(\mathbf{r})$ are the AO basis functions. The basis functions are usually Gaussian functions, but in some software packages they are Slater-type functions or plane waves.

The stationary condition of Equation (1.4) can be satisfied by solving the generalized eigenvalue problem

$$\mathbf{FC} = \mathbf{SC}\boldsymbol{\epsilon} \tag{1.14}$$

where $\mathbf{F}$ is the Fock matrix in the AO basis, $\mathbf{C}$ are the MO coefficients, and $\mathbf{S}$ is the overlap matrix between basis functions

$$S_{\mu\nu} = \langle \mu \,|\, \nu \rangle \tag{1.15}$$

For GHF the Fock matrix can be spin-blocked to give the form

$$\mathbf{F} = \begin{pmatrix} \mathbf{F}^{\alpha\alpha} & \mathbf{F}^{\alpha\beta} \\ \mathbf{F}^{\beta\alpha} & \mathbf{F}^{\beta\beta} \end{pmatrix} \tag{1.16}$$

where each block matrix is defined as

$$\mathbf{F}^{\sigma\tau} = \mathbf{h}^{\sigma\tau} + \delta_{\sigma\tau}[\mathbf{J}^{\alpha\alpha} + \mathbf{J}^{\beta\beta}] - \mathbf{K}^{\sigma\tau} \tag{1.17}$$

The Coulomb and exchange matrix elements are defined as

$$J^{\sigma\sigma}_{\mu\nu} = \sum_{\lambda\kappa} P^{\sigma\sigma}_{\lambda\kappa} \langle \mu\nu \,|\, \kappa\lambda \rangle \tag{1.18}$$

$$K^{\sigma\tau}_{\mu\nu} = \sum_{\lambda\kappa} P^{\sigma\tau}_{\lambda\kappa} \langle \mu\lambda \,|\, \kappa\nu \rangle \tag{1.19}$$

$$\langle \mu\nu \,|\, \kappa\lambda \rangle = \int d\mathbf{x}_1 d\mathbf{x}_2 \psi^*_\mu(\mathbf{x}_1)\psi_\nu(\mathbf{x}_1) r_{12}^{-1} \psi^*_\kappa(\mathbf{x}_2)\psi_\lambda(\mathbf{x}_2) \tag{1.20}$$

The density matrix in the above expressions is constructed from the MO coefficients

$$\mathbf{P} = \mathbf{C}_{\text{occ}}\mathbf{C}_{\text{occ}}^{\dagger} \tag{1.21}$$

where $\mathbf{C}_{\text{occ}}$ are the MO coefficients for the occupied orbitals.

Equation (1.14) is a nonlinear problem since the Fock matrix depends on the MO coefficients and they are determined by diagonalizing the Fock matrix. This equation must be solved iteratively until the MO coefficients used to form the Fock matrix are the same as those obtained from diagonalizing it. At this point we will have reached self consistency, so the HF method is often referred to as a self-consistent field (SCF) method. UHF and RHF are special cases of GHF where the off-diagonal blocks of the Fock matrix are zero for UHF and $\mathbf{F}^{\beta\beta} = \mathbf{F}^{\alpha\alpha}$ for RHF.

1.1.2 Electron Correlation

The Hartree-Fock method embodies many desirable aspects in a molecular theory. However, due to its description of electron repulsion through a mean-field potential, the HF ground-state energy is still far from the exact non-relativistic ground-state energy in the basis used. The difference between these two energies is referred to as the "correlation energy". Without a description that captures some or all of this correlation energy, we cannot quantitatively and in many cases cannot even qualitatively describe molecular systems.

The deficiencies of HF theory are addressed by so-called post-SCF methods.[5,7] These approaches add in explicit two-electron interactions that are missing in the mean-field description of HF. The simplest approach in this category is the configuration interaction (CI) method. This approach describes the electronic wave function as a linear combination of the HF ground-state determinant and other excited determinants.

$$\Psi = \Phi^{\text{HF}} + \sum_i c_i \Phi_i \tag{1.22}$$

If all excited determinants in a given bases are included in this description of the wave function, the exact solution in that basis is obtained. This is the so-called full configuration

interaction (FCI) method. Unfortunately, the number of excited determinants grows exponentially with the size of the system, so this approach is impractical for all but very small systems. The expansion in Equation (1.22) usually includes only certain classes of excited determinants to keep the CI space from growing too large. This approach will be investigated further in Chapter 4.

Electron correlation can also be added into our description of an electronic system with Many-body Perturbation Theory (MBPT). The Hamiltonian is partitioned into a zero-order part $\hat{H}_0$ and a perturbation $\hat{V}$.

$$\hat{H} = \hat{H}_0 + \lambda\hat{V} \tag{1.23}$$

where we have introduced an ordering parameter λ. The wave function and the energy are also expanded in different orders

$$\Psi = \Psi^{(0)} + \lambda\Psi^{(1)} + \lambda^2\Psi^{(2)} + \dots \tag{1.24}$$

$$E = E^{(0)} + \lambda E^{(1)} + \lambda^2 E^{(2)} + \dots \tag{1.25}$$

These expanded quantities are then combined in the time-independent Schödinger equation (Equation (1.1)) and collected in like orders of λ. In perturbation theory, the zero-order part can usually be solved very easily, but solving the higher-order expressions is usually more involved. The most common form of MBPT used in quantum chemistry is Møller-Plesset Perturbation Theory (MPPT). Different orders of MPPT are denoted as MPn where n is the order in the expansion. HF is recovered as MP1 in Møller-Plesset Perturbation Theory and $\Psi^{(0)}$ is the HF wave function.

Coupled cluster (CC) theory is particularly accurate post-SCF method that describes the electronic wave function with an exponential ansatz[8]

$$\Psi = e^{\hat{T}}\Phi^{\mathrm{HF}} \tag{1.26}$$

The $\hat{T}$ operator is a cluster operator that creates excited Slater determinants. The exponential operator is usually expanded in a series and also truncated at some level of excitation.

This method is closely related to the Møller-Plesset series involving many terms similar to those in MPPT. This technique and its connection to MPPT will be discussed further in Section 3.1.

1.1.3 Density Functional Theory

Density functional theory (DFT) is based on proofs by Hohenberg and Kohn that show that the ground-state electronic energy is completely determined by the electron density.[9] The electron density depends on three coordinates independent of the size of the molecular system. This is in contrast to the above wave function approaches with contain $4N$ variables, where N is the number of electrons in the system. In principle, it offers and affordable exact solution to the Schrödinger equation. In practice, the exact density functional is not known so approximations to this functional must be used instead.

The Thomas-Fermi-Dirac form of DFT was very successful at calculating the energy of a uniform electron gas. However, this approach poorly describes kinetic-energy and exchange in molecular systems. Common density functional approximations build on Kohn and Sham's introduction of orbitals to DFT, which dramatically improves the description of the kinetic-energy.

$$T_S = -\frac{1}{2}\sum_{i}^{N} \langle \psi_i | \nabla^2 | \psi_i \rangle \tag{1.27}$$

where the subscript S denotes that the kinetic-energy is calculated from a Slater determinant. Kohn and Sham also introduced an exchange-correlation term to account for errors in the kinetic-energy term and missing electron correlation.

$$E_{\mathrm{DFT}}[\rho] = T_S[\rho] + E_{ne}[\rho] + J[\rho] + E_{xc}[\rho] \tag{1.28}$$

where $E_{ne}[\rho]$ is the nuclear-electron attraction and $J[\rho]$ is Coulombic electron repulsion

$$E_{ne}[\rho] = \sum_{A} \int d\mathbf{x}\, \frac{Z_A \rho(\mathbf{x})}{|\mathbf{R}_A - \mathbf{x}|} \tag{1.29}$$

$$J[\rho] = \frac{1}{2} \int \int d\mathbf{x} d\mathbf{x}'\, \frac{\rho(\mathbf{x})\rho(\mathbf{x}')}{|\mathbf{x} - \mathbf{x}'|} \tag{1.30}$$

The Kohn-Sham (KS) form of DFT is solved in much the same way as HF. A Lagrangian is formed with the constraint that the orbitals remain orthogonal to each other.

$$\mathcal{L} = E_{\mathrm{DFT}}[\rho] - \sum_{ij} \epsilon_{ij}(\langle \psi_i \mid \psi_j \rangle - \delta_{ij}) \tag{1.31}$$

The stationary condition that makes the variation in this Lagrangian zero leads to

$$\hat{f}^{KS}\psi_i = \epsilon_i \psi_i \tag{1.32}$$

where a unitary transformation has made the Lagrange multipliers diagonal. The Kohn-Sham operator can now be defined as

$$\hat{f}^{KS}(\mathbf{x}) = \hat{h}(\mathbf{x}) + \int d\mathbf{x}' \, \frac{\rho(\mathbf{x}')}{|\mathbf{x} - \mathbf{x}'|} + v_{xc}(\mathbf{x}) \tag{1.33}$$

where

$$v_{xc}(\mathbf{x}) = \frac{\partial E_{xc}[\rho]}{\partial \rho(\mathbf{x})} \tag{1.34}$$

If the exact functional were known, DFT would be an elegant means of modeling molecular systems. There have been many approximations developed within KS theory to address different problems. When working on a new problem, one must determine whether there is an appropriate functional approximation that can be used to model a particular phenomenon. We will talk about this process in more detail in Section 2.1.

1.1.4 Time-dependent Quantum Mechanics

The previous sections focused on approximations to the time-independent Schödinger equation. The time-dependent Schödinger equation (TDSE) is written as

$$i\frac{\partial}{\partial t}\Psi(\mathbf{x}, t) = \hat{H}(t)\Psi(\mathbf{x}, t) \tag{1.35}$$

and can be approximated using the same wave function ansatz used for the TISE.

The working equations for time-dependent Hartree-Fock (TDHF) are determined by invoking the time-dependent variational principle where the Lagrangian is defined as

$$\mathcal{L} = \langle \Phi_{HF} | \, \hat{H} - i\frac{\partial}{\partial t} \, | \Phi_{HF} \rangle - \sum_{ij} \epsilon_{ij} (\langle \psi_i \mid \psi_j \rangle - \delta_{ij}) \tag{1.36}$$

where the coefficients enforce that the occupied orbitals remain orthonormal through the propagation. It is the variation in this functional that will determine the time-dependent equations. Evaluating the stationary conditions of the above Lagrangian leads to the following time-dependent equation

$$i\mathbf{S}\dot{\mathbf{P}}\mathbf{S} = \mathbf{FPS} - \mathbf{SPF} \tag{1.37}$$

where the dot denotes a time derivative. This is the time-dependent HF equation in the atomic-orbital basis, but this expression is more commonly written in the orthonormal basis. This is done by defining a transformation matrix ($\mathbf{V} = \mathbf{S}^{1/2}$ for the Löwdin transformation)

$$\mathbf{P}' = \mathbf{VPV}^T \tag{1.38}$$

$$\mathbf{F}' = \mathbf{V}^{-T}\mathbf{FV}^{-1} \tag{1.39}$$

The TDHF equation can now be written in the common Liouville-von Neumann form

$$i\dot{\mathbf{P}}' = [\mathbf{F}', \mathbf{P}'] \tag{1.40}$$

There are many different schemes to propagate this equation in time, but those techniques are beyond the scope of this work.

Density functional theory can also be extended to the time domain using the Runge-Gross theorem. This states that there is a one-to-one correspondence between the external time-dependent potential acting on a system and the electron density. This allows us to construct a similar Lagrangian DFT to derive the time-dependent Kohn-Sham (TDKS) equation

$$i\mathbf{S}\dot{\mathbf{P}}\mathbf{S} = \mathbf{KPS} - \mathbf{SPK} \tag{1.41}$$

where $\mathbf{K}$ is the Kohn-Sham matrix. The Liouville-von Neumann form of the TDKS equation is

$$i\dot{\mathbf{P}}' = [\mathbf{K}', \mathbf{P}'] \tag{1.42}$$

which can be solved in the same way as the TDHF equation. Just like in the time-independent case, the time-dependent exchange-correlation potential is not known. It is often approximated to be the same as the ground-state exchange-correlation functional, known as the adiabatic approximation.

1.1.5 Response Theory

While Equations (1.40) and (1.42) can be solved explicitly in the time domain, it is often advantageous to linearize and transform them to the frequency domain. One approach is to first expand the time-dependent density and Fock (or Kohn-Sham) matrices in a perturbative series

$$\mathbf{P}(t,\lambda) = \mathbf{P}^{(0)} + \lambda_\mu \frac{\partial \mathbf{P}}{\partial \lambda_\mu}\bigg|_{\lambda=0} + \frac{\lambda_\mu \lambda_\nu}{2} \frac{\partial \mathbf{P}}{\partial^2 \lambda_\mu \lambda_\nu}\bigg|_{\lambda=0} + \dots \tag{1.43}$$

$$\mathbf{F}(t,\lambda) = \mathbf{F}^{(0)} + \lambda_\mu \frac{\partial \mathbf{F}}{\partial \lambda_\mu}\bigg|_{\lambda=0} + \frac{\lambda_\mu \lambda_\nu}{2} \frac{\partial \mathbf{F}}{\partial^2 \lambda_\mu \lambda_\nu}\bigg|_{\lambda=0} + \dots \tag{1.44}$$

Each order in the series can then be Fourier transformed to the frequency domain and combined again in Equations (1.40) and (1.42) to collect the different orders of response. The stationary condition the SCF equations is recovered as well as the linear-response equation

$$0 = [\mathbf{F}^{(0)}, \mathbf{P}^{(0)}] \tag{1.45}$$

$$\omega_\mu \mathbf{P}^{(\mu)} = [\mathbf{F}^{(0)}, \mathbf{P}^{(\mu)}] + [\mathbf{F}^{(\mu)}, \mathbf{P}^{(0)}] \tag{1.46}$$

where $\mathbf{P}^{(\mu)}$ and $\mathbf{F}^{(\mu)}$ are the Fourier transformed first-derivatives of the density and Fock (Kohn-Sham) matrices. The linear-response equation is commonly represented in the eigenmode Casida form where excitation energies ω are obtained as solutions to the non-Hermitian

eigenvalue equation:[10–12]

$$\begin{pmatrix} \mathbf{A} & \mathbf{B} \\ \mathbf{B} & \mathbf{A} \end{pmatrix} \begin{pmatrix} \mathbf{X} \\ \mathbf{Y} \end{pmatrix} = \omega \begin{pmatrix} \mathbf{1} & \mathbf{0} \\ \mathbf{0} & \mathbf{-1} \end{pmatrix} \begin{pmatrix} \mathbf{X} \\ \mathbf{Y} \end{pmatrix} \tag{1.47}$$

where the matrix elements of $\mathbf{A}$ and $\mathbf{B}$ are given by:

$$A_{ia,jb} = \delta_{ij}\delta_{ab}(\epsilon_a - \epsilon_i) + (ia|jb) - \alpha(ib|ja) + (ia|f_{xc}|jb) \tag{1.48}$$

$$B_{ia,jb} = (ia|bj) - \alpha(ij|ba) + (ia|f_{xc}|bj) \tag{1.49}$$

Occupied and virtual molecular orbitals (MO) are indexed by i, j and a, b respectively. The scaling factor α in front of the HF exchange integral has a value between 0 and 1 for hybrid functionals and zero for pure density functionals. Solving the system of linear equations as shown in Eq. (1.47) yields the first-order electron density responses $\mathbf{X}$ and $\mathbf{Y}$.

1.2 X-ray Absorption Spectroscopy

X-ray absorption spectroscopy (XAS) has become an ever more present tool for interrogating the electronic and nuclear structure of molecules and condensed matter. This is mainly due to recent advances that have greatly improved its temporal and spectroscopic resolution.[13–17] XAS is particularly powerful due to its ability to probe both the electronic structure (e.g. oxidation state) and the local geometry of the absorbing atom in a single experiment. This technique excites core electrons to weakly bound orbitals or to the continuum. It is often referred to as an "element-specific" technique since the energies of core electrons are strongly dependent on the nuclear charge of the absorbing atom. This makes it possible to isolate and study the local environment around a metal center separate from transitions on surrounding ligands.

X-ray absorption spectra feature a large absorption edge corresponding to the ionization of core electrons. The spectrum is usually partitioned into the region preceding the edge, the near-edge X-ray absorption fine structure (NEXAFS), and the region following the edge, the extended X-ray absorption fine structure (EXAFS).[18] The NEXAFS region, also known

as X-ray absorption near-edge structure (XANES) for heavier elements, contains excitations to bound electronic states close to the ionization potential. The EXAFS region contains oscillatory features corresponding to the scattering of a photoelectron by the surrounding nuclei. Because XAS includes excitations to both bound and continuum states, information about both the electronic and nuclear structure of the system can be obtained in one experimental setup. As a result, X-ray spectroscopy has become increasingly prevalent in the surface science community,[19] as well as in the bioinorganic[20] and thin-film sciences.[21]

1.2.1 Modeling XAS

Both valence and core excitations are induced by coupling a many-body wave function to an electric field. In this way, they are very similar phenomena except that valence excitations are induced by laser pulses of a few or tens of eV, but core excitations require pulses of hundreds or thousands of eV. This difference determines which numerical approaches are tractable for modeling XAS and causes several approximations valid for valence excitations to breakdown.

The eigenmode decomposition form of linear-response TDDFT is possibly the most common method for modeling electronic absorption spectra. Most schemes to iteratively diagonalize Equation (1.47) require solving for lower-energy solutions first before obtaining higher-energy solutions. This is problematic for core excitations because they are particularly high in energy and there are very many lower-energy solutions. Frequency-dependent linear-response avoids this issue since the dynamic polarizability is determined for discrete frequencies and does not depend on solutions at other frequencies. However, the eigenmode form is useful for characterize electronic excited states in more detail. Many techniques which can directly model transitions within a particular energy range have been developed recently. We will detail the calibration of our energy-specific TDDFT (ES-TDDFT) and the development of the energy-specific equation-of-motion coupled cluster (ES-EOMCC) technique in Section 2.1 and Section 3.1 respectively.

The electromagnetic field is often treated as a classical plane wave when coupling to a

quantum mechanical system. This interaction is usually described by expanding the plane wave in a series and truncating at first order

$$\exp(\mathrm{i}\,\mathbf{k}\cdot\mathbf{r}_i) = 1 + \mathrm{i}\,\mathbf{k}\cdot\mathbf{r}_i + \frac{1}{2}(\mathrm{i}\,\mathbf{k}\cdot\mathbf{r}_i)^2 + \cdots \tag{1.50}$$

This is the so-called "dipole approximation" where when $\exp(\mathrm{i}\,\mathbf{k}\cdot\mathbf{r}_i) \approx 1$ then the system couples to the electric field only through the electric dipole. This approximation assumes that the wavelength of the incident field is long compared to the molecular system, so it can treated as a constant over its entire length. X-ray pulses can have wavelengths comparable to the size of molecular systems, so higher-order multipole coupling to the field should be considered. This idea and the consequences of incorrectly including higher multipole terms are investigated further in Section 3.2.

Chapter 2

TRACKING MOLECULES WITH FEMTOSECOND X-RAY ABSORPTION SPECTROSCOPY

2.1 Calibrating TDDFT for X-ray Absorption Spectroscopy

X-ray absorption spectroscopy (XAS) has become a powerful technique in chemical physics due to advances in synchrotron technology that have greatly improved its temporal and spectroscopic resolution. Our recent work on energy-specific TDDFT (ES-TDDFT) allows for the direct calculation of excitation energies in any region of the absorption spectrum, from UV-vis to X-ray. However, the ability of different density functional theories to model X-ray absorption spectra (XAS) of light elements has not yet been verified for ES-TDDFT. This work is a calibration of the ability of existing DFT kernels and basis sets to reproduce experimental K-edge excitation energies. Results were compared against 30 different transitions from gas phase experiments. We focus on six commonly used density functionals (BHandHLYP, B3LYP, PBE1PBE, BP86, HSE06, LC-ωPBE) and various triple-zeta basis sets. The effects of core and diffuse functions are also investigated. The work presented in this section is adapted with permission from P. J. Lestrange, P. D. Nguyen, X. Li, *J. Chem. Theory Comput.*, **2015**, *11*, 2994-2999.[22]

2.1.1 Introduction

X-ray absorption spectroscopy probes core excitations in molecular systems. Both transitions to bound and to continuum states are captured by this technique and many different methods have been developed to model XAS. Both the NEXAFS (XANES) and EXAFS regions of the spectrum are often modeled using a Green's function based scattering approach with muffin-tin potentials.[23,24] However, the NEXAFS region is difficult to capture without a more robust

description of the electronic structure of the absorbing atom and its neighbors. The ΔSCF approach[25] and transition-potential DFT[26,27] have been popular theoretical techniques for modeling NEXAFS spectra in the past. These techniques require the preparation of a full or partial core-hole in order to model core relaxation in a single-determinant framework. The recent orthogonality-constrained DFT method adds a proper constraint to the ΔSCF approach so that single-determinant core-excited states are guaranteed to be orthogonal to the ground-state determinant.[28,29] In contrast, response theory based time-dependent density functional theory (TDDFT) does not require preparation of core-hole states and there has been much effort recently to extend this framework to model core excitations.[1,30–33]

There are two broadly defined implementation schemes for modeling XAS with TDDFT. One approach restricts excitations to only include the core orbitals of interest and the TDDFT equations are then solved within this reduced space. This class of method is often called restricted excitation window TDDFT (REW-TDDFT).[30–33] The energy-specific TDDFT (ES-TDDFT) method,[1,33] on the other hand, does not restrict the molecular orbital space when the linear-response TDDFT equation is solved. Instead, the ES-TDDFT method utilizes a growing-window algorithm[11] to search for eigenvectors with eigenvalues that satisfy an energetic constraint. The ES-TDDFT method has been shown to obtain NEXAFS transition energies in exact agreement with solutions obtained from the full-space TDDFT framework. The growing-window method also ensures the orthogonality of different electronic states, a condition that may fail in REW-TDDFT. Although for XAS of atomic nature, such conditions can be largely satisfied even with a restricted excitation window.[34]

In this work, we focus on calibrating the performance of the ES-TDDFT method for modeling NEXAFS with an emphasis on the dependence on density functionals and basis sets. We will examine the different levels of theory to better characterize the ability of standard density functionals to model NEXAFS. We calculate the K-edge spectra of carbon, nitrogen, and oxygen and compare our results to available experimental data. This will provide a dependable benchmark for ES-TDDFT and highlight it's utility for modeling core excitations of light elements.

2.1.2 Methodology

For a detailed implementation scheme of the energy-specific TDDFT algorithm, readers are referred to Reference 1. In this section, we only provide a brief review of the ES-TDDFT approach.

Linear-response TDDFT is typically written in the non-Hermitian form in Equation (1.47). This equation can be recast for real orbitals into a non-Hermitian (Eq. (2.1)) or a Hermitian (Eq. (2.2)) problem of reduced dimension.

$$(\mathbf{A}-\mathbf{B})(\mathbf{A}+\mathbf{B})\left|\mathbf{X}+\mathbf{Y}\right\rangle = \omega^2\left|\mathbf{X}+\mathbf{Y}\right\rangle \tag{2.1}$$

$$(\mathbf{A}-\mathbf{B})^{1/2}(\mathbf{A}+\mathbf{B})(\mathbf{A}-\mathbf{B})^{1/2}\mathbf{T} = \omega^2\mathbf{T} \tag{2.2}$$

$$\mathbf{T} = (\mathbf{A}-\mathbf{B})^{-1/2}\left|\mathbf{X}+\mathbf{Y}\right\rangle \tag{2.3}$$

Energy-specific TDDFT (ES-TDDFT) solves the Hermitian problem (Equation (2.2)) to obtain excitation energies using a method similar to that of Stratmann et al.[11] The growing-window algorithm starts with a set of trial vectors that are associated with MO transitions above a target energy threshold, $\epsilon_a - \epsilon_i \geq \omega_0$. This energy threshold is defined based on the relevant region of the absorption spectrum. A subspace is then formed using these trial vectors, $\mathbf{C}$

$$\tilde{\mathbf{M}}^{+} = \mathbf{C}^T(\mathbf{A}+\mathbf{B})\mathbf{C} \tag{2.4}$$

$$\tilde{\mathbf{M}}^{-} = \mathbf{C}^T(\mathbf{A}-\mathbf{B})\mathbf{C} \tag{2.5}$$

$$\tilde{\mathbf{M}} = (\tilde{\mathbf{M}}^{-})^{1/2}(\tilde{\mathbf{M}}^{+})(\tilde{\mathbf{M}}^{-})^{1/2} \tag{2.6}$$

with the dimension of $\tilde{\mathbf{M}}$ being the number of trial vectors constructed. After the diagonalization of this subspace, only the resulting eigenvalues above the energy threshold are kept. The corresponding eigenvectors are then projected back onto the full MO space so that a residual can be computed and new vectors with significant amplitude can be added into the trial vector search space. The new and expanded set of trial vectors are used to form another subspace to be diagonalized. The procedure continues until the norm of the

residual is below a desired threshold and eigenvalues above the predefined energy threshold are obtained. Note that the reduced subspace is only used to generate new trial vectors and ensure solutions above the desired energy threshold. Because convergence is tested within the full MO space, the solutions of the ES-TDDFT methods are exact within the TDDFT framework.

2.1.3 Results and Discussion

In this work, ES-TDDFT is used to model the K-edge absorption of light elements. Several different functional and basis set combinations were tested in order to determine an appropriate model chemistry. All calculations were carried out using a development version of Gaussian.[35] A total of 30 K-edge transitions for carbon, nitrogen, and oxygen (CO, CH_2O, C_2H_4, N_2, NH_3, NO_2) were calculated using ES-TDDFT with different functional and basis set combinations. All calculated excitation energies are compared with experimental results obtained from either gaseous X-ray absorption (XAS) or inner-shell Electron Energy Loss Spectroscopy (EELS).[36–42] Assignments are made based on the symmetry and orbital character of the transition and compared with experimental assignments. Excitation energies and assignments for all transitions can be found in Supporting Information of Ref. 22. In the main discussion, we only present the error analysis of excitation energies computed with different DFT kernels and basis sets.

The commonly available functionals: BHandHLYP,[43] B3LYP,[44,45] PBE1PBE,[46,47] BP86[48,49] and two range-separated functionals: HSE06[50–52] and LC-ωPBE[53] have been included in this study. Time-dependent HF is also included as a point of contrast.[54] All electron basis sets from three commonly used families were used: the Pople 6-311+G(d,p)[55,56] basis set , the Ahlrichs def2-TZVPD[57–60] basis set, and the Dunning aug-cc-pVTZ[61,62] basis set. In order to investigate the effect of core basis functions and diffuse functions, the singly and doubly augmented cc-pCVTZ basis sets have also been included.[63,64] All ground-state structures were optimized with the B3LYP functional and the def2-TZVP basis set. Comparisons are made using the mean absolute error (Mean AE), maximum absolute error (Maximum AE),

root mean square (RMS) error, mean signed error (MSE), and the standard deviation of the error with respect to experiment. Along with the absolute errors of the excitation energies, shifted errors are also reported. Due to inherent problems with DFT and the neglect of relativistic effects, DeBeer *et al.*[65] have proposed that relative transition energies are more chemically relevant quantities than absolute transition energies when modeling core excitations. We apply a uniform shift to the calculated spectrum such that the lowest-energy peak perfectly matches the experimental value, as is done in other studies.[32,66,67] The errors are then calculated using the remaining transitions.

Table 2.1 shows the error analysis of predicted K-edge spectra with the ES-TDDFT method. When absolute (unshifted) errors are considered, functionals with a larger percentage of Hartree-Fock exchange result in transition energies much closer to experimental values. This is consistent with trends seen in previous studies.[32,33] BHandHLYP has 50% HF exchange (the largest percentage of HF exchange among all DFT kernels considered here) and consistently outperforms the other functionals in terms of absolute errors with respect to experimental results. The pure density functional (BP86), with no HF exchange, significantly underestimates the K-edge excitation energies by as much as ∼26 eV, compared to only 2-4 eV error by BHandHLYP and 11-17 eV error by B3LYP, PBE1PBE, and HSE06. The good performance of BHandHLYP is likely attributed to the lower self-interaction error as compared to the other functionals,[68] and error cancellations arising from the fact that TDHF consistently overestimates the excitation energies by 15-22 eV.

The two range-separated functionals tested, HSE06 and LC-ωPBE, are based on the PBE functional and include short-range and long-range HF exchange respectively. The HSE06 functional has comparable absolute errors to PBE1PBE (11-15 eV), but LC-ωPBE underestimates K-edge excitation energies by 18-24 eV. The inclusion of exact short-range exchange has been shown to reduce the self-interaction error and improve the description of core excitation energies while long-range exchange appears to be less important for core excitations.[68,69] Without the inclusion of short-range exchange the transition energies calculated with LC-ωPBE are more similar to those calculated with the pure functional.

		Absolute Errors					Shifted Errors				
		Mean AE	RMS	Max AE	MSE	Std. Dev.	Mean AE	RMS	Max AE	MSE	Std. Dev.
BP86	6-311+G(d,p)	20.09	20.24	24.51	-20.09	2.46	1.68	1.82	2.71	-1.39	1.18
	def2-TZVPD	19.93	20.09	24.54	-19.93	2.55	1.75	1.86	2.59	-1.22	1.41
	aug-cc-pVTZ	20.45	20.59	24.79	-20.45	2.40	1.98	2.18	3.12	-1.97	0.94
PBE1PBE	6-311+G(d,p)	11.36	11.43	13.79	-11.36	1.23	0.58	0.73	2.20	-0.24	0.68
	def2-TZVPD	11.21	11.30	13.80	-11.21	1.41	0.72	1.05	3.62	-0.06	1.05
	aug-cc-pVTZ	11.60	11.65	13.80	-11.60	1.12	0.70	0.78	1.26	-0.67	0.40
B3LYP	6-311+G(d,p)	12.88	12.97	15.85	-12.88	1.54	0.93	1.04	2.20	-0.63	0.83
	def2-TZVPD	12.72	12.83	15.84	-12.72	1.67	1.05	1.20	3.07	-0.45	1.12
	aug-cc-pVTZ	13.13	13.21	15.86	-13.13	1.46	1.09	1.19	1.80	-1.06	0.55
BHandHLYP	6-311+G(d,p)	1.92	2.06	3.87	-1.87	0.88	1.03	1.17	2.57	0.97	0.65
	def2-TZVPD	1.90	2.04	3.89	-1.74	1.08	1.22	1.55	4.92	1.15	1.05
	aug-cc-pVTZ	2.06	2.16	3.85	-2.06	0.65	0.73	0.82	1.62	0.65	0.51
HF	6-311+G(d,p)	15.27	15.73	21.45	15.27	3.78	4.02	4.30	6.11	3.90	1.82
	def2-TZVPD	15.29	15.75	21.28	15.29	3.78	4.10	4.50	8.66	3.97	2.11
	aug-cc-pVTZ	15.08	15.52	21.25	15.08	3.67	3.78	4.09	5.93	3.65	1.84
HSE06	6-311+G(d,p)	11.33	11.40	13.72	-11.33	1.23	0.54	0.70	2.21	-0.20	0.67
	def2-TZVPD	11.18	11.27	13.73	-11.18	1.39	0.68	1.03	3.63	-0.02	1.03
	aug-cc-pVTZ	11.56	11.61	13.72	-11.56	1.11	0.64	0.71	1.16	-0.60	0.38
LC-ωPBE	6-311+G(d,p)	18.77	18.93	23.25	-18.77	2.47	0.57	0.72	2.19	-0.16	0.71
	def2-TZVPD	18.57	18.76	23.17	-18.57	2.60	0.73	1.03	3.43	0.03	1.03
	aug-cc-pVTZ	18.90	19.05	23.17	-18.90	2.40	0.60	0.71	1.48	-0.53	0.48

Table 2.1. Errors for all K-edge transitions (eV) using different basis set families. Mean absolute error (Mean AE), root mean square (RMS) error, maximum absolute error (Max AE), mean signed error (MSE), and the standard deviation of the error are compared to experimental results.[36–42] For the shifted errors, the whole spectrum is shifted so that the lowest-energy transition matches perfectly with experiment and the errors of all other peaks are then evaluated.

Based on the shifted errors, all hybrid functionals are much improved. The pure functional is less reliable with errors as large as ∼4 eV. Unlike absolute transition energies, the magnitude of exact exchange among hybrid functionals does not appear to be the most important factor for reproducing relative transition energies. For example, the PBE1PBE functional has the lowest shifted errors (among the functionals that are not range-separated) for several of the basis sets tested. The shifted results for TDHF are still very poor, indicating the importance of electron correlation on core excitations.

From the statistics of all K-edge excitations summarized in Tab. 2.1 and Tab. 2.2, BHandHLYP clearly shows the best agreement with experimental values when absolute excitation energies are considered. When shifted results are used as in most computational practices, all hybrid functionals considered here show similarly good performance with HSE06 being the best choice in terms of mean average errors and standard derivation.

Table 2.1 also shows that absolute errors of K-edge excitations are less sensitive to the quality of valence basis compared to the shifted results. Among the three split- valance basis sets considered in Tab. 2.1, aug-cc-pVTZ results have a smaller standard deviation compared to the other two sets. As the XAS probes core electron excitations, the quality of core basis can be very important on the accuracy of computed spectrum. Flexible basis sets with a reasonable number of core functions, such as the cc-pCVTZ basis set, could improve the description of core orbital relaxation upon excitation. Diffuse functions have also been shown to have a large effect on transition energies,[70,71] so we have included the singly and doubly augmented triple-zeta Dunning basis sets with and without core functions.

Table 2.2 compares K-edge excitations using different basis sets with a focus on the importance of core and diffuse basis functions. The addition of more core functions seems to have little effect for these light elements as the excitation energies shift only slightly toward the experimental values. Although, the average change due to these additional core functions does increase with atomic number. This suggests that core functions will be more important for heavier elements where the other functions in the set may not be capable of describing the core relaxation well. The shifted results are virtually unchanged with the addition of

		Absolute Errors					Shifted Errors				
		Mean AE	RMS	Max AE	MSE	Std. Dev.	Mean AE	RMS	Max AE	MSE	Std. Dev.
BP86	aug-cc-pVTZ	20.45	20.59	24.79	-20.45	2.40	1.98	2.18	3.12	-1.97	0.94
	aug-cc-pCVTZ	20.50	20.64	24.88	-20.50	2.42	1.97	2.18	3.12	-1.97	0.93
	d-aug-cc-pVTZ	20.96	21.12	25.75	-20.96	2.60	2.68	2.83	4.09	-2.68	0.93
	d-aug-cc-pCVTZ	21.01	21.18	25.87	-21.01	2.63	2.69	2.85	4.08	-2.69	0.94
PBE1PBE	aug-cc-pVTZ	11.60	11.65	13.80	-11.60	1.12	0.70	0.78	1.26	-0.67	0.40
	aug-cc-pCVTZ	11.64	11.70	13.88	-11.64	1.14	0.70	0.78	1.26	-0.67	0.40
	d-aug-cc-pVTZ	11.86	11.93	14.43	-11.86	1.25	1.04	1.14	1.77	-1.04	0.48
	d-aug-cc-pCVTZ	11.91	11.98	14.52	-11.91	1.27	1.05	1.15	1.78	-1.05	0.48
B3LYP	aug-cc-pVTZ	13.13	13.21	15.86	-13.13	1.46	1.09	1.19	1.80	-1.06	0.55
	aug-cc-pCVTZ	13.16	13.25	15.93	-13.16	1.48	1.09	1.19	1.79	-1.06	0.55
	d-aug-cc-pVTZ	13.42	13.52	16.49	-13.42	1.60	1.48	1.57	2.32	-1.48	0.54
	d-aug-cc-pCVTZ	13.46	13.56	16.57	-13.46	1.62	1.49	1.58	2.32	-1.49	0.55
BHandHLYP	aug-cc-pVTZ	2.06	2.16	3.85	-2.06	0.65	0.73	0.82	1.62	0.65	0.51
	aug-cc-pCVTZ	2.09	2.19	3.87	-2.09	0.65	0.73	0.82	1.61	0.65	0.51
	d-aug-cc-pVTZ	2.22	2.31	3.85	-2.22	0.62	0.57	0.68	1.50	0.42	0.53
	d-aug-cc-pCVTZ	2.25	2.34	3.87	-2.25	0.62	0.57	0.68	1.51	0.42	0.54
HF	aug-cc-pVTZ	15.08	15.52	21.25	15.08	3.67	3.78	4.09	5.93	3.65	1.84
	aug-cc-pCVTZ	15.05	15.49	21.22	15.05	3.66	3.78	4.09	5.95	3.65	1.84
	d-aug-cc-pVTZ	15.01	15.44	21.15	15.01	3.62	3.67	4.00	5.85	3.55	1.84
	d-aug-cc-pCVTZ	14.98	15.41	21.12	14.98	3.61	3.68	4.01	5.87	3.55	1.85
HSE06	aug-cc-pVTZ	11.56	11.61	13.72	-11.56	1.11	0.64	0.71	1.16	-0.60	0.38
	aug-cc-pCVTZ	11.59	11.65	13.79	-11.59	1.13	0.64	0.71	1.15	-0.60	0.38
	d-aug-cc-pVTZ	11.84	11.90	14.32	-11.84	1.24	1.00	1.09	1.64	-1.00	0.42
	d-aug-cc-pCVTZ	11.88	11.95	14.41	-11.88	1.26	1.01	1.10	1.66	-1.01	0.43
LC-ωPBE	aug-cc-pVTZ	18.90	19.05	23.17	-18.90	2.40	0.60	0.71	1.48	-0.53	0.48
	aug-cc-pCVTZ	18.94	19.10	23.25	-18.94	2.43	0.60	0.71	1.48	-0.53	0.48
	d-aug-cc-pVTZ	19.08	19.24	23.36	-19.08	2.46	0.78	0.93	1.66	-0.78	0.51
	d-aug-cc-pCVTZ	19.11	19.28	23.43	-19.11	2.49	0.78	0.93	1.65	-0.78	0.51

Table 2.2. Errors for all K-edge transitions (eV) focusing on the effect of core and diffuse functions. Mean absolute error (Mean AE), root mean square (RMS) error, maximum absolute error (Max AE), mean signed error (MSE), and the standard deviation of the error are compared to experimental results.[36–42] For the shifted errors, the whole spectrum is shifted so that lowest-energy transition matches perfectly with experiment and the errors of all other peaks are then evaluated.

more core functions, differing by < 0.01 eV. Diffuse functions have a slightly larger effect on the transition energies. An extra set of diffuse functions slightly increases the absolute error for all functionals, but is slightly reduced for TDHF. For the shifted spectra, the error is reduced for BHandHLYP and TDHF, but increases for all other methods with $< 50\%$ HF exchange. Without a large portion of HF exchange, additional diffuse functions are not advantageous and lead to a worse description of the relative transition energies.

2.1.4 Conclusion

Six density functional kernels and various basis sets were used to evaluate the accuracy of ES-TDDFT for describing K-edge transitions of carbon, nitrogen, and oxygen. The results of 30 different transitions were compared against experimental values in the gas phase. There is a consistent improvement in the absolute values of the calculated excitation energies with increasing Hartree-Fock exchange.[32,33] Particularly, short-range exchange was shown to be an important component of any hybrid functional applied to core excitations. When shifted results are used, all hybrid functionals considered here show similarly good performance with HSE06 being the best choice in terms of mean average errors and standard derivation.

For K-edge excitations of light elements, the choice of basis set does not appear to have a large effect on the absolute or shifted errors of the transition energies and these errors are mostly dominated by the choice of the functional. Although a second set of diffuse functions seems to increase the error of the shifted spectra for all functionals with $< 50\%$ HF exchange.

2.2 Dynamics of a Nickel Porphyrin: Insights from Experiment and Theory

Photoexcited Nickel(II) tetramesitylporphyrin (NiTMP), like many open-shell metalloporphyrins, relaxes rapidly through multiple electronic states following an initial porphyrin-based excitation, some involving metal centered electronic configuration changes that could be harnessed catalytically before excited state relaxation. While a NiTMP excited state present at 100 ps was previously identified by X-ray transient absorption (XTA) spectroscopy at a synchrotron source as a relaxed (d,d) state, the lowest energy excited state (*J. Am.*

Chem. Soc., **2007**, *129*, 9616 and *Chem. Sci.*, **2010**, *1*, 642),[72,73] structural dynamics before thermalization were not resolved due to the ∼100 ps duration of the available X-ray probe pulse. Using the femtosecond (fs) X-ray pulses of the Linac Coherent Light Source (LCLS), the Ni center electronic configuration from the initial excited state to the relaxed (d,d) state has been obtained via ultrafast Ni K-edge XANES (X-ray absorption near edge structure) on a time scale from hundreds of femtoseconds to 100 ps. This enabled the identification of a short-lived Ni(I) species aided by time-dependent density functional theory (TDDFT) methods. Computed electronic and nuclear structure for critical excited electronic states in the relaxation pathway characterize the dependence of the complex's geometry on the electron occupation of the 3d orbitals. Calculated XANES transitions for these excited states assign a short-lived transient signal to the spectroscopic signature of the Ni(I) species, resulting from intramolecular charge transfer on a time scale that has eluded previous synchrotron studies. These combined results enable us to examine the excited state structural dynamics of NiTMP prior to thermal relaxation and to capture intermediates of potential photocatalytic significance. The work presented in this section is adapted with permission from M. L. Shelby, P. J. Lestrange, N. E. Jackson, K. Haldrup, M. W. Mara, A. B. Stickrath, D. Zhu, H. Lemke, B. M. Hoffman, X. Li, L. X. Chen, *J. Am. Chem. Soc.*, **2016**, *138*, 8752-8764.[2]

2.2.1 Introduction

Molecular photoexcitation generates high-energy transient species capable of driving subsequent chemical reactions. The challenge for energy conversion from light entails directing these transient species to minimize unwanted processes, such as heat generation and geminate charge recombination. Transition metal complexes (TMCs) have previously been selected for photochemical applications primarily based on the condition of possessing nanosecond or longer triplet excited state lifetimes (and large redox potentials).[74–76] While such selection criteria are sufficient to ensure that a reactive species will persist, recent studies have shown that some excited TMCs can initiate photochemical processes on the picosecond or

subpicosecond time scales via singlet excited states, time scales that are competitive with vibrational relaxation, and faster than intersystem-crossing to a triplet excited state.[72,77–82] Such short-lived excited states are less susceptible to energy dissipation processes that would reduce the potential driving force of a reaction. However, experimentally characterizing the TMC electronic and nuclear configurations of excited states on these time scales is challenging, making rational control difficult. Recent ultrafast optical spectroscopic measurements have provided substantial information on the reaction dynamics of TMCs,[83–91] but optical signatures of metal-centered electronic transitions for these critical TMC intermediates are frequently nonexistent or obscured by $\pi \rightarrow \pi^*$ optical signatures localized on aromatic ligands. A greater understanding of the electronic and nuclear structural response to excitation on fs to ps time scales is needed to utilize these potentially catalytic intermediates and could be pivotal to identifying a new regime of efficient metal based photocatalysts, light sensitizers, and electron donor/acceptors that might otherwise be neglected on the basis of selection criteria focused on triplet state lifetimes.

Pump-probe X-ray spectroscopies are element specific, and can selectively probe both the dynamic electronic structure of a TMC's metal center and its local nuclear dynamics following photoexcitation without interference from ligand-localized transitions.[92–100] Recently, X-ray free electron laser (XFEL) sources capable of producing femtosecond X-ray pulses[101,102] have become available for these studies.[92] By implementing this experimental approach along with accurate theoretical modeling, rational control over transient, catalytically active TMC species becomes a possibility.

Metalloporphyrins possess versatile functionality as light harvesting/electron transfer cofactors, both in biological processes (natural photosynthesis,[103,104] physiological oxygen transport,[105] and small molecule sensing)[106] and photocatalytic processes where they act as redox centers,[107–109] and sensitizers in molecular devices.[110] Such functional versatility is enabled by a high degree of chemical tunability in both the choice of metal center and the ligated macrocycle. Changes in macrocycle functionalization can dramatically impact metalloporphyrin ring conformation and rigidity, leading to varied redox and ligand binding

properties, as well as the ability to impact relaxation dynamics by altering the energetic ordering of excited states. Open-shell transition metal porphyrins have not historically been seen as candidates for solar energy conversion due to their relatively fast excited state deactivation through d-orbital vacancies. While originally thought to be a disadvantage when judged with the triplet lifetime criteria, the ability to rationally control this ultrafast deactivation mechanism presents an exciting possibility for funneling the photon energy absorbed via porphyrin-based $\pi \rightarrow \pi^*$ transitions to redox equivalents at the metal centers via intramolecular charge transfer.

Nickel porphyrins and phthalocyanines have been of particular interest as model complexes to provide guidance for targeted molecular design in part due to their conformational flexibility brought on by the small Ni core size and the ease with which certain ring conformers can be stabilized to tune relaxation kinetics. Nickel(II) tetramesitylporphyrin (NiTMP), which exists in the ground state as an ensemble of ring conformers, and its analogues, have complicated photo- chemical dynamics and have been extensively studied by optical absorption[73,111] and Raman spectroscopy.[112–117] These studies, combined with quantum-mechanical calculations, proposed a plausible pathway for the photoexcitation. Within 20 ps of the photoexcitation that initiates the $S_0 \rightarrow S_1$ transition, a porphyrin macrocycle based $\pi \rightarrow \pi^*$ transition, the electron promoted to the π^* orbital moves to an empty $3d_{x^2-y^2}$ orbital, the highest energy ligand field state for a square-planar complex, and an electron from an originally filled $3d_{z^2}$ orbital moves to fill the hole in the π orbital of the macrocycle left by the initial photoexcitation, resulting ultimately in the lowest- lying triplet state, ($3d_{z^2}$, $3d_{x^2-y^2}$). This state has a 3d electronic configuration of $(3d_{x^2-y^2})^1(3d_{z^2})^1$ and is here denoted T(d,d) (Figure 2.1).[112,118] A pump-pump-probe transient absorption measurement of Ni(II) porphyrin excited state dynamics suggested that a transient Ni(I) charge transfer state may exist with a lifetime of a few picoseconds,[111] but previously such a reaction pathway could not be substantiated by monitoring the temporal evolution of the nickel electronic configuration. In comparison to these previous optical and vibrational spectroscopic studies, X-ray transient absorption (XTA) spectroscopy,[92,93] which combines a laser excitation and con-

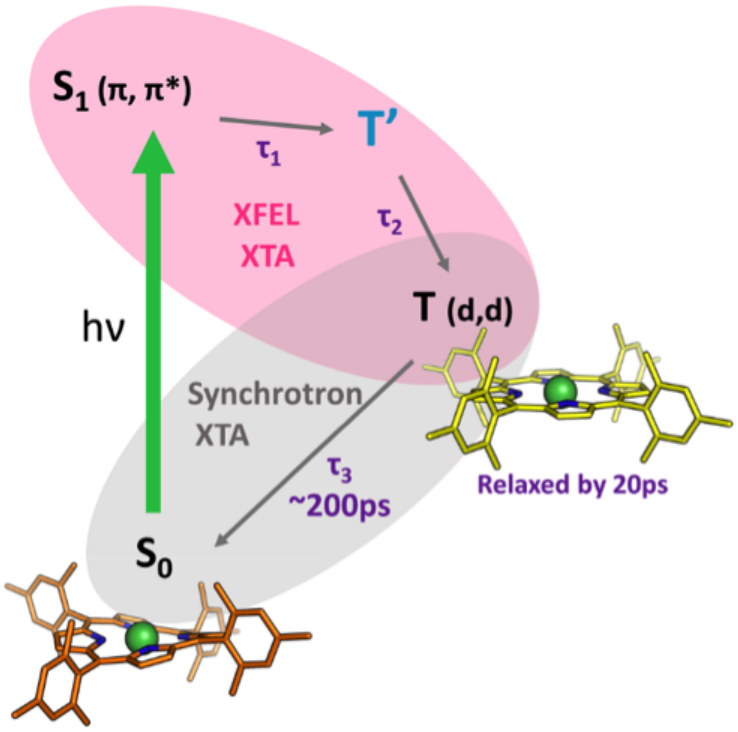

Figure 2.1. The relaxation pathway of NiTMP following Q-band excitation (e.g. at 527 nm). Structures for states characterized by XTA are shown. Within a few ps the porphyrin macrocycle $S_1(\pi, \pi^*)$ population has dissipated by transfer of the excitation to the metal center. The resulting state (T') is therefore either a hot ($3d_{z^2}$, $3d_{x^2-y^2}$) state which decays to the relaxed ($3d_{z^2}$, $3d_{x^2-y^2}$) state T(d,d) via vibrational relaxation or a (π, $3d_{x^2-y^2}$) state with Ni(I) character that transfers an electron back to the ligand. By 20 ps the T(d,d) state is fully populated and vibrationally relaxed, and has adopted a flattened structure with elongated Ni-N bonds. This T(d,d) state decays back to the ground state with a 200 ps lifetime.

ventional X-ray absorption spectroscopy,[119] can directly probe the metal center electronic structure and local geometry rather than relying on the indirect deduction of excited state dynamics from relatively broad transient optical spectral features.

Previous XTA studies at a synchrotron source (the Advanced Photon Source, Argonne

National Laboratory) with ∼100 ps time resolution[72,73] have conclusively verified that the thermalized excited T(d,d) state has an $(3d_{x^2-y^2})^1(3d_{z^2})^1$ electronic configuration, and have captured this state's elongated Ni-N bond length and flattened macrocycle conformation through analysis of the Extended X-ray Absorption Fine Structure (EXAFS), which arises from scattering processes with atoms neighboring the absorbing Ni.[72,73,120] However, the time resolution of the synchrotron X-ray pulses was insufficient to detect detailed excited state structural dynamics before the development of the relaxed T(d,d) state. In this study, this missing time window in the evolution of excited Ni(II)TMP is obtained by collection of XTA spectra near the nickel K-edge (8333 eV) with the subpicosecond time resolution provided by the Linac Coherent Light Source (LCLS), an X-ray free electron capable of delivering femtosecond X-ray pulses of incredible intensity.[98,121] This study has in fact disclosed a transient charge transfer state, denoted T' for consistency with previous work, that occurs prior to the appearance of T(d,d) (Figure 2.1) and, importantly, the X-ray absorption near edge spectra (XANES) of electronic states and geometries in the proposed photochemical trajectory were calculated and the effects of different orbital occupancies, Ni-N bond lengths, and the magnitude of repulsive potential acting on the Ni 1s electrons were correlated with trends in the experimental spectra.

2.2.2 Electronic Structure Calculations

To understand the overall electronic and structural evolution of the NiTMP excited states and to ascertain how changes in the electronic and nuclear structure as the molecule relaxes are reflected in the experimentally observed XTA signals, each electronic state in the proposed mechanism (Figure 2.1) was modeled separately. Initial DFT and TDDFT calculations using the BP86 functional were employed to probe the basic orbital structure of NiTMP and its excited states using the ADF package.[122,123] A double-ζ polarized (DZP) basis set was used for the description of C, N, and H atoms, and a triple-polarized (TZP) basis set was used to describe the atomic orbitals of Ni. This combination of functional and basis set has previously described the orbital structure of a related Ni compound with

high accuracy.[124] Subsequently, the geometries of the ground and each intermediate excited state were optimized with the BP86 functional[48,49] and the 6-31G(d) basis set[125,126] using a development version of the Gaussian software package.[35] The X-ray absorption was calculated with energy-specific TDDFT (ES-TDDFT)[1,22] using the PBE1PBE and Ahlrichs' def2-TZVP basis set[57] with diffuse functions on the nickel atom.[58–60] For all calculations of X-ray absorption spectra, the mesityl groups on the porphyrin have been replaced with methyl groups to reduce computational cost.

2.2.3 Results

2.2.3.1 Ni K-edge XANES Describe Excited State Electronic and Structural Dynamics

In the Ni K-edge XANES spectra shown in Figure 2.2, the spectrum at a -5 ps pump-probe time delay (before the laser arrives) is identical to the previously obtained spectrum for the ground state S_0,[72,127] while the spectra at the 20 ps time delay and longer resemble the spectrum identified by the same study as the T(d,d) state.[72,73]

Comparing the spectra at 100 ps delay with the T(d,d) spectrum and considering the 200 ps T(d,d) state decay time constant obtained previously, we estimate the initial excited state fraction to be ∼60% (see Supporting Information 2 of Ref. 2). XANES features for the S_0 and T(d,d) states have been assigned and share attributes characteristic of a square planar Ni(II) coordination geometry. A distinct peak at 8339 eV in the S_0 state spectrum and at 8341 eV in the T(d,d) state spectrum (Figure 2.2A, labeled E2 and E3), respectively, are assigned to the strong dipole-allowed 1s → $4p_z$ transition.[20] Features near the "white line" absorption peak at 8351 eV are ascribed to contributions from multiple scattering resonances and transitions from Ni 1s to π^* antibonding molecular orbitals resulting from the hybridization of Ni $4p_x$ and $4p_y$ orbitals with porphyrin N 2s orbitals. Below the rising edge in the pre-edge region from 8330 to 8336 eV are weak quadrupole-allowed 1s → vacant 3d transitions, which directly probe the 3d orbital energies and electronic occupation,[128] determined by the coordination geometry and electronic state of the Ni center. The 4p

orbitals are vacant for Ni complexes, so changes in transition energies to these orbitals, as well as to all high energy bound states, are determined by perturbations to the 4p energies and changes in the energy of the core orbitals due to structural or oxidation state changes.

The progression of the electronic state population $S_0 \rightarrow S_1 \rightarrow T(d,d)$ is captured by XANES spectra taken as a function of the pump-probe delay time. The peak position of the $1s \rightarrow 4p_z$ transition for the S_0 state at 8339 eV (Figure 2.2A, label E2) clearly shifts to 8341 eV, the energy for the same transition in the T(d,d) state. Meanwhile in the less well-resolved white line region, the prominent peak feature shifts from 8359 to 8353 eV.

While the $\sigma^*_{x,y}$ orbitals should shift to lower energy in the excited state as the Ni-N distances expand and the hybridization between the Ni $4p_{x,y}$ and Ni 2s orbitals is weakened,[129] the $4p_z$ transition blue shift has not yet been well explained due to the fact that coupling between the Ni $4p_z$ orbital and porphyrin π-orbitals is minimal.

At a glance, the spectra at time delays of –5 to 20 ps seem to resemble mixtures of the S_0 and T(d,d) states, but a feature around 8337 eV in the difference spectra (Figure 2.2C) is a notable exceptions. A transient feature at 8337 eV rises rapidly to its maximum amplitude at 400 to 800 fs, and decays within ∼2 ps (Figure 2.2B and Figure 2.2C). After ∼2 ps, the XANES difference reflects an increasing population of T(d,d) state, whose features are fully developed by 10 ps.

The ground state $1s \rightarrow 4p_z$ peak depletion proceeds with an approximate time constant of ∼1 ps, in contrast to the growth kinetics of the T(d,d) state $1s \rightarrow 4p_z$z peak, which displays a sharp rise after ∼200 fs followed by a slower rise to the maximum peak height, suggesting the presence of an additional transient state, which we denote T' (Figure 2.1) preceding the relaxed T(d,d) state (Figure 2.2C). Other dynamics of spectral features on the ps time scale include an apparent delay between the rise of the white line peak feature at 8353 eV, which is an indication of the Ni-N bond elongation as seen in the T(d,d) state, and the rise of the $1s \rightarrow 4p_z$ transition peak associated with T(d,d).

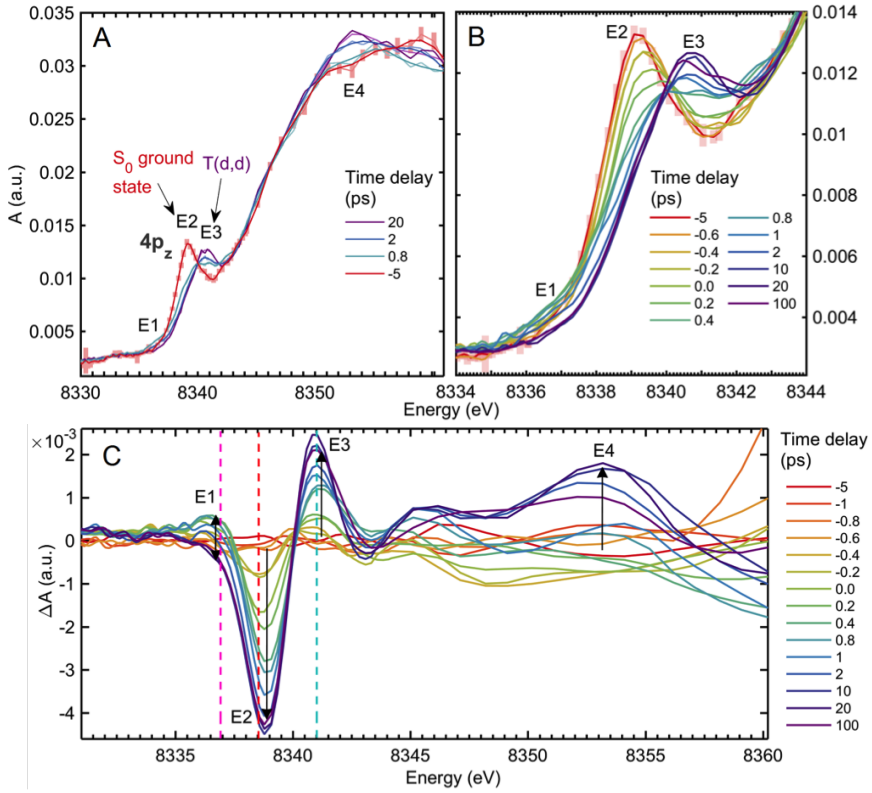

Figure 2.2. Smoothed Ni K-edge XANES spectra of NiTMP between -5 and 100 ps following 527 nm excitation. Numbered energies correspond to E0, the 1s → 3d transition ("pre-edge") region; E1, a transient at the low-energy end of the 1s → $4p_z$ region; E2, the S_0 1s → $4p_z$ transition; E3, the T(d,d) 1s → $4p_z$ transition; and E4, the white-line feature associated with shortened Ni-N bonds in the T(d,d) state. (A) Time delays characteristic of (-5 ps) S_0, (0.4 ps) the peak of the transient signal at 8337 eV, (2 ps) the partial disappearance of the transient at 8337 eV, the appearance of the T(d,d) 1s → $4p_z$ peak at E2, and the shift of the primary white line feature to E4, and (20 ps) T(d,d). (B) The evolution of the XANES from -5 to 100 ps within the 1s → $4p_z$ region. (C) Difference spectra relative to S_0 spectrum for delays between -5 and 100 ps.

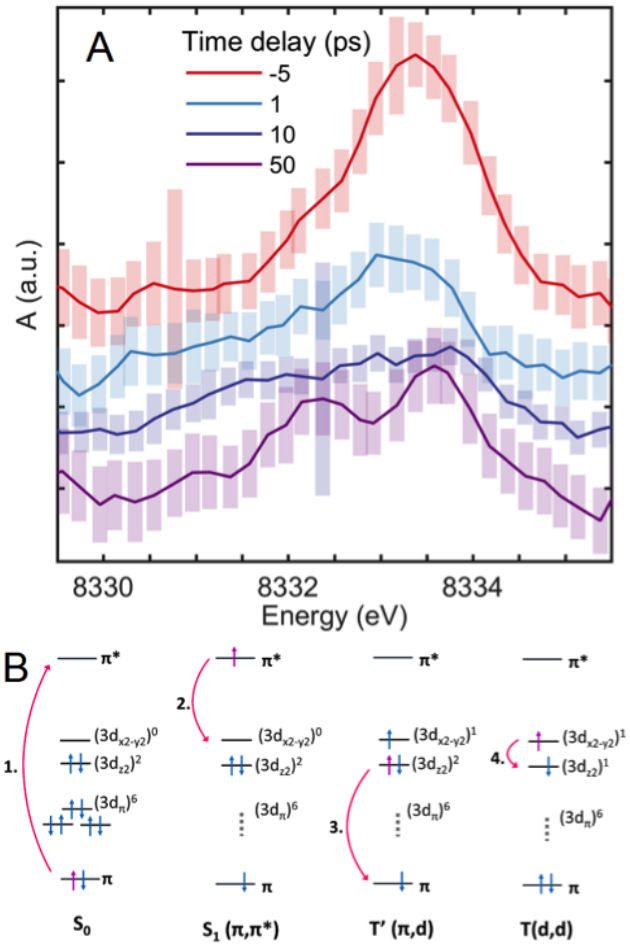

Figure 2.3. (A) XANES scans in the 1s → 3d region, 5 pt smoothed and with the rising XANES edge background subtracted. (B) 3d-orbital occupations of electronic states in the NiTMP relaxation pathway resulting from: (1) excitation of the porphyrin macrocycle, (2) charge transfer from the macrocycle π^* orbital to the Ni metal center, (3) reverse charge transfer from Ni to the macrocycle via relaxation of a $3d_{z^2}$ electron into the π hole, (4) relaxation of the $3d_{x^2-y^2}$ electron into the $3d_{z^2}$ to recover the ground state d-orbital configuration.

2.2.3.2 Ni 3d Orbital Configuration from Pre-edge Transitions

Pre-edge features corresponding to quadrupole- allowed transitions from 1s to vacant 3d orbitals in the nickel center provide insight into the electronic configuration of the 3d or-

bitals. In synchrotron experiments, the pre-edge region of S_0 contains a single peak for the 1s $\rightarrow$ $3d_{x^2-y^2}$ transition arising from the electronic configuration of $(3d_{z^2})^2(3d_{x^2-y^2})^0$ (Figure 2.3B, S_0).[72] By 50 ps after photoexcitation (Figure 2.3B, 1.), the T(d,d) excited state is fully populated and its pre-edge exhibits two peaks arising from the 1s $\rightarrow$ $3d_{x^2-y^2}$ and 1s $\rightarrow$ $3d_{z^2}$ transitions available for the $(3d_{z^2})^1(3d_{x^2-y^2})^1$ electronic configuration (Figure 2.3B, T(d,d)) which eventually decays to the ground state (Figure 2.3B, 4.). Looking at the time evolution of the d-orbital transition region (Figure 2.3A), at the negative delay representing 100% ground state population, we see a single peak corresponding to the transition to the sole 3d vacancy, $3d_{x^2-y^2}$, consistent with previous synchrotron experiments.[72,73] Following excitation, the d-orbital transitions are derived from a mixture of states which we interpret as evolving according to a series of processes represented in Figure 2.3B. At 1 ps delay time, the magnitude of this peak is diminished and slightly red- shifted, while by 10 ps the pre-edge features are significantly broadened with some intensity growing in at lower energy. At 50 ps delay time, we see features associated with the T(d,d) state, where single vacancies in the $3d_{x^2-y^2}$ and $3d_{z^2}$ lead to a split peak, although the splitting energy is 1 eV less than the 2.3 eV observed at 100 ps during synchrotron experiments. This splitting is not clearly discernible by 1 ps, but may influence the shape of the broadened features at 10 ps. The absence of a split peak by 1 ps is contradictory to the full conversion of the excited population to T(d,d) by 350 fs, as suggested by previous studies.[130] Total population of the vibrationally hot T(d,d) state is more consistent with the 10 ps spectrum where the 1s $\rightarrow$ $3d_{x^2-y^2}$ and 1s $\rightarrow$ $3d_{z^2}$ transitions appear to be broadened with the 1s $\rightarrow$ $3d_{x^2-y^2}$ slightly higher in energy, possibly due to the shorter Ni-N bond length.

Directly detecting T' features for these weakly absorbing transitions is complicated by the fact that T' appears to be short-lived, present at low accumulation, and exists simultaneously with several other electronic states. Features at 1 ps are likely ascribable to a combination of the S_1 state, T', and broadened T(d,d) features.

	input for excited state XAS modeling							
wave function	S_0	$S_1(\pi,\pi^*)$	T'	T(d,d)	S_0	S_0	T(d,d)	T(d,d)
geometry	S_0	$S_1(\pi,\pi^*)$	T'	T(d,d)	T'	T(d,d)	S_0	$S_1(\pi,\pi^*)$
	eV	Δ eV						
1s α	-8167.47	-0.05	2.02	-1.17	-0.37	-0.34	-0.67	-0.61
1s β	-8167.47	-0.05	2.03	-1.17	-0.37	-0.34	-0.67	-0.61
$4p_z$ α	-1.39	-0.07	0.18	-0.23	0.06	-0.03	-0.15	-0.16
$4p_z$ β	-1.39	-0.06	0.05	-0.44	0.06	-0.03	-0.34	-0.34

Table 2.3. Orbital Energies for the Ground State and for Excited State Electronic Configurations and Geometries

2.2.3.3 Modeling of Inner Shell XAS Bound Transitions

Solutions to the Self Consistent Field (SCF) equations that converge to a higher energy than ground state solutions have long been recognized as useful approximations to excited state wave functions.[131–133] These solutions allow excited states to be treated in a single determinant framework whose response can be modeled with TDDFT. In order to obtain these higher-energy SCF solutions, a set of natural transition orbitals (NTOs)[134] for the state of interest was first generated at the excited state geometry. The initial guess for the SCF density of this higher-energy solution was then formed by a HOMO–LUMO swap of the dominant NTOs. A second-order optimization scheme was then used to converge to the state of interest.[135] The XANES spectra of these intermediate states were then calculated with ES-TDDFT at the same level of theory as the ground state (discussed in Section 2.2.2).

Due to the neglect of scalar and spin-orbit relativistic effects in this simulation, the calculated transitions are much lower in energy than the experimental results. However, it has been shown that these operators have little effect on relative transition energies[67] and uniform shifts are routinely applied to calculated XANES spectra to better compare

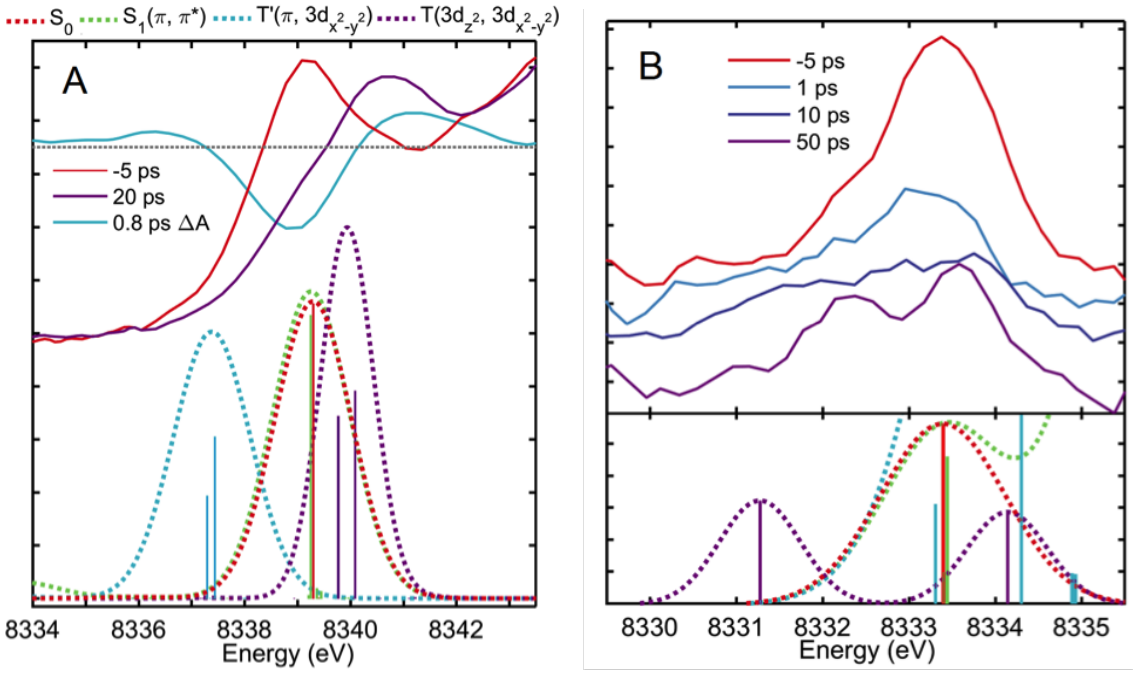

Figure 2.4. Gaussian-broadened calculated XAS transitions of relevant excited electronic states compared to experimental spectra in (A) the rising edge regions where 1s $\rightarrow$ 4p$_z$ transitions dominate and (B) the pre-edge region.

transition energies with experimental data.[32,66,67] A uniform shift of 172 eV is applied to all calculated spectra and all transitions are convoluted with Gaussian functions to match experimental lineshapes; 2.2 and 1.8 eV FWHM for the 4p$_z$ and 3d transitions, respectively.

The dipole allowed 1s $\rightarrow$ 4p transitions are the dominant transitions in all calculated XAS (Table 2.3, Figure 2.4A). The electronic environment around the Ni atom has changed minimally between the S_0 and $S_1(\pi, \pi^*)$ states, so little change is seen in the 1s $\rightarrow$ 4p$_z$ transition. However, a red and a blue shift is observed for the T' and T(d,d) states, respectively. These trends reproduce those of the experimental data where the T(d,d) 1s $\rightarrow$ 4p transition is clearly blue-shifted compared to the S_0 and a short-lived rise and fall is evident red of the S_0 peak. It is worth noting, however, that the calculated transitions are pure populations of their respective electronic states, which do not exist in the relaxation of the excited NiTMP

and the experimental data reflects of a mixture of states.

For this system, the modeled 1s $\rightarrow$ 3d transitions reflect the expected 3d-orbital occupation for the ground and T(d,d) states. Modeled transitions to $3d_{z^2}$ and $3d_{x^2-y^2}$ roughly coincide with the two peaks apparent in the experimental XANES at 50 ps delay (Figure 2.4B) and are very similar to those observed in the pre-edge region at 100 ps during our previous synchrotron experiments.[72,73] The experimental 1s $\rightarrow$ $3d_{x^2-y^2}$ peak at 1 ps is slightly red-shifted compared to the ground state, and this same behavior is seen for the modeled transition for the T' state. This red shift is notable as it contrasts with the blue shift observed for the same transition at 50 ps and for the modeled T(d,d) state. A weakly dipole allowed 1s $\rightarrow$ π transition is apparent in the calculated spectra of the $S_1(\pi, \pi^*)$ and T' states, although these are not plotted because their contribution is removed during background subtraction of the experimental data. Furthermore, these are relatively short-lived states, the contribution to the total signal is quite small, and this region of the spectrum is very noisy due to low XAS signal, so well-defined peaks for these weak dipole allowed transitions are not observed experimentally.

2.2.4 Discussion

This study, which is among early examples of XTA measurements at LCLS, allows us to establish a kinetic scheme describing the decay of photoexcited NiTMP and to distinguish the short-lived Ni(I) state T' as an intermediate preceding the formation of the previously characterized T(d,d) state. Inner-shell transitions characterized by the combined experimental and computational results are analyzed to derive properties not directly measurable using other ultrafast methods. Here, we discuss the evidence for the charge transfer nature of the short-lived T' state, discuss the interpretation of the modeled XAS transitions toward discerning the impact of electronic occupation on Ni orbital energies, reflect on the role of structure in determining excited state properties, and present our views on the implications of our findings for potential applications.

2.2.4.1 Evidence for a Transient Ni(I) Center Due to Intramolecular Electron Transfer

In combination with calculated XAS transitions relating transient XANES features to corresponding electronic states, global analysis of the XTA signal as a function of the X-ray photon energy and delay time allowed us to overcome challenges in the assignment of T' to a CT state: (1) the weak T' state signal compared to those of the S_0 and T(d,d) states through the rising-edge; (2) the ambiguity of previous ultrafast optical absorption measurements with regards to changes in the Ni orbital occupation; and (3) the uncertainty of the correlation between the 3d electronic configuration and the energy of the prominent 1s $\rightarrow$ $4p_z$ transition.

Relaxation through a charge transfer (CT) state that produces a transient Ni(I) intermediate has been previously hypothesized based on double-excitation optical methods that observed the relaxation of an excited π electron through d-orbital vacancies in the long-lived T(d,d) state in NiTPP.[111] Such a CT state has also been implicated as the route of excited porphyrin deactivation in Ni tetraphenylporphyrin (NiTPP), Ni octaethylporphyrin (NiOEP), heme,[136] and several other open-shell metalloporphyrins[137] by pump-probe photoelectron spectroscopy measurements in the gas phase, which report fast time constants for the evolution of the NiOEP excited state absorption very similar to this work (100 fs and 1.2 ps).

A short-lived CT state, T', is compatible with the population of the T(d,d) state on the picosecond time scale as observed by previous studies,[130,138] although these did not implicate a charge transfer state and depicted the $S_1(\pi, \pi^*)$ relaxation process as the direct transfer of the excitation to the metal center, resulting in a hot T(d,d) state. Vibrational relaxation of the hot T(d,d) state was observed within 10-20 ps.

During this period, vibrational relaxation processes likely occur and these results do not preclude the involvement of an unrelaxed T(d,d) state in the S_1 decay. However, a purely vibrational model that does not assign T' as a CT state is not as well supported by the current analysis of the $4p_z$ region, where XANES differences before T(d,d) is fully populated

are ascribed to the rearrangement of the Ni electronic structure. Ni orbital energies calculated for a T(d,d) electronic configuration but an S_0 or S_1 geometry, approximating an unrelaxed T(d,d) state, show that such a state cannot account for the transient signal at 8337 eV due to an overall blue shift in the 1s $\rightarrow$ 4p$_z$ transition (Table 2.3).

Nuclear movement during vibrational relaxation affects the 3d orbital energies, especially those involved in coordination to the porphyrin ring, which is reflected in the dynamics of the 1s $\rightarrow$ 3d transition region as general broadening of the 3d transitions in T(d,d). An increased line width for NiTMP 1s $\rightarrow$ 3d transitions due to conformational heterogeneity was previously observed for the NiTMP ground state.[73] This may provide an explanation of the apparent broadening of 3d transitions at 10 ps when T(d,d) is fully populated, although a full description of the relaxation processes in terms of nuclear movement requires additional measurement with more direct structurally sensitive techniques.

2.2.4.2 XAS Transitions Reflect Photoinduced Electronic Structural Changes in the Metal Center

Because it directly probes transient metal orbital energies and occupancy, XTA on the fs time scale can determine the dynamics of photoinduced metal electronic configuration and orbital energy changes well before thermalization of the excited states. While optical transient absorption measurements can clearly identify the kinetics of $S_1(\pi, \pi^*)$ state decay, they are not able to directly detect optically dark electronic states arising from changes in metal centered electronic occupation or metal orbital energy changes in subsequent excited states. This study has directly obtained energies of the transitions 1s $\rightarrow$ 3d and 1s $\rightarrow$ 4p$_z$ in Ni for different electronic states, from which these properties have been obtained for short-lived transient states.

Changes in the observed Ni K-edge transition features, such as the red shift and subsequent blue shift of the 1s $\rightarrow$ 4p$_z$ transition energy, agreed with the calculated inner shell transitions (Table 2.3) and their energies are interpreted in terms of the evolving electronic configuration. With the assignment of T' to Ni(I), T' state formation can be understood as

the intramolecular charge transfer from the π^* orbital to the $3d_{x^2-y^2}$ orbital. Computational results indicate a rise of the 1s energy by ∼2 eV for the T' electronic configuration, where charge transfer results in greater nuclear shielding and therefore a lower electron binding energy. The rise of the 1s orbital energy in turn reduces the 1s → $4p_z$ transition energy in the T' state. This is identical to the core-level shift seen in X-ray photoelectron spectroscopy (XPS)[139] and the effect of oxidation on K-edge spectra has also been observed in previous XAS experiments.[140,141]

This computed red shift is seen experimentally as the rise and fall of intensity around E1 in <2 ps. Only about 0.2 eV of the ∼2 eV shift in the 1s → $4p_z$ transition energy change from the ground state to the T' state transition is due to the shift of the $4p_z$ orbital energy. Similarly, the blue shift in the 1s → $4p_z$ transition energy of the T(d,d) state can be attributed to a change in the repulsive potential felt by the core electrons as the $3d_{x^2-y^2}$ orbital is far more hybridized with the ligand orbitals than the $3d_{z^2}$ orbital (see Figure S7 in Supplementary Information of Ref. 2). Relative to the ground state, which has a doubly occupied $3d_{z^2}$ and an unoccupied $3d_{x^2-y^2}$ orbital, the T(d,d) state has less electron density around the Ni atom, lowering the 1s orbital energy and blue-shifting the 1s → $4p_z$ transition by 1.5 eV.

As evidenced by the computed changes in the Ni 1s energy experimental 1s → 3d transition energies cannot be solely relied upon to determine changes in d-orbital splitting. Though the 1s → $3d_{x^2-y^2}$ transitions, for example, are within half an eV of each other according to the experimental spectrum, we can expect the $3d_{x^2-y^2}$ orbital energy to change much more significantly to remain consistent with the shifts in the Ni 1s energy. Calculated transition energies (see Supporting Information 4 of Ref. 2) are very similar to those experimentally observed with the possible exception of the T(d,d) state, though even here the trend in the movement of the transitions with respect to the ground state is preserved.

2.2.5 Conclusion

Ultrafast XANES at the Ni K-edge was successfully measured for optically excited Ni(II)TMP on a previously unachievable subpicosecond time scale, providing insight into its ultrafast electronic and structural relaxation processes. Importantly, a transient Ni(I) (π, d) electronic state (T') is implicated as an intermediate through the interpretation of a short-lived excited state absorption. The assignment of this absorption is confirmed by agreement with calculated XAS transitions for the postulated (π, d) electronic states at this energy. The observed and computed inner shell-to-valence orbital transition energies demonstrate and quantify the influence of electronic configuration on specific metal orbital energies. The strong influence of the valence orbital occupation on the inner shell orbital energies indicates that one should not use the transition energy from 1s alone to draw conclusions about the d-orbital energies of different states. A transient electronic configuration could influence d-orbital energies up to a few eV and any potential photocatalytic application should account for this to ensure that energy levels are well matched and that the photoexcitation can be used optimally in driving desirable processes.

Chapter 3

DEVELOPING NEW MODELS TO DESCRIBE X-RAY ABSORPTION SPECTROSCOPY

3.1 Energy-specific Equation-of-motion Coupled Cluster Theory

Single-reference techniques based on coupled cluster (CC) theory, in the forms of linear response (LR) or equation of motion (EOM), are highly accurate and widely used approaches for modeling valence absorption spectra. Unfortunately, these equations with singles and doubles (LR-CCSD and EOM-CCSD) scale as $\mathcal{O}(N^6)$, which may be prohibitively expensive for the study of high-energy excited-states using a conventional eigensolver. In this paper, we present an energy-specific non-Hermitian eigensolver that is able to obtain high-energy excited-states (e.g., XAS K-edge spectrum) at low computational cost. In addition, we also introduce an improved trial vector for iteratively solving the EOM-CCSD equation with a focus on high-energy eigenstates. The energy-specific EOM-CCSD approach and its low-scaling alternatives are applied to calculations of carbon, nitrogen, oxygen, and sulfur K-edge excitations. The results are compared to other implementations of CCSD for excited-states, energy-specific linear response time-dependent density functional theory (TDDFT), and experimental results with multiple statistical metrics are presented and evaluated. The work presented in this section is adapted with permission from B. Peng, P. J. Lestrange, J. J. Goings, M. Caricato, X. Li, *J. Chem. Theory Comput.*, **2015**, *11*, 4146-4153.[142] Copyright 2015 American Chemical Society.

3.1.1 Introduction

Due to its complexity, XAS often relies on theoretical insight for interpretation. As in lower-energy absorption spectroscopy, variants of time-dependent density functional theory

(TDDFT)[10–12] are the most frequently used methods. The restricted excitation window (REW-TDDFT)[30–33] and energy-specific (ES-TDDFT)[1,22,33] TDDFT approaches are now routinely used to model XAS. The REW-TDDFT method restricts solutions to only include transitions from orbitals deemed relevant to a particular region of the spectrum, whereas the ES-TDDFT approach searches for solutions in the full orbital space with a constraint on the eigenvalues. These two different numerical approaches have been shown to produce nearly identical X-ray K-edge spectra because excitations from the $1s$ (K-edge) orbital are rather localized in the orbital space.[34] Variations of the ΔSCF approach,[25] such as the transition-potential DFT[26,27] and the orthogonality constrained DFT,[28,29] which require the preparation of a core-hole single-determinant state, have been successfully applied to X-ray absorption spectroscopy. From the DFT kernel perspective, there has also been interest in developing short-range corrected functionals that improve the description of core correlation and reduce the self-interaction error specifically for XAS.[68,69]

Wave function-based approaches, while more expensive, are inherently free of the self-interaction error and can be systematically improved. For example, single-reference techniques based on coupled cluster (CC) theory, in the forms of linear response (LR)[143,144] or equation-of-motion (EOM),[145,146] are highly accurate and widely used approaches for modeling valence absorption spectra.[8,147] Unfortunately, these equations with singles and doubles (LR-CCSD and EOM-CCSD) scale as $\mathcal{O}(N^6)$, which may be prohibitively expensive for the study of large molecular systems. This high computational cost has prompted the development of many low-scaling approximations to EOM-CCSD and LR-CCSD. The EOM-MBPT2 equation is obtained by truncating the perturbative expansion of the cluster operator at second-order.[148,149] This approach still scales as $\mathcal{O}(N^6)$ but with a much smaller prefactor than that of EOM-CCSD. Partitioned EOM-MBPT2 (P-EOM-MBPT2) is an iterative $\mathcal{O}(N^5)$ approach that makes the further approximation that the doubles-doubles block of the Hamiltonian can be treated as diagonal.[149–151] While these techniques have been extensively used in obtaining low-lying excited-states, they have not been applied to the study of core excitations, although further approximations to these techniques have been

used previously with varying success.

Beyond coupled cluster, there are other wave function and Green's function-based methods to study high-energy excited-states. The CIS(D_∞) approach can be related to P-EOM-MBPT2 by treating the singles-doubles blocks of the Hamiltonian to first-order only.[152] The second-order algebraic-diagrammatic construction approach (ADC(2)) is a symmetrized form of CIS(D_∞) that has been previously used to model XAS.[153–155] The core valence separation approximation (CVS)[156] is employed to reduce the dimension of the problem by only including excitations from the relevant core orbitals, however, there is an estimated 0.5-1.0 eV error associated with the CVS approximation.[154,157,158] The closely related CIS(D) method applies a non-iterative doubles correction to excitation energies obtain from configuration interaction singles (CIS).[159,160] By using the REW approach, CIS(D) can be used to model core-excitations, but has been known to provide qualitatively incorrect spectra in some cases.[161]

Where core excitations are concerned, direct applications of EOM-CCSD and its closely-related derivatives are computationally intractable due to the large space where the excited-states of interest reside. The electron-attachment EOM-CCSD (EA-EOM-CCSD)[162] has been used previously to investigate K-edge transitions in small molecules, relying on the validity and availability of a core-hole reference state. Recently, an equation-of-motion multi-reference coupled cluster including singles and doubles (EOM-MRCCSD) method has been developed to obtain core excitations in the coupled cluster framework.[163–165] The EOM-MRCCSD approach for XAS is based on construction of a core-hole reference in a select subspace spanned by active core, occupied, and unoccupied spin-orbitals of interest. Recently, a complex polarization propagator formulation of coupled cluster response theory (CPP-CC) has been applied to model X-ray absorption among other properties.[166–168] This formalism can be used for many different coupled cluster approaches truncated at different levels (CCS, CC2, CCSD, CCSD(3)). Unlike EOM-CC which solves for resonant frequencies or poles of the response function, the CPP-CC method solves a damped frequency dependent response function. This technique is able to resolve the off-resonant response of the system,

but requires the solution of many frequency-dependent problems.

In this section, we present an energy-specific non-Hermitian eigensolver with improved trial vectors to efficiently solve the EOM-CCSD equation for high-energy core excitations. This approach utilizes low-scaling approximations of EOM-CCSD to refine trial vectors, followed by iterative eigenvalue-screening, eigenvector-bracketing and growing-window techniques to search for high-energy solutions in the full orbital space. The strategy used throughout is a non-Hermitian generalization of our previously developed energy-specific algorithm applied in TDDFT.[1] This strategy will allow these highly accurate single-reference wave function methods to be routinely applied to the study of core excitations.

3.1.2 Method

3.1.2.1 Brief Review of EOM-CCSD, EOM-MBPT2 and P-EOM-MBPT2

For two excellent articles of coupled cluster theory, see the review by Crawford and Schaefer[169] and the book by Shavitt and Bartlett.[147] In the present work we adopt the notation that indices i, j, k, l refer to occupied orbitals, a, b, c, d refer to virtual orbitals, and p, q, r, s refer to any orbital.

The generalized CC Schrödinger equation may be written as

$$\bar{H}\,\hat{R}(m)\,|\Phi_0\rangle = E_m\,\hat{R}(m)\,|\Phi_0\rangle, \tag{3.1}$$

where $|\Phi_0\rangle$ is the reference wave function, and $\hat{R}(m)$ is the excitation operator for the m-th excited-state with energy E_m. This takes the form,

$$\hat{R}(m) = \hat{R}_1 + \hat{R}_2 + \ldots = \sum_{ia} r_i^a(m)\, a_a^\dagger a_i + \sum_{\substack{i<j \\ a<b}} r_{ij}^{ab}(m)\, a_a^\dagger a_b^\dagger a_j a_i + \ldots. \tag{3.2}$$

where $a^\dagger$ and a are creation and annihilation operators. $\bar{H}$ is the similarity transformation of the bare electronic Hamiltonian $\hat{H}$,

$$\bar{H} = e^{-\hat{T}}\,\hat{H}\,e^{\hat{T}}, \tag{3.3}$$

in which the cluster operator $\hat{T}$ takes the following form,

$$\hat{T} = \hat{T}_1 + \hat{T}_2 + \ldots = \sum_{ia} t_i^a \, a_a^\dagger a_i + \frac{1}{4} \sum_{ijab} t_{ij}^{ab} \, a_a^\dagger a_b^\dagger a_j a_i + \ldots . \tag{3.4}$$

Equation (3.1) represents a right-hand eigenvalue problem, however, Eq. (3.3) makes $\bar{H}$ non-Hermitian. As a result, Eq. (3.1) is different from its associated left-hand eigenvalue problem,

$$\langle \Phi_0 | \, \hat{L}(m) \, \bar{H} = \langle \Phi_0 | \, \hat{L}(m) \, E_m. \tag{3.5}$$

where $\hat{L}(m)$ is the de-excitation operator defined as,

$$\hat{L}(m) = \hat{L}_1 + \hat{L}_2 + \ldots = \sum_{ia} l_a^i(m) \, a_i^\dagger a_a + \sum_{\substack{i<j \\ a<b}} l_{ab}^{ij}(m) \, a_i^\dagger a_j^\dagger a_b a_a + \ldots . \tag{3.6}$$

Note that Eq. (3.1) and Eq. (3.5) share the same eigenvalues (E_m) and the left-hand and right-hand eigenvectors are related to each other through the biorthonormality condition,

$$\langle \Phi_0 | \, \hat{L}(m) \, \hat{R}(n) \, | \Phi_0 \rangle = \delta_{m,n}, \quad m \neq 0 \text{ and } n \neq 0 \tag{3.7}$$

such that the generalized CC energy expression can be obtained,

$$E_m = \langle \Phi_0 | \, \hat{L}(m) \, \bar{H} \, \hat{R}(m) \, | \Phi_0 \rangle. \tag{3.8}$$

In order to calculate electronic excitation energies, it is convenient to define a normal-ordered Hamiltonian, $\bar{H}_N$, by

$$\bar{H}_N = \bar{H} - E_0, \tag{3.9}$$

where E_0 is the energy associated with ground state wave function $|\Phi_0\rangle$. Then, Eq. (3.8) can be rewritten as

$$\omega_m = \langle \Phi_0 | \, \hat{L}(m) \, \bar{H}_N \, \hat{R}(m) \, | \Phi_0 \rangle \tag{3.10}$$

where ω_m is the m-th excitation energy.

Within the framework of EOM-CCSD method, $\hat{L}$ and $\hat{R}$ are truncated to the second order, the excitation energies are obtained by diagonalizing the EOM-CCSD Hamiltonian

matrix,

$$\mathbf{H}_{EOM-CCSD} = \begin{bmatrix} \bar{\mathbf{H}}^{SS} & \bar{\mathbf{H}}^{SD} \\ \bar{\mathbf{H}}^{DS} & \bar{\mathbf{H}}^{DD} \end{bmatrix} \tag{3.11}$$

$$\bar{H}^{SS}_{ai,ck} = \langle \Phi^a_i | \, \bar{H}_N \, | \Phi^c_k \rangle$$

$$\bar{H}^{SD}_{ai,cdkl} = \langle \Phi^a_i | \, \bar{H}_N \, | \Phi^{cd}_{kl} \rangle$$

$$\bar{H}^{DS}_{abij,ck} = \langle \Phi^{ab}_{ij} | \, \bar{H}_N \, | \Phi^c_k \rangle$$

$$\bar{H}^{DD}_{abij,cdkl} = \langle \Phi^{ab}_{ij} | \, \bar{H}_N \, | \Phi^{cd}_{kl} \rangle$$

where $|\Phi^c_k\rangle, |\Phi^{cd}_{kl}\rangle$ are singly and doubly excited determinants, respectively. The overall dimension of Eq. (3.11) is $OV + O^2V^2$ where O and V are the numbers of occupied and virtual orbitals. EOM-CCSD scales as $\mathcal{O}(N^6)$ and a lower-scaling approximation can be obtained by only keeping terms in the perturbative expansion of the cluster operator through second order. This gives rise to the EOM-MBPT2 Hamiltonian matrix,[148,150,151]

$$\mathbf{H}_{EOM-MBPT2} = \begin{bmatrix} \bar{\mathbf{H}}^{SS(2)} & \bar{\mathbf{H}}^{SD(2)} \\ \bar{\mathbf{H}}^{DS(2)} & \bar{\mathbf{H}}^{DD(2)} \end{bmatrix}, \tag{3.12}$$

where $\bar{\mathbf{H}}^{(2)}_{SS}$ is the singles-singles block of the Hamiltonian, $\bar{\mathbf{H}}_{SS}$, through second order, and so on. This approximation neglects the numerous $\hat{T}_1$ terms, as $\hat{T}^{(1)}_1$ equals zero in the perturbative approach, and only needs the $\hat{T}^{(1)}_2$ amplitudes, which are determined through

$$t^{ab\,(1)}_{ij} = \frac{\langle i\, j \,\|a\, b\rangle}{\epsilon_i + \epsilon_j - \epsilon_a - \epsilon_b}, \tag{3.13}$$

where ϵ's are the Hartree-Fock molecular orbital energies.

EOM-MBPT2 is still a $\mathcal{O}(N^6)$ method, but with a much smaller prefactor than EOM-CCSD. Further approximation can be made by replacing $\bar{\mathbf{H}}^{DD(2)}$ with its zeroth order based on Löwdin partitioning approach[170] to give rise to an iterative $\mathcal{O}(N^5)$ method, the so-called partitioned EOM-MBPT2 (P-EOM-MBPT2).[150,151,170] The P-EOM-MBPT2 Hamiltonian is

$$\mathbf{H}_{P-EOM-MBPT2} = \begin{bmatrix} \bar{\mathbf{H}}^{SS(2)} & \bar{\mathbf{H}}^{SD(2)} \\ \bar{\mathbf{H}}^{DS(2)} & \bar{\mathbf{H}}^{DD(0)} \end{bmatrix}, \tag{3.14}$$

where $\bar{\mathbf{H}}^{DD(0)} = \epsilon_a + \epsilon_b - \epsilon_i - \epsilon_j$.

In practice, due to the non-Hermitian nature of Hamiltonians in Eq. (3.11), Eq. (3.12), and Eq. (3.14), and their large matrix dimension (roughly O^2V^2), the most efficient computational approach to find the lowest eigenvalues and corresponding left and right eigenvectors is a modified version of Davidson algorithm.[171–174] However, core excitations in XAS usually exhibit high excitation energies ranging from hundreds to thousands eV, and are thus far away from low-lying excited-states. It is then impractical for the conventional EOM methods mentioned above to capture these high-energy excited-states because ordinary solvers require that all lower-energy solutions be obtained before any higher-energy solution.

3.1.2.2 Improved Trial Vectors for High-Energy Excited States

Davidson-like eigensolvers usually initialize with a set of well-defined guess vectors, and the quality of these guess vectors subsequently affects the convergence speed in iterative methods for eigenvalue problems. In TDDFT, trial vectors constructed from simple occupied to virtual orbital transitions have proven to be quite reasonable. However, such trial vectors are usually far from the converged EOM-CCSD solution and as a result they may lead to excessive iterations with Davidson-like eigensolvers. A better and widely used trial vector scheme for EOM-CCSD in practice starts with the solution of configuration interaction singles (CIS). However, generating trial vectors for high-energy excited-states using conventional CIS calculations is impractically expensive with conventional techniques. As a result, the feasibility of applying EOM-CCSD approach for XAS calculations depends on the availability of appropriate trial vectors and efficient solvers that can obtain the high-energy eigenvectors of interest. In this work, we develop a two-step strategy to generate appropriate trial vectors that aims to enable EOM-CCSD and its low-scaling approximations to study high-energy excitations such as those probed by XAS.

Assume that M excited-states with energies greater than ω_0 are the subject of interest to be investigated using EOM-CCSD. In the first step, high-energy trial vectors are generated using the energy-specific eigensolvers with low-scaling excited-state methods such as CIS

and P-EOM-MBPT2. For CIS, the Hermitian energy-specific algorithm[1] is used to obtain m eigenvectors ($m \geq M$, $\omega \geq \omega_0$) as trial vectors for the following calculation. As the CIS approach does not take into account electron correlation, their eigenvectors can be poor guesses for high-energy excited-states as contributions from $\hat{T}_2$ become more important.[149] In fact, in our test cases, searching for high-energy eigenvectors in EOM-CCSD framework usually takes many more iterations compared to those for valence excitations. Any improvement to expedite solving the EOM-CCSD equations for high-energy excited-states will be appreciated.

To improve the CIS vectors for high-energy EOM-CCSD calculations, we introduce a second step to refine the trial vectors using the $\mathcal{O}(N^5)$ P-EOM-MBPT2 approach with a non-Hermitian energy-specific eigensolver which will be introduced later in this paper. The refined trial vectors will be used together with the non-Hermitian energy-specific eigensolver to obtain solutions of the EOM-CCSD equation. In the following discussion, methods that utilize the energy-specific eigensolver (Hermitian or non-Hermitian) will have the "ES-" prefix in order to distinguish the results from those using conventional algorithms.

Figure 3.1 shows the effect of the quality of different trial vectors on the convergence behavior of an ES-EOM-CCSD calculation of a carbon K-edge excitation of CO. Two different tight convergence criteria, the residual norm and the change in excitation energy, are considered in this comparison. For both criteria, EOM-CCSD using the P-EOM-MBPT2 eigenvectors as trial vectors exhibits ∼20% savings in computational cost. Note that the cost of computing ES-P-EOM-MBPT2 eigenvectors is trivial compared to the cost of solving $\mathcal{O}(N^6)$ EOM-CCSD equation. This test case suggests that P-EOM-MBPT2 eigenvectors are a better choice over the CIS trial vectors for ES-EOM-CCSD calculations.

3.1.2.3 Non-Hermitian Energy-Specific Eigensolver

In this work, we introduce a non-Hermitian energy-specific eigensolver for EOM-CCSD and its low-scaling approximations to efficiently compute high-energy excited-states. The discussion starts with a set of left $\mathbf{L} = \{L_1, \ldots, L_m\}$ and right $\mathbf{R} = \{R_1, \ldots, R_m\}$ trial vectors

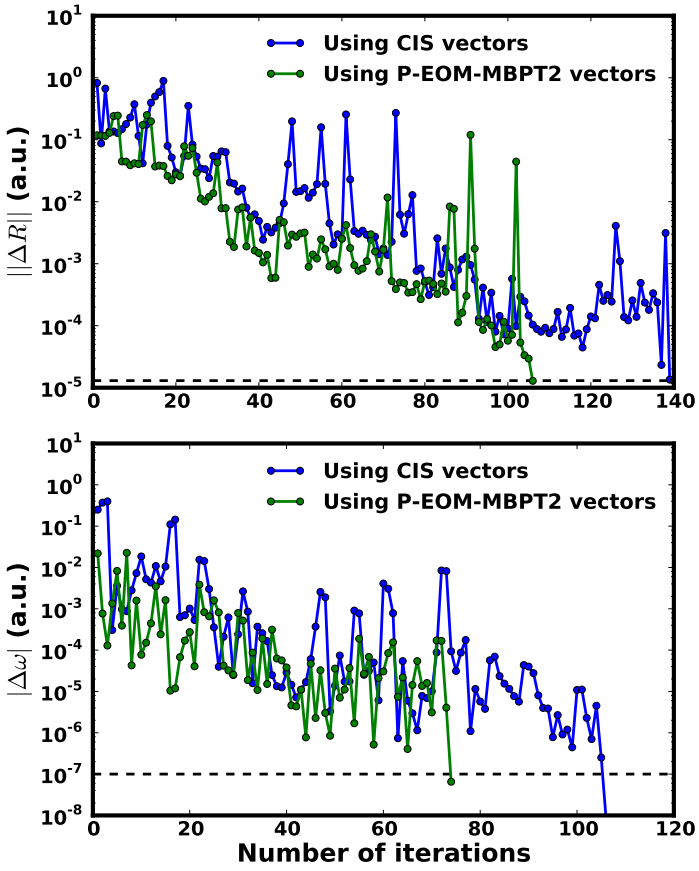

Figure 3.1. Comparison of the convergence behaviors of ES-EOM-CCSD calculations using CIS and P-EOM-MBPT2 trial vectors for the carbon $1s \rightarrow 2p\pi^*$ transition of CO. The residual norm of the right eigenvector (top panel) and the absolute change of eigenvalues (bottom panel) are plotted against the number of iterations. The basis set used is 6-311G$**$. The calculated excitation energy is 288.32 eV.

in the full orbital space that correspond to initial guesses of high-energy excited-states generated using the two-step strategy presented above. Note that the left and right vectors are related by the biorthonormalization condition (Eq. (3.7)). The EOM Hamiltonian **H**,

Eq. (3.11), is projected onto the subspace spanned by the trial vectors,

$$\mathbf{h} = \mathbf{L}^{\dagger}\mathbf{H}\mathbf{R} \tag{3.15}$$

The EOM Hamiltonian in the reduced space $\mathbf{h}$ is then diagonalized to obtain a new set of left $\mathbf{l} = \{l_1, \ldots, l_m\}$ and right $\mathbf{r} = \{r_1, \ldots, r_m\}$ eigenvectors and eigenvalues $\boldsymbol{\omega} = \{\omega_1, \ldots, \omega_m\}$. Eigenpairs in the reduced space are screened and only the ones with associated eigenvalues above the desired energy threshold ω_0 are kept. The transformation of these qualified eigenpairs from the reduced space to the full orbital space yields the new approximate eigenvectors,

$$\tilde{\mathbf{R}} = \mathbf{R}\mathbf{r}, \qquad \tilde{\mathbf{L}} = \mathbf{L}\mathbf{l}. \tag{3.16}$$

Equation (3.7) is used to ensure the new left and right eigenvectors are biorthonormalized. To test the convergence, the eigenvector residuals of states of interest are computed

$$\Delta R_k = (\mathbf{H} - \mathbf{I}\omega_k)\, R_k \tag{3.17}$$

$$\Delta L_k = \left(\mathbf{H}^{\dagger} - \mathbf{I}\omega_k\right) L_k \tag{3.18}$$

If some of the norms of residuals are still above the pre-defined threshold, perturbation vectors are generated using the following equation,

$$R'_k = \left(\mathbf{I}\omega_k - \mathbf{H}_D\right)^{-1} \Delta R_k \tag{3.19}$$

$$L'_k = \left(\mathbf{I}\omega_k - \mathbf{H}_D\right)^{-1} \Delta L_k \tag{3.20}$$

where $\mathbf{H}_D$ are the diagonal elements of the $\mathbf{H}$ matrix.[171,172] In our implementation, as in previous studies,[173,175] $\mathbf{H}_D$ is approximated by the corresponding orbital energy differences. The perturbation vectors are biorthonormalized and added to $\mathbf{R}$ and $\mathbf{L}$ to form the new subspace for the next iteration starting from Eq. (3.15). If complex eigenvalues are obtained in the intermediate iteration, the space of $\mathbf{R}$ and $\mathbf{L}$ needs to be increased. The larger number of expansion vectors can not only benefit the elimination of complex eigenvalues, but also help

to accelerate the convergence.[11,173] This process is repeated until the norm of the residuals are below the desired threshold.

The two-step calculation strategy and energy-screening and eigenvector-bracketing technique introduced above avoids the scan through low-lying excited-states in EOM calculations, as well as improving the quality of trial vectors for EOM-CCSD calculation by using converged eigenvectors associated with the high excited-states from low-scaling EOM calculations. This makes it possible to calculate high-energy excited-states with coupled cluster theory.

3.1.3 Benchmarks and Discussion

Energy-specific variations of EOM-CCSD, EOM-MBPT2, and P-EOM-MBPT2 have been implemented and tested in a development version of the Gaussian software package.[35] For all excited-state calculations, the convergence is obtained when (i) the norm of the residual vectors is below a threshold, 10^{-5} a. u., as recommended by Stanton and Bartlett;[145] or (ii) the change in the eigenvalues is less than 10^{-7} a.u.[173] All ground state geometries were optimized at the CCSD level with the def2-TZVPD basis set.[58–60,176]

Table 3.1. Comparison of conventional EOM-CCSD and ES-EOM-CCSD for select low-lying excited-states of carbon monoxide computed with the def2-TZVPD basis set (eV). The energy threshold for the energy-specific calculations is 11.2 eV.

State	Transition	ES-EOM-CCSD	EOM-CCSD
$B\,^1\Sigma^+$	$\sigma \rightarrow 3s$	11.27	11.27
$C\,^1\Sigma^+$	$\sigma \rightarrow 3p\sigma$	12.30	12.30
$E\,^1\Pi$	$\sigma \rightarrow 3p\pi$	12.32	12.32
$F\,^1\Sigma^+$	$\sigma \rightarrow 3d\sigma$	13.53	13.53

As discussed in the Methods section, the energy-specific eigensolver is able to obtain

the exact solutions represented in the full space. This has been verified by benchmark calculations on select excited-states using the ES-EOM-CCSD method compared to those obtained by full EOM-CCSD calculations including low-lying states. In Tab. 3.1, the results from ES-EOM-CCSD and EOM-CCSD are numerically identical, suggesting that the energy-specific approach is able to obtain the exact excited-states even though low-lying states are not considered in the eigenvector search algorithm. As the full EOM-CCSD calculation has to include extra low-lying states in order to locate the states in the targeted energy range, it unavoidably incurs additional two-fold computational cost compared to the ES-EOM-CCSD method in this test case. Assuming the number of excited-states (i.e. the number of $\mathbf{R}$ and $\mathbf{L}$ vectors) grows linearly with respect to the excitation energy, the computational cost of each EOM-CCSD iteration will grow linearly with respect to the energy of the targeted states. For core-electron excitations, the cost of the conventional EOM-CCSD approach becomes intractable. In contrast, the computational cost of ES-EOM-CCSD is nearly constant because the search space is in principle invariant to the excitation energy range of interest.

The quality of the ES-EOM-CCSD approach is also compared to other implementations/approximations of CC method to XAS. Table 3.2 compares oxygen K-edge excitations of H_2O obtained using ES-EOM-CCSD to those computed using multi-reference EOM-MRCCSD[163–165] and single-reference CPP-CCSD.[177] Table 3.3 shows ES-EOM-CCSD and EA-EOM-CCSD[162] results for K-edge excitations of a select test set. This comparison shows that, for the limited number of test cases, ES-EOM-CCSD results are in excellent agreement with the results from other coupled cluster methods. The difference between ES-EOM-CCSD and EA-EOM-CCSD can be attributed to the different reference used in the calculation. The EA-EOM-CCSD method requires a pre-defined core-hole reference that accounts for some amount of core-hole relaxation. Therefore, the EA-EOM-CCSD results can be of higher accuracy, although they strongly depend on the quality and existence of the core-hole reference.

Excitation energies of a set of 31 K-edge transitions for carbon, nitrogen, and oxygen, of seven molecules (CO, CH_2O, C_2H_4, N_2, NH_3, NO_2, H_2O) are calculated with ES-EOM-CC methods (see Supporting Information in Ref. 142 for details). The results are compared

Table 3.2. Comparison of ES-EOM-CCSD with multi-reference EOM-MRCCSD[163–165] method and single-reference CPP-CCSD[177] method for select core-excitations of H_2O (in eV).

Excitation	Basis	ES-EOM-CCSD	EOM-MRCCSD	CPP-CCSD[177]	Experiment[40]
$1a_1 \rightarrow 4a_1$	6-311G**	535.72	535.76[163]	–	534.00
	cc-pVDZ	538.36	538.40[163,164]	–	
	cc-pVTZ	535.41	535.34[164]	–	
	aug-cc-pVTZ	535.30	535.32[165]	–	
	aug-cc-pCVTZ	535.66	–	535.68	
$1a_1 \rightarrow 2b_1$	6-311G**	537.57	537.61[163]	–	535.90
	cc-pVDZ	540.17	540.21[163,164]	–	
	cc-pVTZ	537.22	537.13[164]	–	
	aug-cc-pVTZ	537.08	537.11[165]	–	
	aug-cc-pCVTZ	537.44	–	537.47	

with results from gaseous XAS or inner-shell electron energy loss spectroscopy (ISEELS) experiments.[36–42] The mean absolute/signed error (MAE/MSE), root mean square (RMS) error, maximum absolute error (Max AE), mean standard error (MSE) and standard deviation (StDev) of the errors with respect to experimental results are statistically evaluated. Energy-specific TDDFT (ES-TDDFT)[1] results are also included for comparison. Two density functionals, BHandHLYP[43] and PBE1PBE[46,47] were used as they have been shown to consistently perform well for predicting K-edge spectra.[22]

Table 3.4 lists error analyses of absolute and shifted K-edge excitation energies (300-500 eV for these systems) obtained with different methods and the doubly augmented Dunning basis with flexible core orbitals (d-aug-cc-pCVDZ).[63,64] While absolute excitation energies are direct measurement of the accuracy of a method, uniform shifts are often applied to calculated XAS to account for the lack of relativistic effects and higher-order correlations.[32,66,67] For error analyses of shifted results, the calculated excitation energies are uniformly shifted so

Table 3.3. Comparison of ES-EOM-CCSD with EA-EOM-CCSD[162] for select core-excitations. The EA-EOM-CCSD results are based on pre-defined core-hole reference states, and the latter is obtained from a so-called quasi-RHF (QRHF) calculation.[178–180] A modified Sadlej basis set is used in both calculations, where some atomic s and p functions are uncontracted from the original Sadlej basis set (see Ref. 162 for more details).

Molecule	Core	Excitation	ES-EOM-CCSD	EA-EOM-CCSD[162]	Experiment
CO	Carbon	$2\sigma \rightarrow 2\pi$	287.99	287.08	287.40[38]
	Oxygen	$1\sigma \rightarrow 2\pi$	535.52	534.15	534.21[181]
C_2H_2	Carbon	$1\sigma_u \rightarrow 1\pi_g(2p)$	286.70	286.21	285.81[182]
C_2H_4	Carbon	$1b_{1u} \rightarrow 1b_{2g}(2p)$	285.87	285.16	284.87[182]
N_2	Nitrogen	$1\sigma_u \rightarrow 1\pi_g$	401.93	401.73	401.00[183]
CH_2O	Carbon	$2a_1 \rightarrow 2b_1(\pi^*)$	287.57	285.77	286.00[181]
	Oxygen	$1a_1 \rightarrow 2b_1(\pi^*)$	532.43	530.78	530.80[181]

that the lowest-energy transition matches the corresponding experimental value. Errors are calculated using the remaining transitions.

DFT methods (BHandHLYP and PBE1PBE) consistently underestimate absolute K-edge excitation energies, whereas wave function-based methods overestimate the K-edge excitations. The ES-BHandHLYP method surprisingly outperforms even ES-EOM-CCSD. This is due to fortuitous error cancellation in BHandHLYP functional which includes 50% of HF exchange that shifts the spectra to the opposite sign compared to those from pure functionals.[22] For details regarding the performance of ES-TDDFT on XAS calculations, we refer readers to Reference 22.

After the K-edge excitation energies are shifted, the associated errors change significantly. All methods considered herein become more reliable with MAEs of < 1 eV with standard derivation < 0.5 eV. ES-EOM-CCSD shows the best performance in all statistical metrics. It consistently overestimates K-edge excitation energies only by 0.2-0.3 eV.

Table 3.4. Error analyses of calculated 31 K-edge excitation energies (eV). For error analyses of shifted energies, excitation energies are uniformly shifted so that the lowest-energy transition matches the corresponding experimental value. MAE: Mean absolute error. StDev: standard deviation. MSE: mean signed error. RMS: root mean square. Max AE: maximum absolute error. ES-TDDFT results were obtained using the method in Ref. 1 and the basis set used is d-aug-cc-pCVDZ.

	Absolute K-edge Excitations				Shifted K-edge Excitations			
	MAE (StDev)	MSE (StDev)	RMS	Max AE	MAE (StDev)	MSE (StDev)	RMS	Max AE
ES-PBE1PBE	11.68 (1.35)	-11.68 (1.35)	11.75	14.17	0.95 (0.42)	-0.95 (0.42)	1.04	1.67
ES-BHandHLYP	1.99 (0.61)	-1.99 (0.61)	2.08	3.58	0.62 (0.38)	0.45 (0.58)	0.72	1.49
ES-P-EOM-MBPT2	5.24 (0.66)	5.24 (0.66)	5.28	6.92	0.49 (0.34)	-0.18 (0.58)	0.59	1.19
ES-EOM-MBPT2	3.42 (0.57)	3.42 (0.57)	3.46	4.80	0.29 (0.29)	0.23 (0.34)	0.41	0.86
ES-EOM-CCSD	3.11 (0.53)	3.11 (0.53)	3.15	4.37	0.27 (0.26)	0.20 (0.32)	0.37	0.76

The lower-scaling alternatives of ES-EOM-CCSD, as represented by ES-EOM-MBPT2 and ES-P-EOM-MBPT2, also show a consistent overestimation with slightly larger errors, yet still outperform DFT-based methods. Note that the difference between these low-scaling methods and ES-EOM-CCSD is much greater for these core excitations than for valence and Rydberg excitations.[149] Although inclusion of triples has shown to be able to improve the CPP-CCSD results to be within 0.5 eV of the experimental values for Ne, CO, and H_2O,[177] it is formally a $\mathcal{O}(N^7)$ method which is outside the consideration of this work.

As a larger test case, we also applied various energy-specific methods for calculation of the K-edge excitation of sulfur in dibenzolthiophene (DBT, Fig. 3.2). We focus on the two lowest peaks, $1s \rightarrow 3p\pi$ ($\sim$ 2472 eV) and $1s \rightarrow 3\sigma$ ($\sim$ 2474 eV), in the sulfur K-edge XAS spectrum of DBT.[184] Table 3.5 shows the calculated results obtained with different energy-specific methods. ES-EOM-CCSD and its perturbative approximations are very consistent, and only underestimate the sulfur K-edge excitations by no more than 1.7 eV compared to the experimental values. They show a small increase in absolute error compared to those for lighter elements (C, N, O). This increase of error is likely due to a combination of relativistic

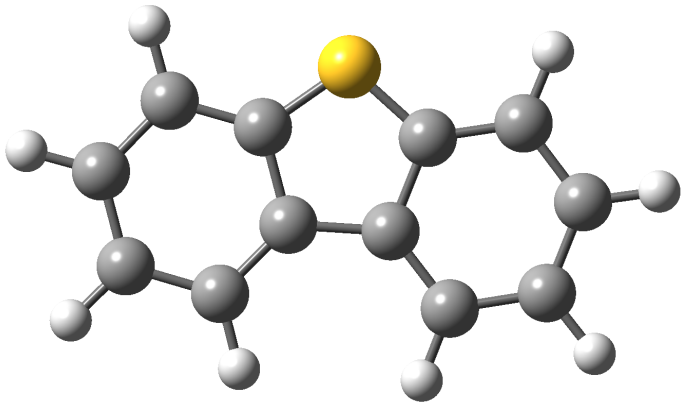

Figure 3.2. Structure of dibenzothiophene (DBT).

effects and basis set incompleteness. The present calculations neglect the relativistic effect. Neglecting the relativistic effect inevitably leads to an underestimation in the computed spectra, and this error becomes larger as the atomic number increases. As a result, the relativistic correction is bigger for sulfur than for light elements (C, N, O). It was estimated to be as large as ∼7 eV for the sulfur 1s level.[184] On the other hand, basis set incompleteness gives rise to an overestimation of the spectrum. For example, Fransson et al.[167] found that, for ethene and its fluoro derivatives, a red-shift of ∼1.3 eV needs to be applied to account for basis set incompleteness for a correlation consistent double-ζ basis set, and a red-shift of ∼0.5 eV for triple corrections for CCSD method. The low-scaling approximations of EOM-CCSD are associated with a larger error due to the basis set incompleteness. As a result, due to the error cancellation, P-EOM-MBPT2 happens to exhibit the best performance with the 6-311++G* basis, although this observation likely won't hold for larger basis sets.

For the K-edge excitation of sulfur, a heavier element than those previously studied, ES-TDDFT with the as-investigated two functionals, PBE1PBE and BHandHLYP severely underestimate the excitations by 20∼50 eV. Obviously, neither the relativistic effect nor the basis set incompleteness can explain the poor performance of TDDFT for sulfur K-

edge excitation. It is likely due to the large self-interaction error in these DFT kernels. Nevertheless, after the computed excitation energies are shifted so that the lowest XAS peak ($1s \rightarrow 3p\pi$) is aligned with the experimental value (2472 eV), all methods show an excellent agreement with the experiment for the second XAS peak ($1s \rightarrow 3p\sigma$).

Table 3.5. Calculated sulfur $1s \rightarrow 3p$ K-edge excitation energies (in eV) for the dibenzothiophene molecule. The basis set used here is 6-311++G*.

	Absolute K-edge Excitations		Shifted K-edge Excitations
	$1s \rightarrow 3p\pi$ (B2)	$1s \rightarrow 3p\sigma$ (A1)	$1s \rightarrow 3p\sigma$ (A1)
Experiment	∼2472	∼2474	∼2474
ES-PBE1PBE	2420.55	2422.26	2473.71
ES-BHandHLYP	2446.19	2448.69	2474.50
ES-P-EOM-MBPT2	2471.29	2473.35	2474.06
ES-EOM-MBPT2	2470.38	2472.68	2474.30
ES-EOM-CCSD	2470.32	2472.56	2474.24

3.1.4 Conclusion

In this chapter, we presented a strategy using the low-scaling P-EOM-MBPT2 approach to improve the trial vectors for solving the EOM-CCSD equation with an emphasis on the high-energy excited-states, e.g. core electron excitations. An energy-specific non-Hermitian Davidson eigensolver, facilitated by the energy-screening, eigenvector-bracketing, and growing-window techniques, has been developed to efficiently obtain high-energy solutions without scanning through low-energy states. With these advances, EOM-CCSD and its low-scaling alternatives can be directly used to compute XAS. Applications to first-row elements (carbon, nitrogen, and oxygen) K-edge XAS of various modules show the wave function-based methods (EOM-CCSD and its low-scaling alternatives) are not obviously advantageous in terms of absolute excitations compared to the spectra predicted by ES-TDDFT using the

BHandHLYP functional. After uniform spectral shift, all methods considered here perform very well for shifted K-edge XAS of first-row elements with ES-EOM-CCSD marginally outperforming DFT and low-scaling alternatives in all statistical metrics. For K-edge XAS of heavier element, sulfur, EOM-CCSD and its low-scaling alternatives maintain the excellent performance while TDDFT severely underestimates the excitation energies.

3.2 The Consequences of Going Beyond the Dipole Approximation

The interaction between a quantum mechanical system and plane wave light is usually modeled within the electric-dipole approximation. This assumes that the intensity of the incident field is constant over the length of the system and transition probabilities are described in terms of the electric-dipole transition moment. For short-wavelength spectroscopies, such as X-ray absorption, the electric-dipole approximation often breaks down. Higher order multipoles are then included to describe transition probabilities. The square of the magnetic dipole and electric quadrupole are often included, but this results in an origin-dependent expression for the oscillator strength. The oscillator strength can be made origin-independent if all terms through the same order in the wave vector are retained. We will show the consequences and potential pitfalls of using either of these two expressions. It is shown that the origin-dependent expression may violate the Thomas-Reiche-Kuhn sum rule and the origin-independent expression can result in negative transition probabilities. The work presented in this section is adapted with permission from P. J. Lestrange, F. Egidi, X. Li, *J. Chem. Phys.*, **2015**, *143*, 234103.[185] Copyright 2015 AIP Publishing LLC.

3.2.1 Introduction

The utility of a spectroscopic technique is greatly enhanced by theoretical models that provide a language through which to explain complex phenomena.[186] For many spectroscopies, the strength of the incident field is weak enough that it can be described as a classical perturbation on a quantum mechanical system. A Taylor expansion of the perturbed observable is often introduced and then truncated at some finite order to describe the interaction of the

incident plane wave with the system. In this way, the system's properties can be described in terms of electric and magnetic multipoles.[187,188] Unfortunately, many properties become origin-dependent when described beyond the lowest-order nonzero multipole. This is non-physical and a potential pitfall when using multipole theory, as molecular properties should be origin-independent when described through infinite-order. This non-physical origin dependence has prompted the development of schemes to minimize the origin dependence[67] and the derivation of fully origin-independent expressions[3,189–191] for describing observable molecular properties.

If the wavelength of the incident field is long compared to the size of the system, the Taylor expansion describing the system-wave interaction can be truncated at the first term. This is the well-known electric-dipole approximation (EDA), so-called because the electric-dipole is the relevant multipole for describing molecular transitions. The EDA assumes that the magnitude of the incident field is constant over the length of the system and is commonly used to describe one-photon molecular absorption and emission processes. X-ray absorption spectroscopy (XAS) is an interesting case where the EDA is not always valid. The wavelength of the field can often be < 1 nm and thus comparable to the size of a molecular system.

The most commonly used expression for describing XAS oscillator strengths truncates the Taylor expansion after the second term. This origin-dependent expression is often used in the atomic spectroscopy community.[192,193] There is no ambiguity when defining the origin in atomic spectroscopy and the origin-dependence of the expression is not often considered. However, origin-dependence of computational oscillator strengths is an unavoidable issue for modeling molecular XAS where there is no unambiguously correct way of defining the origin of a multi-atomic system. This issue becomes even more important as molecular XAS spectra nowadays can be computed routinely with low-scaling many-body methods, such as time-dependent density functional theory (TDDFT).[1,22,30–33]

Neese and co-workers have developed a scheme to minimize this origin dependence by using clever choices of the molecular origin.[67] In many ways this is physically satisfying because the molecular origin is often chosen to be within the transition density of a given

excitation and the Taylor expansion of the plane wave is expected to converge more quickly in this region. However, this only marginalizes the origin dependence problem and does not eliminate it completely. It has been recently shown that this origin dependence is due to an incomplete treatment of the oscillator strength through second-order in the wave vector and a rigorously origin-independent second-order expression has been implemented by Jacob and co-workers.[3] It is important to understand that these different oscillator strength expressions may lead to different interpretations and assignments of spectral features. There are also some important nuances, strengths, and deficiencies unique to these expressions that have yet to be explored in the literature. In fact, the use of either expression can lead to surprising consequences, highlighting the need for further developments in this field. In this work, we will compare the complete second-order oscillator strength expression with the more commonly used origin-dependent expression. Some of the noteworthy consequences when using each expression include violation of the Thomas-Reiche-Kuhn sum rule, varying spectral lineshapes and, most surprisingly, possibly computing negative transition probabilities.

3.2.2 Theory

The interaction of a molecular system with an electromagnetic field is often treated semiclassically.[194–196] The incident field is treated as a classical plane wave and the molecular system is described quantum mechanically. The incident electric field $\mathbf{E}$ is described by means of the scalar and vector potentials ϕ and $\mathbf{A}$. We will assume the Coulomb gauge where $\nabla \cdot \mathbf{A} = 0$ and add the further constraint that the scalar potential be zero, $\phi(\mathbf{r}, t) = 0$. This particular choice of gauge is often referred to as the velocity gauge and we will make comparisons later to the so-called length gauge when discussing transition properties below.

3.2.3 The Absorption of Light

The Hamiltonian describing the interaction of a quantum system with a monochromatic electric field in the non-relativistic limit can be written as

$$\hat{H}(t) = \sum_{i}^{N} \frac{1}{2m_e} \left[\hat{\mathbf{p}}_i - \frac{e}{c}\mathbf{A}(\mathbf{r}_i, t)\right]^2 + V(\mathbf{r}_1, \ldots, \mathbf{r}_N) \tag{3.21}$$

where $\hat{\mathbf{p}}_i = -\mathrm{i}\,\hbar\nabla$ and e and m_e are the charge and mass of the electron respectively. The vector potential is defined as

$$\mathbf{A}(\mathbf{r}, t) = -A_0\,\boldsymbol{\varepsilon}\cos(\mathbf{k}\cdot\mathbf{r} - \omega t) \tag{3.22}$$

where A_0 is proportional to the amplitude of the incident electric field. The wave vector $\mathbf{k}$ describes the propagation direction with a magnitude $k = |\mathbf{k}| = \omega/c$. The propagation direction is perpendicular to the polarization vector $\boldsymbol{\varepsilon}$. We can describe the electric field in terms of this vector potential

$$\mathbf{E}(\mathbf{r}, t) = -\frac{1}{c}\frac{\partial \mathbf{A}(\mathbf{r}, t)}{\partial t} = A_0\,k\,\boldsymbol{\varepsilon}\sin(\mathbf{k}\cdot\mathbf{r} - \omega t) \tag{3.23}$$

The Hamiltonian in Eq. (3.21) can be separated into a portion independent of the incident field and the perturbing operator.

$$\hat{H}(t) = \hat{H}_0 + \hat{V}(t) \tag{3.24}$$

where

$$\hat{V}(t) = -\frac{e}{m_e c}\sum_{i} \mathbf{A}(\mathbf{r}_i, t)\cdot\hat{\mathbf{p}}_i \tag{3.25}$$

The strength of the incident field is assumed to be weak and the quadratic terms in $\mathbf{A}$ have been neglected. Using the definitions of the vector potential (Eq. (3.22)), the perturbing operator becomes

$$\hat{V}(t) = \frac{eA_0}{m_e c}\sum_{i} \cos(\mathbf{k}\cdot\mathbf{r}_i - \omega t)(\hat{\mathbf{p}}_i\cdot\boldsymbol{\varepsilon}) \tag{3.26}$$

$$= \hat{V}\exp(-\mathrm{i}\,\omega t) + \hat{V}^*\exp(\mathrm{i}\,\omega t) \tag{3.27}$$

with the interaction potential defined as

$$\hat{V} = \frac{eA_0}{2m_e c} \sum_i \exp(\mathrm{i}\,\mathbf{k}\cdot\mathbf{r}_i)(\hat{\mathbf{p}}_i \cdot \boldsymbol{\varepsilon}) \tag{3.28}$$

This potential can be used with Fermi's golden rule to describe the rate of transition between two states

$$\Gamma_{0n}(\omega) = \frac{2\pi}{\hbar} |\langle 0|\, \hat{V}\, |n\rangle\,|^2 \delta(\omega - \omega_{0n}) \tag{3.29}$$

$$= \frac{\pi A_0^2}{2\hbar c^2} |T_{0n}|^2 \delta(\omega - \omega_{0n}) \tag{3.30}$$

where T_{0n} is the transition moment between state $|0\rangle$ and $|n\rangle$. Following an integration over all frequencies and the inclusion of additional prefactors, we can arrive at the expression for the dimensionless oscillator strength

$$f_{0n} = \frac{2m_e}{e^2 E_{0n}} |T_{0n}|^2 \tag{3.31}$$

where E_{0n} is the transition energy between state $|0\rangle$ and $|n\rangle$. This represents the transition probability between two states relative to a classical electron in a harmonic potential.[195] The experimentally observed absorption intensity is proportional to Eq. (3.31) and the oscillator strength is often convoluted with a broadening function when results are compared with experimental lineshapes.

3.2.4 Multipole Expansion

The perturbing operator (Eq. (3.28)) can be greatly simplified by expanding the plane wave in a Taylor series and truncating at some finite order.

$$\exp(\mathrm{i}\,\mathbf{k}\cdot\mathbf{r}_i) = 1 + \mathrm{i}\,\mathbf{k}\cdot\mathbf{r}_i + \frac{1}{2}(\mathrm{i}\,\mathbf{k}\cdot\mathbf{r}_i)^2 + \cdots \tag{3.32}$$

This expansion is commonly truncated at the first term, leading to the well-known electric-dipole approximation. This assumes that the wavelength of the incident field is long compared to the size of the system and that the intensity of the field is constant over the length of

the system. Within this approximation, the transition moment is simply the electric-dipole (E1) transition moment, expressed in atomic units as

$$\begin{aligned} T_{0n}^{(E1)} &= \sum_i \langle 0| \, \hat{\mathbf{p}}_i \cdot \boldsymbol{\varepsilon} \, |n\rangle \\ &= \boldsymbol{\varepsilon} \cdot \langle 0| \, \hat{\boldsymbol{\mu}} \, |n\rangle \end{aligned} \tag{3.33}$$

For the vast majority of spectroscopic experiments, the molecules are randomly oriented with respect to the incident field. The oscillator strength should therefore be isotropically averaged[197] to account for these random orientations in the ensemble. The isotropically averaged electric-dipole oscillator strength (in atomic units) is

$$\langle f_{0n}^{(E1)} \rangle_{\text{iso}} = \frac{2}{3E_{0n}} | \, \langle 0| \, \hat{\boldsymbol{\mu}} \, |n\rangle \, |^2 \tag{3.34}$$

This expression is zero-order in the wave vector and is commonly used to describe absorption intensities for low energy absorption spectra. However, the EDA is not always valid when the molecular system is very large or the wavelength of the incident field is very small (e.g. X-ray). Additional terms accounting for variation in the field over the length of the molecule should be included in the description of the transition moment and oscillator strength.[198–200] In this case, the Taylor expansion of the plane wave is commonly truncated after the second term.[1,67] This leads to the magnetic dipole (M1) and electric quadrupole (E2) transition moments

$$\begin{aligned} T_{0n}^{(M1)} &= \frac{\mathrm{i}}{2} (\mathbf{k} \times \boldsymbol{\varepsilon}) \cdot \sum_i \langle 0| \, (\mathbf{r}_i \times \hat{\mathbf{p}}_i) \, |n\rangle \\ &= \frac{\mathrm{i}}{2} (\mathbf{k} \times \boldsymbol{\varepsilon}) \cdot \langle 0| \, \hat{\mathbf{m}} \, |n\rangle \end{aligned} \tag{3.35}$$

$$\begin{aligned} T_{0n}^{(E2)} &= \frac{\mathrm{i}}{2} \sum_{\alpha\beta} \sum_i k_\alpha \varepsilon_\beta \, \langle 0| \, r_{i,\alpha} \hat{p}_{i,\beta} + \hat{p}_{i,\alpha} r_{i,\beta} \, |n\rangle \\ &= \frac{\mathrm{i}}{2} \sum_{\alpha\beta} k_\alpha \varepsilon_\beta \, \langle 0| \, \hat{Q}_{\alpha\beta} \, |n\rangle \end{aligned} \tag{3.36}$$

where the Greek indices run over Cartesian coordinates. Contributions from the spin operator will be neglected throughout because states with different M_S values will be degenerate and their spin contributions to the magnetic transition moments will cancel out.[3,201]

With this truncation of the Taylor expansion, all isotropically averaged cross terms become zero and the two additional contributions to the oscillator strength are

$$\langle f_{0n}^{(M1)} \rangle_{\text{iso}} = \frac{\alpha^2}{6} E_{0n} |\langle 0| \hat{\mathbf{m}} |n\rangle|^2 \tag{3.37}$$

$$\langle f_{0n}^{(E2)} \rangle_{\text{iso}} = \frac{\alpha^2}{20} E_{0n} \left[\sum_{\alpha\beta} \langle 0| \hat{Q}_{\alpha\beta} |n\rangle^2 - \frac{1}{3} \left(\sum_{\alpha} \langle 0| \hat{Q}_{\alpha\alpha} |n\rangle \right)^2 \right] \tag{3.38}$$

While the electric-dipole expressions in Eq. (3.33) and Eq. (3.34) are both zero-order in the wave vector, truncating the Taylor expansion after the second term leads to transition moments that are first-order in the wave vector and oscillator strength terms that are second-order.

As is often the case when molecular properties are described beyond the lowest nonzero multipole order, the oscillator strength becomes origin-dependent when the $f_{0n}^{(M1)}$ and $f_{0n}^{(E2)}$ terms are included.[189,190] This is obviously problematic because the obtained physical observable is origin-independent. Bernadotte et al. have recently shown that this origin dependence is due to inconsistent treatment of the oscillator strength through second-order.[3] The additional second-order contributions to the oscillator strength contain the magnetic quadrupole (M2) and the electronic octupole (E3) transition moments.

$$\begin{aligned} T_{0n}^{(M2)} &= -\frac{1}{6} \sum_{\alpha\beta} \sum_{i} (\mathbf{k} \times \boldsymbol{\varepsilon})_\alpha k_\beta \langle 0| r_{i,\beta} (\mathbf{r}_i \times \hat{\mathbf{p}}_i)_\alpha + (\mathbf{r}_i \times \hat{\mathbf{p}}_i)_\alpha r_{i,\beta} |n\rangle \\ &= -\frac{1}{6} \sum_{\alpha\beta} (\mathbf{k} \times \boldsymbol{\varepsilon})_\alpha k_\beta \langle 0| \hat{\mathcal{M}}_{\alpha\beta} |n\rangle \end{aligned} \tag{3.39}$$

$$\begin{aligned} T_{0n}^{(E3)} &= -\frac{1}{6} \sum_{\alpha\beta\gamma} \sum_{i} k_\alpha k_\beta \varepsilon_\gamma \langle 0| r_{i,\alpha} r_{i,\beta} \hat{p}_{i,\gamma} + r_{i,\alpha} \hat{p}_{i,\beta} r_{i,\gamma} + \hat{p}_{i,\alpha} r_{i,\beta} r_{i,\gamma} |n\rangle \\ &= -\frac{1}{6} \sum_{\alpha\beta\gamma} k_\alpha k_\beta \varepsilon_\gamma \langle 0| \hat{O}_{\alpha\beta\gamma} |n\rangle \end{aligned} \tag{3.40}$$

When the magnitude of the transition moment is squared to derive the oscillator strength (Eq. (3.31)), there are two cross terms that include the product between these and the E1

transition moment. The isotropically averaged cross terms are

$$\langle f_{0n}^{(M2)} \rangle_{\text{iso}} = \frac{\alpha^2}{9} E_{0n} \sum_{\alpha\beta\gamma} \epsilon_{\alpha\beta\gamma} \langle 0| \hat{\mu}_\beta |n\rangle \langle 0| \hat{\mathcal{M}}_{\gamma\alpha} |n\rangle \tag{3.41}$$

$$\langle f_{0n}^{(E3)} \rangle_{\text{iso}} = -\frac{2\alpha^2}{45} E_{0n} \sum_{\alpha\beta} \langle 0| \hat{\mu}_\beta |n\rangle \langle 0| \hat{O}_{\alpha\alpha\beta} |n\rangle \tag{3.42}$$

where $\epsilon_{\alpha\beta\gamma}$ is the Levi-Civita tensor. While all second-order terms are individually origin-dependent, these dependencies cancel out when all terms are included. It has also been shown that the oscillator strength is always origin-independent when treated consistently through a finite order in the wave vector.[3]

The spectra obtained from different expressions for the oscillator strength can be strikingly different.

$$f^{(0)} = \langle f_{0n}^{(E1)} \rangle_{\text{iso}} \tag{3.43}$$

$$f^{(E1+E2+M2)} = \langle f_{0n}^{(E1)} \rangle_{\text{iso}} + \langle f_{0n}^{(M1)} \rangle_{\text{iso}} + \langle f_{0n}^{(E2)} \rangle_{\text{iso}} \tag{3.44}$$

$$f^{(2)} = \langle f_{0n}^{(E1)} \rangle_{\text{iso}} + \langle f_{0n}^{(M1)} \rangle_{\text{iso}} + \langle f_{0n}^{(E2)} \rangle_{\text{iso}} + \langle f_{0n}^{(M2)} \rangle_{\text{iso}} + \langle f_{0n}^{(E3)} \rangle_{\text{iso}} \tag{3.45}$$

The transition probabilities calculated with the zero-order expression (Eq. (3.43)) will be strictly zero for dipole-forbidden transitions; the EDA cannot describe quadrupole-allowed transitions. Improper treatment of the oscillator strength through second-order (denoted as $f^{(E1+M1+E2)}$ in Eq. (3.44)) can result in artificial enhancement of transition probabilities and qualitatively wrong spectral shapes that are dependent upon the origin definition. Unlike $f^{(E1+M1+E2)}$, the full second-order expression (Eq. (3.45)) is origin-independent and retains many of the properties expected of an oscillator strength. While the origin-independent expression may be preferable, it is not completely devoid of problems since it is still a truncated form of the complete, infinite-order operator. The failings of the $f^{(E1+M1+E2)}$ expression and some potential problems associated with $f^{(2)}$ are explored in Results and Discussion.

3.2.5 Different Gauges

The electric transition moments in Eqs. (3.33), (3.36) and (3.40) are in their velocity gauge representation. When a complete basis set is used, there are equivalent expressions in which the operator takes a different form.[196] The relationship between these expressions can be shown for the E1 transition moment using the commutation relationship

$$[r_{i,\alpha}, \hat{H}_0] = \frac{\mathrm{i}\hbar}{m_e}\hat{p}_{i,\alpha} \tag{3.46}$$

This relationship can be used with Equation (3.33) to show that the E1 transition moment can also be written (in atomic units) as

$$T_{0n}^{(E1)} = -\mathrm{i}E_{0n}\sum_i \langle 0|\, \mathbf{r}_i \cdot \boldsymbol{\varepsilon}\, |n\rangle \tag{3.47}$$

Similar commutation relationships (see Appendix A of Ref. 3) can be used to show that

$$T_{0n}^{(E2)} = \frac{E_{0n}}{2}\sum_{\alpha\beta}\sum_i k_\alpha \varepsilon_\beta \langle 0|\, r_{i,\alpha} r_{i,\beta}\, |n\rangle \tag{3.48}$$

$$T_{0n}^{(E3)} = \mathrm{i}\frac{E_{0n}}{6}\sum_{\alpha\beta\gamma}\sum_i k_\alpha k_\beta \varepsilon_\gamma \langle 0|\, r_{i,\alpha} r_{i,\beta} r_{i,\gamma}\, |n\rangle \tag{3.49}$$

when a complete basis set is used. These expressions are referred to as the length gauge representations of the electric transition moments. There are also corresponding length gauge expressions for the oscillator strength that are equivalent to those in the velocity gauge when a complete basis set is used.

It is important to note that when the basis set is incomplete, $f^{(2)}$ is only origin-independent in the velocity gauge. The origin dependence of the magnetic multipole integrals can be represented in terms of lower-order magnetic multipoles and velocity gauge electric multipoles. This can be shown by shifting the molecular origin from $\mathbf{O}$ to $\mathbf{O} + \mathbf{a}$.

$$\langle 0|\, \hat{m}_\alpha(\mathbf{O}+\mathbf{a})\, |n\rangle = \langle 0|\, \hat{m}_\alpha(\mathbf{O})\, |n\rangle - \epsilon_{\alpha\beta\gamma} a_\beta \langle 0|\, \hat{\mu}_\gamma\, |n\rangle \tag{3.50}$$

$$\begin{aligned}\langle 0|\, \hat{\mathcal{M}}_{\alpha\beta}(\mathbf{O}+\mathbf{a})\, |n\rangle = {} & \langle 0|\, \hat{\mathcal{M}}_{\alpha\beta}(\mathbf{O})\, |n\rangle - 3a_\beta \langle 0|\, \hat{m}_\alpha(\mathbf{O})\, |n\rangle + \delta_{\alpha\beta}\left(\mathbf{a}\cdot\langle 0|\, \hat{\mathbf{m}}(\mathbf{O})\, |n\rangle\right) \\ & + \sum_{\gamma\delta}\epsilon_{\alpha\gamma\delta}\left[2a_\beta a_\gamma \langle 0|\, \hat{\mu}_\gamma\, |n\rangle - a_\gamma \langle 0|\, \hat{Q}_{\beta\delta}(\mathbf{O})\, |n\rangle\right]\end{aligned} \tag{3.51}$$

For a detailed derivation see the Supporting Information of Ref. 3. For problems of chemical relevance it is usually impractical to use a complete basis set. In order to maintain origin independence, all second-order contributions to the oscillator strength presented in this work will be calculated in the velocity gauge.

The zero-order expression for the oscillator strength is origin-independent in both the length and velocity gauge and there has been considerable debate over the appropriate gauge to describe transition probabilities.[202–205] Recent work on propagating the electronic density in time while coupled to the electric field through the electric-dipole has shown that the length gauge representation tends to be more numerically stable.[196] This is also the gauge most commonly used and is employed for the $f^{(0)}$ results presented in this work. This mixed gauge representation is consistent with that presented by Bernadotte et al. in Ref. 3.

3.2.6 Computational Details

The multipole expansion may be used to describe transition probabilities for any quantum mechanical method able to describe electronic excited states. We will use linear-response time-dependent density functional theory (TDDFT) for our discussion. A formal response theory is appealing because it allows us to discuss the Thomas-Reiche-Kuhn sum rule.[206–208] This sum rule does not hold for approximate response methods such as Configuration Interaction Singles (CIS)[209] and the Tamm-Dancoff approximation (TDA).[12,210]

The X-ray absorption energies and oscillator strengths are calculated using energy-specific TDDFT (ES-TDDFT)[1,22] in a development version of the Gaussian software package.[35] To first order, the density matrix response to the perturbation can be written in terms of excitation and de-excitation amplitudes, which are found by solving the TDDFT equations:

$$\rho(x, x') = \sum_{ia} \left(X_{ia}\varphi_a(x)\varphi_i(x') + Y_{ia}\varphi_i(x)\varphi_a(x') \right) \tag{3.52}$$

where the i and a subscripts refer to occupied and virtual orbitals, respectively. The transition moments between electronic states are calculated as the trace of the transition density with multipole integrals in the MO basis. The $[\mathbf{X} + \mathbf{Y}]$ or $[\mathbf{X} - \mathbf{Y}]$ density is used depending

on if the operator is Hermitian or anti-Hermitian respectively. For example, the length gauge E1 transition moment is calculated as

$$\langle 0| \sum_k r_{k,\alpha} |n\rangle = \sqrt{2} \sum_{ia} \left[X_{ia}^n + Y_{ai}^n \right] \langle \psi_i| \sum_k r_{k,\alpha} |\psi_a\rangle \tag{3.53}$$

where ψ_p are molecular orbitals. For all calculations presented herein, geometries are optimized with the PBE1PBE functional (also known as PBE0)[46,47] and the 6-31+G(d) basis set.[125,126,211–213]

3.2.7 Results and Discussion

3.2.7.1 Thomas-Reiche-Kuhn Sum Rule

Oscillator strengths obtained from TDHF[214] and TDDFT[10] obey the Thomas-Reiche-Kuhn sum rule.[206–208]

$$\sum_i f_{ij} = N \tag{3.54}$$

This says that the sum of all oscillator strengths from a particular state to all others will equal the number of electrons in the system. When the infinite-order expression for the transition moment is used, the oscillator strength is origin-independent and obeys this sum rule in any coordinate system definition. However, if the oscillator strength is treated incompletely at some finite order, the oscillator strength is not guaranteed to satisfy this sum rule. This behavior can be illustrated (in Fig. 3.3) using the $f^{(0)}$, $f^{(E1+M1+E2)}$, and $f^{(2)}$ expressions to model excitations of molecular hydrogen calculated with the PBE1PBE functional and the daug-cc-pVTZ basis set.[61–63] The system is originally oriented along the z-axis with the origin placed at the center of the molecular bond. The origin is then displaced along the x-axis and the sum rule evaluated at all definitions of the origin.

The EDA is, of course, more than sufficient to describe transition probabilities for molecular hydrogen. The zero-order expression is origin-independent and the sum rule is satisfied at all definitions of the origin. When the second-order oscillator strength is treated incompletely, the summation total is wildly inflated as the origin is moved far away from the

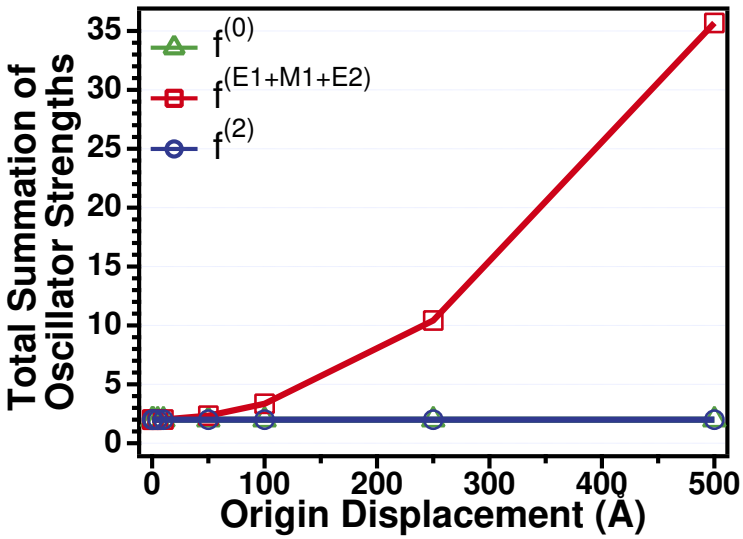

Figure 3.3. The sum of oscillator strengths from 68 excitations of H_2 calculated at the PBE1PBE/daug-cc-pVTZ level of theory. Three different oscillator strength expressions are used: $f^{(0)}$, $f^{(E1+M1+E2)}$, and $f^{(2)}$. Note that the $f^{(0)}$ and $f^{(2)}$ plots overlap almost exactly.

molecular system, rising to > 35 when the origin is displaced by 500 Å. To the best of our knowledge, this behavior of the $f^{(E1+M1+E2)}$ expression has not yet been reported in the literature. This behavior is corrected, however, when the cross terms are included and the complete second-order expression is used. The sum rule is then satisfied at any definition of the origin, as it should be.

This behavior alone is not sufficient to say that $f^{(E1+M1+E2)}$ should not be used because there is no reason to place the molecular origin outside of the molecular system. Those definitions of the origin do not allow one to take advantage of molecular symmetry and reduce computational cost. Also, methods such as CIS and TDA do not satisfy this sum rule and are used to successfully model experimental spectra nonetheless. We will next turn our attention to more reasonable origin definitions contained within the molecular system and show how these still have a large effect on the resulting spectrum when using $f^{(E1+M1+E2)}$.

3.2.7.2 Lineshape Variation

The $f^{(E1+M1+E2)}$ expression can result in very different spectra for different definitions of the origin. We can show this by modeling a derivative of the low bandgap polymer poly[2,6-(4,4-bis-(2-ethylhexyl)-4*H*-cyclopenta[2,1-*b*:3,4-*b*']dithiophene)-alt-4,7(2,1,3-benzothiadiazole)] (PCPDTBT) where the alkyl chains have been replaced with methyl groups (Fig. 3.4). The nitrogen and sulfur K-edges of this system have been previously investigated both experimentally and theoretically.[215,216] We will focus on the sulfur K-edge transitions as the wavelength is about 0.5 nm and a single subunit of this polymer is >1 nm, making it a likely case where the EDA would break down.

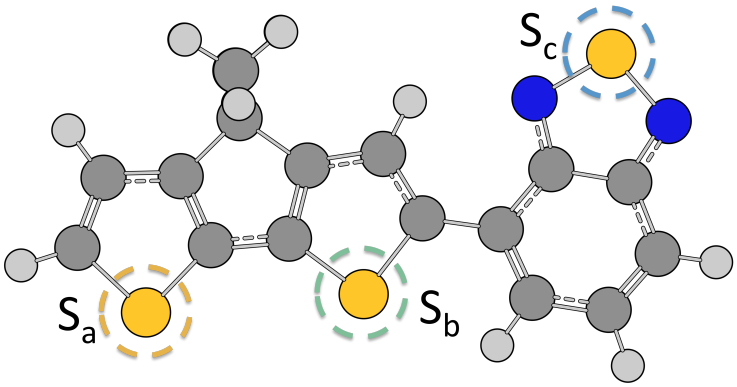

Figure 3.4. A single subunit of the PCPDTBT polymer where the alkyl chains have been replaced with methyl groups. The different sulfur atoms are denoted as S_{a-c} in order to identify different definitions of the origin to compare with their respective spectra in Fig. 3.5.

Spectra using the origin-independent $f^{(0)}$ and $f^{(2)}$ expressions and the origin-dependent $f^{(E1+M1+E2)}$ expression are plotted in Sec. 3.2.7.2. We have placed the origin at the center of mass (COM) of the system and on each sulfur atom (denoted as S_{a-c} in Fig. 3.4) to show the variation in the origin-dependent expression. All transitions are broadened with Lorentzian functions with FWHM of 0.35 eV consistent with the core-hole lifetime for sulfur K-edge

transitions.[18,217]

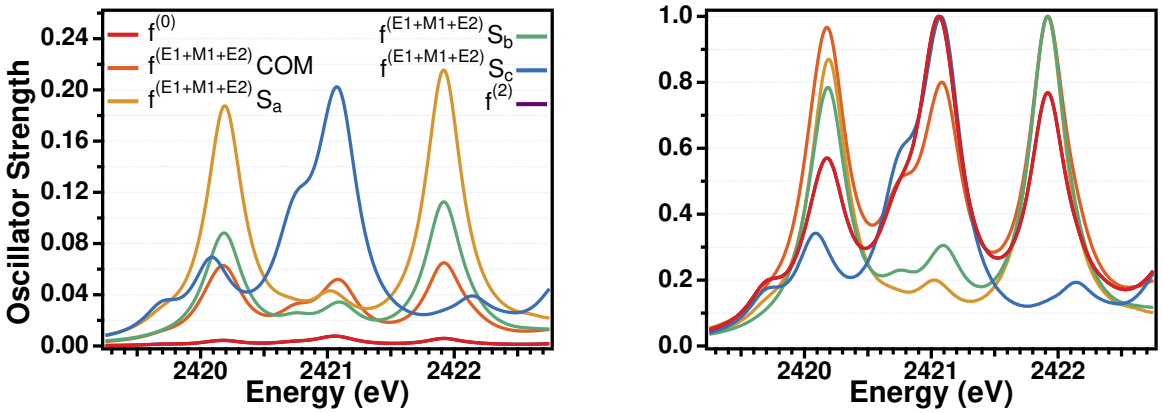

Figure 3.5. Sulfur K-edge spectra of the PCPDTBT derivative in Fig. 3.4. The $f^{(0)}$ and $f^{(2)}$ definitions of the oscillator strength as well as the $f^{(E1+M1+E2)}$ expression with four different definitions of the origin are included. The origin is placed at the COM and on each sulfur atom denoted as S_{a-c}. Note that the $f^{(0)}$ and $f^{(2)}$ spectra overlap almost exactly. The unnormalized and normalized spectra are on the left and right respectively. The individual oscillator strengths are left out for clarity.

All oscillator strengths calculated with $f^{(E1+M1+E2)}$ are far greater than those calculated with $f^{(0)}$ or $f^{(2)}$ (Sec. 3.2.7.2). They also vary dramatically for different definitions of the origin. The zero- and second-order spectra are virtually identical as the cross terms largely cancel out contributions from Eqs. (3.37) and (3.38). This may seem counterintuitive because the size of this system is more than twice the wavelength of the exciting electromagnetic field and the EDA is expected to break down. List et al. have observed similar behavior for *trans*-polyenes of varying length.[191] The modest effect of higher-order contributions was attributed to the localized nature of the initial state which confines the transition density around the core hole. The PCPDTBT transitions are all localized around the excited atom, which explains the very small change when going beyond the EDA. Further, the largest possible

error due to the EDA is about 20% so we would only ever expect a small effect for these dipole-allowed transitions.[191]

When comparing to experimental results, modeled spectra are rescaled in order to compare with the experimental intensities. With this in mind, it is important to consider how the different oscillator strength expressions can change the relative peak intensities and overall spectral features and not just the overall intensity. Section 3.2.7.2 contains normalized spectra such that the strongest transition is set to unity. There are three dominant transitions with the middle transition often having a shoulder slightly lower in energy. For the $f^{(E1+M1+E2)}$ expression, when the origin is place on S_a or S_b the middle transition is strongly dampened and when the origin is placed on S_c this feature is strongly enhanced relative to the other peaks. This origin-dependent enhancement of features can be rationalized in terms of where the excitation is localized on the system.

The core hole of the dominant transitions for the features around 2420 and 2422 eV is localized on S_c. The dominant transition contributing to the feature around 2421 eV has the core hole localized on S_a. When the origin is placed on the excited sulfur atom, the oscillator strength calculated with $f^{(E1+M1+E2)}$ is much closer to that calculated with $f^{(0)}$ or $f^{(2)}$ (evident in Sec. 3.2.7.2). The reverse is also true: when the origin is placed far from the excited atom, the oscillator strength calculated with $f^{(E1+M1+E2)}$ is artificially enhanced relative to the correct value. This behavior is consistent with that seen by Neese and co-workers and one of the arguments for placing the origin within the transition density so the Taylor series expansion of the plane wave converges more quickly.[67] With the origin placed at the COM, the three features all have comparable intensities, although the relative magnitude of the three features is still not consistent with the $f^{(0)}$ and $f^{(2)}$ expressions. This enhancement and dampening of features could be mitigated by changing the molecular origin to be within the the transition density of each excitation although this would be rather tedious as well as computationally inefficient.

An incomplete treatment of the oscillator strength through second-order can result in variable spectral shapes dependent upon the location of the origin and the localization of

the transition densities. This can result in the dampening of important features and the enhancement of features that are insignificant experimentally. This is particularly troubling when $f^{(E1+M1+E2)}$ is used because spectral features may be misassigned and the experiment interpreted incorrectly if too much confidence is placed in the theoretical model. Although much of this can be accounted for by shifting the origin for each transition to be within the transition density. In short, the $f^{(E1+M1+E2)}$ expression is not an appropriate way to model the oscillator strength unless particular care is taken when defining the molecular origin. The $f^{(2)}$ expression, on the other hand, does not require this type of consideration and is always independent of the coordinate system.

3.2.7.3 Negative Oscillator Strengths

The oscillator strength is a measure of transition probability and should always be positive for absorption processes, although it can be negative for emission.[194] The $f^{(0)}$ and $f^{(E1+M1+E2)}$ expressions are always positive because they arise from a truncation of the Taylor expansion of the plane wave at some finite order. The transition moments are evaluated with this truncation and their magnitude is squared keeping all nonzero terms. The full second-order expression, however, comes from keeping all terms through second-order after the magnitude of the transition moment has been squared. The resulting cross terms make it possible that the oscillator strength can become negative.

$TiCl_4$ has been studied experimentally and theoretically by several different groups and is often used to illustrate the ability of a TDDFT based method to model X-ray excitations.[1,3,29,67,218,219] It's a tetrahedral coordinated system of T_d symmetry, so the five Ti d orbitals are split into two sets of two and three orbitals that transform as the e and t_2 irreducible representations, respectively. The experimental pre-edge peak is a rather broad feature requiring two peaks to fit, which are assigned as excitations to the e and t_2 sets of Ti d orbitals. We will focus on excitations to the e set of orbitals.

There are eight different transitions to the e set of Ti d orbitals that are around ∼2763 eV when calculated at the PBE1PBE/6-31+G(d) level of theory (Tab. 3.6). The first six

Symmetry	Energy (meV)	$10^3 f^{(0)}$	$10^3 f^{(E1+M1+E2)}$	$10^3 f^{(2)}$
T_1	4.474	0.00	5.54	5.54
T_1	4.474	0.00	5.54	5.54
T_1	4.474	0.00	5.54	5.54
T_2	4.482	2.48	3.59	−5.28
T_2	4.482	2.48	3.59	−5.28
T_2	4.482	2.48	3.59	−5.28
E	4.515	0.00	3.32	3.32
E	4.515	0.00	3.32	3.32

Table 3.6. Oscillator strengths for Cl 1s → Ti 3d transitions calculated at the PBE1PBE/6-31+G(d) level of theory. The excitation energies are shifted by −2763 eV.

excitations are dominated by transitions from the t_2 Cl 1s orbitals and the final two are dominated by transitions from the a_1 orbital. The excitations from the t_2 orbitals are further separated into two sets of triply degenerate transitions, one of which is dipole-allowed. These dipole-allowed transitions have negative oscillator strengths when the second-order expression is used. The second-order cross terms include the electric-dipole and either the magnetic quadrupole or the electric octupole. These second-order terms can either be positive or negative depending on the signs of these transition moments and will only be nonzero for dipole-allowed transitions. This means that the only instance where the second-order oscillator strength can be negative is when the E1 transition moment is nonzero. Unfortunately, the addition of the cross-terms between the electric-dipole and the electric octupole and magnetic quadrupole terms provides an origin-independent oscillator strength, but the resulting expression is no longer a perfect square. The origin of negative oscillator strengths for the $f^{(2)}$ expression has also been discussed by other authors.[220,221]

From an experimental point of view, the intrinsic broadening of these excitations is so

large that they cannot be individually resolved, therefore no comparison can be made with the calculated intensities for each transition. However, the fact that the computed oscillator strength is negative may be considered a diagnostic for the need to include even higher-order multipole contributions in the model, since the exact (untruncated) quantity is assured to be positive for absorption processes. In fact, as can be seen from Tab. 3.6, the effect of the second-order terms is of the same order of magnitude as the electric-dipole contribution for the T_2 transition. It should also be pointed out that the TRK sum rule should still be satisfied, therefore the positive contributions from the second-order terms in other transitions will compensate for the negative ones when the sum is performed.

3.2.8 Conclusion

The origin-dependent $f^{(E1+M1+E2)}$ expression is commonly used to describe X-ray absorption spectra when the EDA is expected to breakdown. We have shown that this expression is not guaranteed to satisfy the Thomas-Reiche-Kuhn sum rule and can often result in different spectral shapes dependent up on the origin definition. This is true even in cases where the EDA is still valid as different definitions of the origin can artificially enhance higher-order terms in the oscillator strength expression. Spectra obtained using this expression are not likely to be reliable unless particular care is taken when assigning the molecular origin for each calculated transition. Full treatment of the oscillator strength through second-order removes many of these strange behaviors; the sum rule is satisfied and the spectral lineshape is consistent at all definitions of the origin. However, the $f^{(2)}$ expression can result in negative oscillator strengths for dipole-allowed transitions. This has been observed for several Cl K-edge transitions of $TiCl_4$, but it is not yet clear how common this behavior is. Having negative oscillator strengths would prevent one from making spectral assignments and is a diagnostic for the need to use a higher-order expansion or the untruncated form of the operator. When the transition moment and oscillator strength are treated through infinite-order, these undesirable properties are no longer present. It seems that either the electric-dipole approximation or the infinite-order oscillator strength should be used. Any

other truncation of the plane wave Taylor expansion can lead to strange and unphysical behaviors that can effect the way spectral features are assigned.

Chapter 4

TD-CI USING THE GRAPHICAL UNITARY GROUP APPROACH

Dynamic electric properties are most commonly determined by applying linear and nonlinear-response theory. This is often a sequential process as each order of response depends on the solution for the previous lower-order. Response theory is a perturbative approach and is not directly amenable to modeling time-resolved spectroscopies or experiments involving exotic pulse shapes. Nonperturbative interaction between a system and an electric field can be modeled explicitly in time. This makes it possible to more easily resolve higher-order properties and highly nonlinear processes. Time-dependent configuration interaction (TDCI) has asserted itself as a powerful tool for accurately modeling electronic dynamics. We have implemented TDCI using the Graphical Unitary Group Approach (TD-GUGA-CI) in order to study the dynamics of open-shell systems while retaining spin as a good quantum number. This approach has been used to resolve linear and nonlinear electric properties of molecular systems. Important considerations when modeling dynamic electric properties in the time domain are presented as well as comparisons to properties of broken-symmetry solutions.

4.1 Introduction

Intense atto- and femtosecond laser sources have opened up new ways to probe electronic and nuclear dynamics in real time.[222,223] Intricate experiments take advantage of these new laser sources and tease out previously inaccessible information about different molecular systems.[224,225] A more detailed understanding of linear and nonlinear-responses to these strong electric fields will aid in the interpretation of these complex experiments.

Dynamical polarizabilities and hyperpolarizabilities are often calculated with time-dependent

perturbation theory using sum-over-states expressions.[226] These techniques assume a much weaker field strength than those seen in typical attosecond experiments. Further, they are not able to account for the complicated pulse shapes that are often employed or the time-dependence between pump and probe pulses. An alternative approach would be to model the system explicitly in the time domain under the influence of an external field and extract relevant properties from the simulation. This goes beyond the perturbative regime and captures all orders of response that could be described by perturbation theory all at once. It also allows for the use of pulse shapes and field strengths more representative of the experiment being modeled.

Real-time time-dependent density functional theory (RT-TDDFT) has become the workhorse of time-dependent electronic structure theory due to its low computational cost and reasonable accuracy.[227] It has been used to model absorption spectra of large molecules,[228,229] linear and nonlinear electric properties,[230,231] and spin[232,233] and charge transport.[234,235] However, RT-TDDFT suffers from some well-documented problems associated with using adiabatic functionals of the density. This can lead to a time-dependence in the resonant frequencies as the density is propagated in time.[236–238] This is a particularly vexing problem that makes it difficult to model time-resolved spectroscopies or excited-state properties although some groups have made recent progress in this area.[239,240]

Multiconfigurational wave functions propagated in time do not suffer from the same difficulties of RT-TDDFT. These techniques have been used to model time-resolved photoionization[241,242] and nonlinear-responses[243–247] to intense electric fields. Time-dependent Configuration Interaction Singles (TD-CIS) is the simplest and most commonly used multiconfigurational approach. Unfortunately, it tends to overestimate (hyper)polarizabilities due to a lack of electron correlation in the description of the ground state, although it is able to qualitatively describe high harmonic generation (HHG) spectra.[243,246,247] Madsen and Miyagi recently gave a more detailed analysis of the role of multielectron excitations on the description of nonlinear properties with their series of TD-RASSCF approaches.[248] Their analysis highlighted the importance of including doubly excited configurations in the basis

describing the time-evolving wave function. This work will focus on practical considerations of evaluating nonlinear electric properties in the time domain for both closed- and open-shell systems with GUGA-CI. We will also highlight the importance of including doubly excited configurations in the description of the time-evolving wave function.

4.2 Theory

4.2.1 Configuration Interaction

Configuration Interaction describes electronic wave functions as linear combinations of different electron configurations

$$|\psi\rangle = \sum_i C_i \, |\phi_i\rangle \, . \tag{4.1}$$

CIS uses singly excited configurations from the reference state to describe excited electronic states, but does not improve the description of the reference ground state.[209] The expansion in Equation (4.1) can be truncated at other levels of excitation leading to methods like CISD and CISDT where doubly and triply excited configurations are also included. These approaches can be used to describe multiconfigurational ground and excited electronic states. The bases used in the expansion are usually either excited Slater determinants (SDs)[249–252] or spin-adapted configurations known as Configuration State Functions (CSFs).[253,254]

Excited SDs can be used as the CI basis for any form of the mean-field reference including a restricted, unrestricted, or noncollinear wave function.[255–257] Any relaxation or breaking of a particular symmetry in the reference configuration will also be broken for the resulting CI wave functions. There are some advantages in using a broken-symmetry wave function including most notably that breaking symmetry usually lowers the energy of the variational wave function. However, when a broken-symmetry wave function is used as the reference configuration for response theory of CI, there can often be unphysical bright transitions to different spin states.[258] These unphysical transitions should usually be removed from calculated spectra and should influence calculated electric properties as well.

Configuration state functions are spin-adapted combinations of determinants that can also be used as the basis in the CI expansion. They do require the use of a restricted reference configuration that is both an eigenfunction of $\hat{S}_z$ and $\hat{S}^2$. CSFs are an appealing alternative to SDs since the Full CI space will be smaller due to the lack of coupling between different spin states and the Hamiltonian being block-diagonalized into different spin states. For higher-spin states, CIS on top of an ROHF wave function will add a small amount of electron correlation to the description of the ground state.[259] This is of course different from what is seen when only singly excited SDs are used or when the reference configuration is a singlet. The combination of SDs needed to create the excited high-spin CSFs may include doubly excited determinants which would offer a small correction to the description of the ground state.

The time-independent nonrelativistic electronic Hamiltonian is defined as

$$\hat{H}_0 = \sum_{ij} \langle i| \hat{h} |j\rangle \hat{E}_{ij} + \frac{1}{2} \sum_{ijkl} (ij|kl)(\hat{E}_{ij}\hat{E}_{kl} - \delta_{jk}\hat{E}_{il}) \tag{4.2}$$

where $\{i, j, k, l\}$ are orbital indices, $\langle i| \hat{h} |j\rangle$ and $(ij|kl)$ are one- and two-electron integrals respectively, and $\hat{E}_{ij}$ is a spin adapted excitation operator

$$\hat{E}_{ij} = \sum_{\sigma} \hat{a}^{\dagger}_{i\sigma}\hat{a}_{j\sigma}. \tag{4.3}$$

The one- and two-body coupling coefficients between states must be calculated when constructing the CI matrix: $\langle \psi'| \hat{E}_{ij} |\psi\rangle$ and $\langle \psi'| \hat{E}_{ij}\hat{E}_{kl} - \delta_{jk}\hat{E}_{il} |\psi\rangle$. These are simple to calculate when using orthogonal orbitals and determinants since they can only be 0 or ± 1. CSFs are not orthogonal, however, and these coupling coefficients cannot be calculated so simply.

The graphical unitary group approach (GUGA)[253,260–264] determines these coupling coefficients by finding patterns in a graph constructed from available spin couplings within different orbital occupations. The graph is a convenient representation of a distinct row table, which contains all unique rows of the Paldus arrays that define different spin-adapted configurations. Each path that traverses the graph is a unique CSF and the coupling coefficients are determined by the shape made by two different CSFs. This graph can be efficiently

searched to build the Hamiltonian or, in the case of direct CI, the matrix-vector product

$$\sigma_i = \sum_j H_{ij} C_j \tag{4.4}$$

where H_{ij} are elements of $\hat{H}_0$. This technique can also be applied to multiconfigurational SCF (MCSCF) or any CI excitation level simply by changing the graph that is searched. Further details on the implementation of GUGA-CI can be found in Appendix A.

4.2.2 Time-dependent CI

The dynamics of a time-evolving wave function are determined by solving the time-dependent Schrödinger equation

$$\mathrm{i}\frac{\partial \Psi(t)}{\partial t} = \hat{H}(t)\Psi(t). \tag{4.5}$$

The time-dependent Hamiltonian is defined as

$$\hat{H}(t) = \hat{H}_0 - \hat{\boldsymbol{\mu}} \cdot \mathbf{E}(t) \tag{4.6}$$

where the field-free Hamiltonian is augmented by the dipole operator $\hat{\boldsymbol{\mu}} = -\sum_i^N \mathbf{r}_i + \sum_A^{N_A} Z_A \mathbf{R}_A$ coupling to an external electric field $\mathbf{E}(t)$.

The time-dependent wave function is described in the basis of CI states

$$\Psi(t) = \sum_i C_i(t)\psi_i. \tag{4.7}$$

The initial wave function at $t = 0$ can be any of the CI states or a superposition of several states. Without an external electric field, the propagation of the time-evolving coefficients is trivial

$$\mathbf{C}(t + \Delta t) = e^{-\mathrm{i}\hat{\mathbf{H}}_\mathbf{0}\Delta t}\mathbf{C}(t) \tag{4.8}$$

where $\hat{\mathbf{H}}_\mathbf{0}$ is the diagonal field-free Hamiltonian in the CI basis. This just causes the wave function to rotate through the complex plane, but does not change any observables if beginning in an eigenstate of $\hat{H}_0$. The split operator approach[265] can be used to separate the

time-dependent and -independent parts of the Hamiltonian and describe the system under the influence of an oscillating electric field

$$\mathbf{C}(t+\Delta t) = \left[\prod_{q=x,y,z} \mathbf{U}_q^{\dagger} e^{\mathrm{i}E_q(t)\boldsymbol{\mu}_q \Delta t} \mathbf{U}_q\right] e^{-\mathrm{i}\hat{\mathbf{H}}_\mathbf{0}\Delta t}\mathbf{C}(t) \tag{4.9}$$

where $\mathbf{U}_q$ is a unitary matrix that transforms the CI dipole matrix $\boldsymbol{\mu}_q$ so that it is diagonal. With this formalism, the dynamics of a time-dependent wave function can be determined in the basis of resolved CI states.

4.2.3 Dynamic (hyper)polarizabilities

In these simulations, the field is turned on adiabatically using a linear ramp envelope that grows to a maximum intensity over several optical cycles of the applied field (oc = $\frac{2\pi}{\omega}$). This type of time-dependent electric field can be written as

$$\mathbf{E}(t) = \begin{cases} \frac{t}{x\,\mathrm{oc}}\mathbf{A}\cos(\omega t) & \text{if } 0 \leq t < x\,\mathrm{oc} \\ \mathbf{A}\cos(\omega t) & \text{if } t \geq x\,\mathrm{oc} \end{cases} \tag{4.10}$$

where $\mathbf{A}$ is the constant magnitude vector of the field and x is the number of optical cycles over which the field is turned on. The dynamic polarizabilities and hyperpolarizabilities are determined using a method previously developed in our group.[231] This approach uses several simulations with maximum field strengths of $\pm A$, $\pm 2A$, and $\pm 3A$ to determine first, second, and third-order electric properties. The time-dependent dipole moments of the system under these field strengths are combined and a function is then fit to the data.

To review how this approach works, we must first notice that the time-evolving dipole moment can be expanded in a Taylor series to all orders of response.[266] Each order can be grouped into its own expression that can be used to extract properties from the time-evolving dipole moment with a small error related to the field strengths used, $\mathcal{O}(A^4)$. The

first-, second-, and third-order responses are determined as

$$\mu_{ij}^{(1)} = \frac{8[\mu_i(t, A_j) - \mu_i(t, -A_j)] - [\mu_i(t, 2A_j) - \mu_i(t, -2A_j)]}{12A_j} \tag{4.11}$$

$$\mu_{ijj}^{(2)} = \frac{16[\mu_i(t, A_j) + \mu_i(t, -A_j)] - [\mu_i(t, 2A_j) + \mu_i(t, -2A_j)] - 30\mu_i^0}{24A_j^2} \tag{4.12}$$

$$\mu_{ijjj}^{(3)} = \frac{-13[\mu_i(t, A_j) - \mu_i(t, -A_j)] + 8[\mu_i(t, 2A_j) - \mu_i(t, -2A_j)] - [\mu_i(t, 3A_j) - \mu_i(t, -3A_j)]}{48A_j^3} \tag{4.13}$$

where $\mu_i(t, \pm A_j)$ are the ith components of the time-dependent dipole induced by a field with maximum intensity $\pm A_j$. The polarizability and hyperpolzarizability values are then extracted by fitting different functions to the simulation data

$$\mu_{ij}^{(1)} = \alpha_{ij}(-\omega; \omega)\cos(\omega t) \tag{4.14}$$

$$\mu_{ijk}^{(2)} = \frac{1}{4}[\beta_{ijk}(-2\omega; \omega, \omega)\cos(2\omega t) + \beta_{ijk}(0; \omega, -\omega)] \tag{4.15}$$

$$\mu_{ijkl}^{(3)} = \frac{1}{24}[\gamma_{ijkl}(-3\omega; \omega, \omega, \omega)\cos(3\omega t) + 3\bar{\gamma}_{ijkl}(-\omega; \omega, \omega, -\omega)\cos(\omega t)] \tag{4.16}$$

The frequency-dependent polarizability $\alpha_{ij}(-\omega; \omega)$ is related to the linear refractive index. The first hyperpolarizabilities $\beta_{ijk}(-2\omega; \omega, \omega)$ and $\beta_{ijk}(0; \omega, -\omega)$ correspond to second-harmonic generation (SHG) and optical rectification (OR) respectively. The second hyperpolarizabilities $\gamma_{ijkl}(-3\omega; \omega, \omega, \omega)$ and $\bar{\gamma}_{ijkl}(-\omega; \omega, \omega, -\omega)$ related to third-harmonic generation (THG) and averaged degenerate four-wave mixing (DFWM). Data from the simulation after the external field has reached its maximum are fit to Eqs. (4.14) to (4.16) to extract these properties. Field strengths were kept sufficiently weak so that ionization would not need to be considered and the Keldysh parameters were close to one for all simulations.[267] The fields used for H_2 and water were chosen to compare with experimental data. The off-resonant field for BeH is representative of a Ti:Sapphire laser having a maximum intensity of 800 nm. All simulations used a time step of 0.1 au (0.00242 fs). All CI calculations were performed in a development version of Gaussian[35] and all properties from response theory were obtained using the Dalton16 package.[268,269]

4.3 Results

We begin by calculating the dynamic polarizabilities and hyperpolarizabilities of H_2 at the experimental bond length of 0.7414 Å[270] using TD-CIS and TD-CISD with the 6-31G basis set. This results in 4 configurations for CIS and 10 configurations for CISD, so all configurations can easily be included in the description of the time-evolving wave function. The molecule is oriented along the z-axis and we study the response of the system to 632.8 nm light propagating along the molecular axis. All even-order properties are zero because molecular hydrogen has an inversion center, so only the odd-order molecular properties are presented.

In these calculations, a monochromatic field is linearly ramped to a maximum intensity over several optical cycles. The field must be turned on slowly so that it remains an adiabatic perturbation to the system. If the field is turned on too quickly the system will be perturbed too far from the ground state, preparing a superposition of the ground and excited-states. The time-evolving dipole would then report on how all states in the superposition respond to the field and not just the ground state. This can certainly be problematic when trying to determine the properties of a the ground state or any other single eigenstate.

	1 oc		2 oc		5 oc	
$\alpha_{zz}(-\omega;\omega)$	7.407	(0.999)	7.405	(0.999)	7.407	(0.999)
$\gamma_{zzzz}(-3\omega;\omega,\omega,\omega)$	−506.404	(0.783)	−515.418	(0.850)	−514.369	(0.992)
$\bar{\gamma}_{zzzz}(-\omega;\omega,\omega,-\omega)$	−454.117		−457.244		−457.202	

Table 4.1. TD-CIS polarizabilities and 2nd hyperpolarizabilities of H_2 under the influence of 632.8 nm light with the field turned on at different rates. R^2 values for fits are included in parentheses.

We have compared the (hyper)polarizabilities extracted from simulations where the electric field is turned on over different periods of time. The field is ramped up to its maximum intensity over 1, 2, or 5 optical cycles and the electric properties are extracted from 4 ad-

ditional optical cycles of propagation. The extracted properties are largely unaffected by how quickly the field is turned on (Table 4.1). This is likely because even if the field is turned on quickly and some excited-states are fractionally populated, the superposition is still dominated by the ground state. In that case the majority of the signal would still come from the response of the ground state wave function to the field.

The quality of the fits to the 2nd hyperpolarizabilities signals are significantly improved by turning on the field more slowly. This is due to a large amount of noise that grows in quickly over several optical cycles (Figure 4.1). This likely arises from stimulated transitions among excited-states populated by turning on the field too quickly. These data suggests that turning on the field over 5 optical cycles is a sufficient length of time to achieve an adiabatic perturbation and will be used for all subsequent simulations.

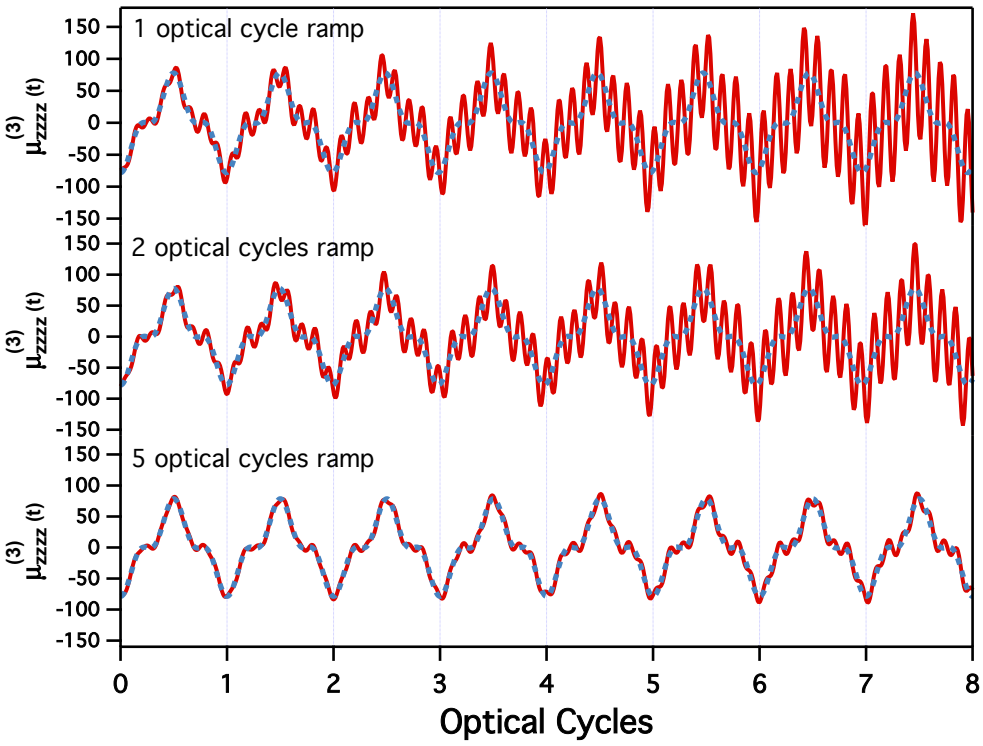

Figure 4.1. The quality of the 2nd hyperpolarizability fits for H_2 if the field is turned on over different lengths of time.

All properties extracted from the real-time simulations are in good agreement with those calculated from response theory. Deviations are partly due to the fact that the field is not truly monochromatic while the field is ramping towards its maximum intensity. Slight numerical noise over the course of the simulation is also a likely culprit. The fits to the simulation data are also very good with R^2 always above 0.99 (Figure 4.2). The polarizability and second hyperpolarizability values are extracted from the fits and are presented in Table 4.2.

	Resp. (HF)	Resp. (CIS)	TD-CIS	Resp. (CISD)	TD-CISD	Exp.[271]
$\alpha_{zz}(-\omega;\omega)$	6.614	7.630	7.407	6.193	6.015	6.9395
$\gamma_{zzzz}(-3\omega;\omega,\omega,\omega)$	−134.107		−514.369	−57.065	−63.201	
$\bar{\gamma}_{zzzz}(-\omega;\omega,\omega,-\omega)$	−118.138		−457.202	−50.609	−69.062	

Table 4.2. Dynamic (hyper)polarizabilities of H_2 with a wavelength of 632.8 nm modeled using various methods and the 6-31G basis set.

The TD-CIS properties are consistently larger in magnitude than those calculated with response theory from a HF reference or with CISD (FCI for this system). A previous study by Saalfrank and coworkers also noted the tendency of TD-CIS to overestimate polarizabilities when compared with TD-CISD.[243] This behavior comes from two factors: the first excitation energy is lower for CIS than for CISD and the transition moments from the ground state are larger for CIS. The same laser pulse thus perturbs the ground state further from equilibrium and induces a larger dipole moment. This behavior can also be rationalized by observing the relative changes in energy and populations of the ground and first excited-state over the course of the simulations (Figure 4.3). The change in energy and projection onto the first excited-state are much greater for CIS than for CISD.

For most systems larger than H_2 it may not be affordable to use the entire CI space as the basis describing the time-evolving wave function. We have investigated how different properties change as the number of CI states increases for a water molecule. The experimental geometry of gaseous water was used with $R_{O\text{-}H} = 0.957$ Å and $\alpha_{HOH} = 104.474°$.[272] For these

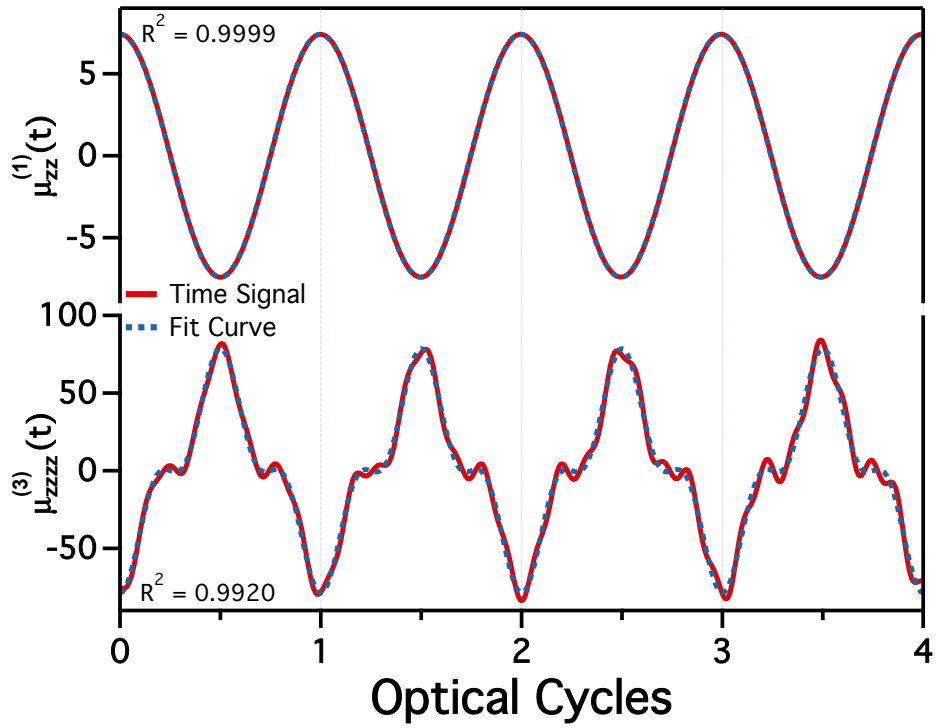

Figure 4.2. Time evolution of the first- and third-order responses of H_2 modeled with TD-CIS using the 6-31G basis set. The fit curves and their R^2 values overlay the simulation data.

simulations, the system is oriented in the xy-plane with the molecular dipole along the z-axis.

In most published TD-CI studies an adequate basis for the time-evolving wave function is identified by adding in higher energy states until the time-evolving dipole moment has converged to a reasonable degree.[246] Figure 4.4 shows that the majority of the electric properties converge smoothly toward the result that would be obtained using the full CIS space. However, the third-order properties along the static dipole axis ($\gamma_{zzzz}(-3\omega;\omega,\omega,\omega)$ and $\bar{\gamma}_{zzzz}(-\omega;\omega,\omega,-\omega)$) do not converge as smoothly as the lower-order properties. It seems that as much as 2/3 of the total space may be required to converge the linear and nonlinear properties to within 5% of what would be calculated using the total CI space, consistent

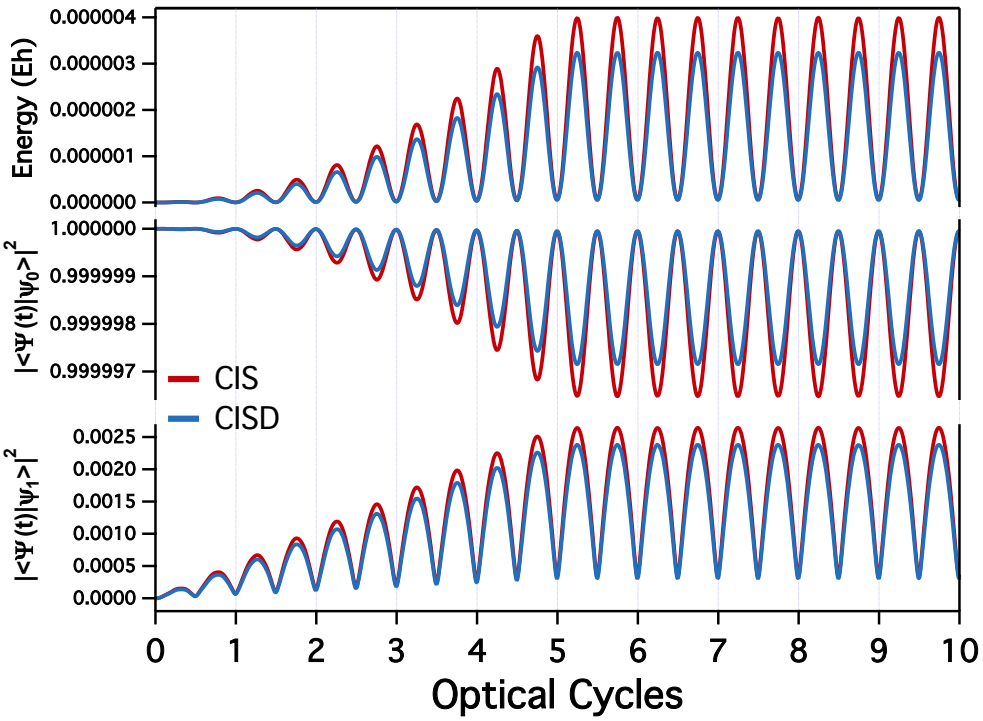

Figure 4.3. Change in energy of the time-dependent H_2 wave function relative to the ground state energy and its projection onto the ground and first excited-state modeled with CIS and CISD. The incident 631.8 nm pulse increases to a maximum intensity of 0.001 a.u. over 5 optical cycles.

with what other studies have shown.[246] At that point all of the valence transitions have been included and only the oxygen K-edge transitions are remaining, which are energetically well-separated from other transitions and contribute very little in the determination of these properties. It may be advantageous for future HHG studies to also evaluate the convergence of higher-order properties as well as that of the first-order polarizability when determining the basis for the time-evolving wave function. The vast majority of valence transitions may be required.

For the water molecule, the first-order properties calculated with TD-CIS are again consistently larger in magnitude than those calculated with TD-CISD. Unfortunately, both

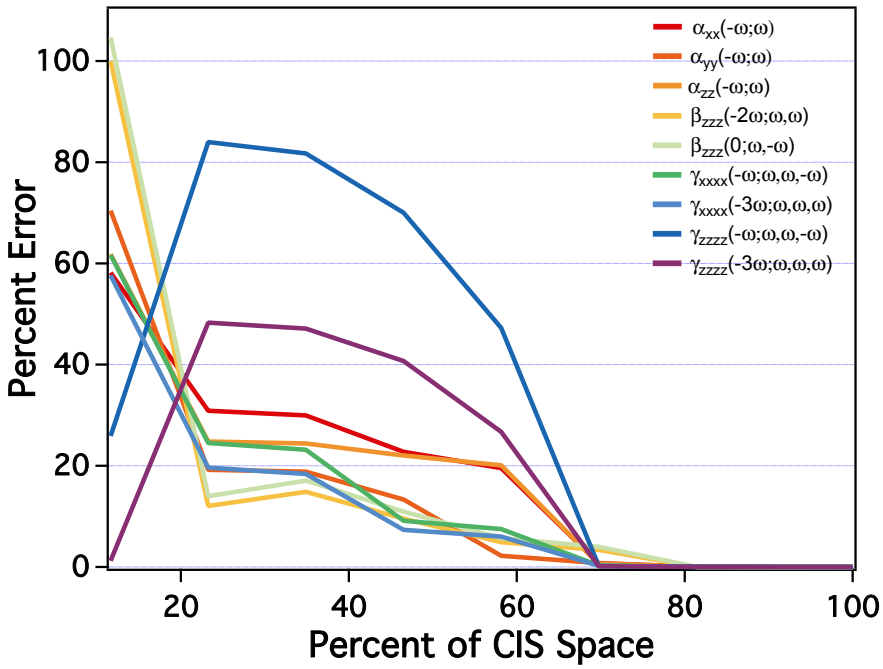

Figure 4.4. Convergence of various properties of water as the number of CIS states is increased until it spans the full space.

methods and linear-response HF underestimate the experimental polarizabilities although TD-CIS is closer. The deviation from experiment is due to several factors, most notably the limited basis set used in these simulations. The CISD excitation energies for water are known to be too large compared to experimental values leading to the diminished response seen at all orders.[243]

An important benefit of the GUGA-CI approach is that it restricts the system to have a particular spin symmetry. This is in contrast to CI on top of an Unrestricted Hartree Fock (UHF) wave function in which all CI states will have broken $\hat{S}^2$ symmetry, just like the reference configuration. We will illustrate show that breaking spin symmetry and mixing with higher-spin states influences the determination of dynamic electric properties. The TD-UCIS results take parameters from unrestricted CIS calculations in Gaussian and the

	Resp. (HF)	Resp. (CIS)	TD-CIS	Resp. (CISD)	TD-CISD	Exp.[273]
$\alpha_{xx}(-\omega;\omega)$	5.245	5.587	5.578	4.899	4.892	9.546
$\alpha_{yy}(-\omega;\omega)$	7.249	8.133	8.123	6.150	6.143	10.314
$\alpha_{zz}(-\omega;\omega)$	5.837	6.419	6.411	5.039	5.031	9.906
$\beta_{zzz}(-2\omega;\omega,\omega)$	−5.694	−12.461	−12.371	−2.563	−2.566	
$\beta_{zzz}(0;\omega,-\omega)$	−4.495	−10.434	−10.346	−2.077	−2.071	
$\gamma_{xxxx}(-3\omega;\omega,\omega,\omega)$	1901.647		1851.873		1078.802	
$\bar{\gamma}_{xxxx}(-\omega;\omega,\omega,-\omega)$	1032.180		1016.642		722.862	
$\gamma_{zzzz}(-3\omega;\omega,\omega,\omega)$	455.240		350.143		260.333	
$\bar{\gamma}_{zzzz}(-\omega;\omega,\omega,-\omega)$	278.554		159.873		189.269	

Table 4.3. Dynamic (hyper)polarizabilities of water with a wavelength of 514.5 nm modeled using various methods and the 6-31+G* basis set.

necessary state and transition dipoles were evaluated using unrelaxed CI densities. We will investigate the linear and nonlinear properties of the paramagnetic BeH molecule, a typically example with a spin-contaminated ground state wave function (Table 4.4).[258] The molecule is fixed at its experimental geometry of 1.3426 Å.[274]

	Resp. (ROHF)	TD-UCIS	TD-GUGA-CIS	TD-GUGA-CISD
$\alpha_{xx}(-\omega;\omega)$	36.359	37.834	38.720	28.633
$\alpha_{zz}(-\omega;\omega)$	20.566	20.758	20.732	20.307
$\beta_{zzz}(-2\omega;\omega,\omega)$	−221.381	−193.605	−211.705	−205.635
$\beta_{zzz}(0;\omega,-\omega)$	−151.097	−132.211	−143.883	−153.281
$\gamma_{zzzz}(-3\omega;\omega,\omega,\omega)$		41 148.193	47 154.336	38 425.598
$\bar{\gamma}_{zzzz}(-\omega;\omega,\omega,-\omega)$		10 735.933	13 278.785	31 112.808

Table 4.4. Dynamic (hyper)polarizabilities of BeH with a wavelength of 800 nm modeled using various methods and the 6-31+G* basis set.

The first-order properties are virtually identical for TD-UCIS and TD-GUGA-CIS, but both methods significantly overestimate the polarizabilities compared to the TD-GUGA-CISD method. The calculated first hyperpolarizabilities are also similar between both single excitation methods and are comparable to the CISD results. The third-order properties do start to deviate significantly between all time-dependent methods, particularly for $\bar{\gamma}_{zzzz}(-\omega;\omega,\omega,-\omega)$. The TD-GUGA-CISD results are about three times greater than the singly excited methods. Part of the difference between the UCIS and GUGA-CIS approaches is explained by the different reference states. The rest is due to the different eigenspectra for the approaches. Many of the excited-states determined by the UCIS approach mix with neighboring quartet states and shift to different energies. Of course, this does not happen with the GUGA-CI approach and all states are true doublets.

4.4 Conclusions

Linear and nonlinear electric properties can be extracted from time-dependent configuration interaction calculations by fitting equations to the time signal. This approach is nonperturbative and has the potential to go beyond what is possible with traditional response theory since high order properties can be determined all at once without needing to sequentially solve each response problem. The time over which an electric field is turned on was shown to have a significant impact on the quality of the fit. Although the extracted properties did vary much for H_2, this is not likely to be the case for more complicated systems. The quality of the CI space used to describe the time-evolving wave function should also be considered. The vast majority of valence excitations may be necessary to adequately converge linear and nonlinear properties. The TD-GUGA-CI approach forces open-shell systems to remain spin eigenfunctions. Results for the broken-symmetry TD-UCIS method deviate from the GUGA-CI properties mostly due to changes in the eigenspectrum as states mix with other higher-spin states. In short, TD-GUGA-CI is a powerful tool for modeling linear and nonlinear electric properties and has the potential to model more complex time-resolved spectra in the future.

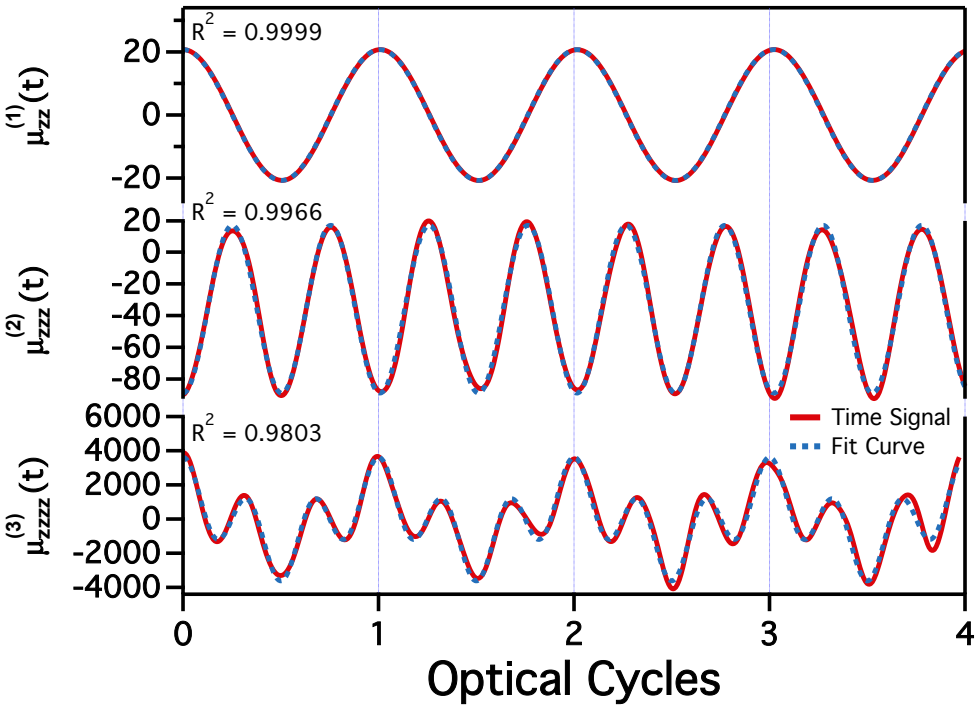

Figure 4.5. Time evolution of the first-, second-, and third-order responses of BeH modeled with TD-GUGA-CIS using the 6-31+G* basis set. The fit curves and their R^2 values overlay the simulation data.

Chapter 5

AN EFFICIENT IMPLEMENTATION OF SPIN-PROJECTED GENERALIZED HARTREE-FOCK THEORY

Projected Hartree-Fock (PHF) theory can restore important symmetries to broken-symmetry wave functions. Variation after projection (VAP) implementations make it possible to deliberatively break and then restore a given symmetry by directly minimizing the projected energy expression. This technique can be applied to any symmetry that can be broken from relaxing constraints on single Slater determinant wave functions. Generalized Hartree-Fock (GHF) wave functions are neither eigenfunctions of $\hat{S}_z$ or S^2. By relaxing these constraints, the wave function can explore a larger variational space and can reach lower energies than more constrained HF solutions. We have implemented spin-projected GHF (SGHF), which retains many of the advantages of breaking symmetry while also being a spin eigenfunction, with some notable improvements over previous implementations. The overall structure of the algorithm better constrains memory usage and forms new intermediate matrices. Discretization of the necessary integration over the rotation group $SO(3)$ is accomplished much more efficiently using Lebedev grids. A novel scheme to incrementally build rotated Fock matrices is also presented and compared with more standard approaches.

5.1 Introduction

Strongly correlated systems present a unique challenge for electronic structure theory. These systems typically have degenerate or nearly degenerate orbitals which cause the single determinant description of the wave function to break down leading to spontaneous symmetry breaking due to instabilities. While this symmetry breaking will lower the variational energy closer to the exact value, the approximate solution will not have the same symmetries as the

true solution. On the other hand, if a solution is constrained to have the desired symmetries of the exact solution this will raise the solution's energy and can lead to qualitatively incorrect descriptions of the system. Löwdin referred to this as the "symmetry dilemma" where one must make a choice on whether to enforce a particular symmetry or to find a lower energy broken-symmetry solution.[275]

This dilemma has motivated the development of various projection techniques to approximately or exactly restore certain symmetries of broken-symmetry wave functions. In this way the energy is lowered by symmetry breaking and lowered again by restoring the desired symmetry. The approximate wave function and its properties are also made more similar to the true solution. The simplest scheme is to apply a projection operator after converging to a stable broken-symmetry solution, referred to as projection after variation (PAV). This projected wave function is not variationally optimized making the evaluation of properties and derivatives quite complicated.[276–278] PAV also has difficulties near regions of spontaneous symmetry breaking, which can lead to discontinuities in the potential energy surface (PES). Further, most implementations only approximately restore spin symmetry, so there will still be contaminating states.[279] These problems can be addressed by variationally optimizing the wave function in the presence of the projection operator, known as variation after projection (VAP).

The problems with PAV approaches led to the development of the Extended Hartree-Fock (EHF) method.[280,281] This is a VAP approach that uses Löwdin's spin projection operator to remove components of the wave function not having the desired spin symmetry. While this method was successful in many respects, Löwdin's projection operator led to exceedingly complicated SCF equations and was all but abandoned. Simpler operators the restore spin symmetry have since been developed, renewing interest in this body of work. Scuseria and coworkers revitalized VAP techniques in the quantum chemistry community by applying them to the Hartree-Fock-Bogoliubov (HFB) and HF wavefunctions.[282,283] They broke and restored not only spin symmetry, but also complex conjugation, point group, and particle number in the case of HFB wave functions. These contributions built off of a larger body

of work on symmetry projection in the nuclear physics community.[284–286] These projected Hartree-Fock (PHF) wave functions retain the advantages of broken-symmetry wave functions, namely the larger variational space, and also have the same symmetries as the exact solution. In other words, they provide a solution to the "symmetry dilemma".

The PHF method accounts for the majority of static correlation, but there is still a significant portion of dynamic correlation that is unaccounted for. This motivated the development of many techniques to add dynamic correlation in much the same way as ordinary HF. Scuseria and coworkers have worked to combine symmetry projection with DFT while attempting to avoid double counting of electron correlation[287] and have reformulated the spin-projected HF wave function in terms of a polynomial similarity transformation to form a spin-projected coupled cluster theory.[288,289] Other groups have also combined spin-projected HF with many-body perturbation theory[290] and configuration interaction.[291,292]

The majority of the recent extensions of Scuseria's original work on PHF have focused on spin-projected unrestricted HF (SUHF). Our work revisits spin-projected GHF (SGHF) and provides ways to more efficiently construct the PHF effective Fock matrix. First, we present an algorithm that is more easily parallelized and allows better control over memory usage. We also advocate using a Lebedev integration grid when discretizing the integration over rotation angles and discuss issues with convergence associated with sparse grids. Finally, we present a novel scheme to incrementally build all necessary rotated Fock matrices. These modifications have greatly reduced the cost of optimizing SGHF wave functions and will make it possible to study larger molecular systems with this method. Some of these techniques can also be used with projected UHF and with other types of projection operators.

5.2 Theory

Projected Hartree-Fock theory (PHF) describes the electronic wave function in terms of a transfer operator (or a sum of transfer operators) acting on a broken-symmetry wave

function[293,294]

$$\left|\Psi_m^S\right\rangle = \hat{P}\left|\Phi\right\rangle = \sum_k f_k \hat{P}_{mk}^S \left|\Phi\right\rangle . \tag{5.1}$$

where $\left|\Psi_m^S\right\rangle$ is a wave function with quantum numbers S and m. The coefficients f_k are determined by diagonalizing the Hamiltonian in the basis of the transfer operators. The transfer operators are defined as linear combinations of group operators $\hat{A}$ weighted by elements of the matrix associated with that operator in a particular irreducible representation

$$\hat{P}_{mk}^S = \frac{l_S}{h} \sum_{A \in G} \Gamma^S(A)_{mk}^* \hat{A} \tag{5.2}$$

The normalization factor l_S and h are the dimension of the irreducible representation Γ^S and the order of the group respectively. These operators are meant to restore a particular symmetry such as spin, particle number, complex conjugation, or point group. The action of operator $\hat{P}_{mk}^S$ produces a wave function that transforms as the mth row of irreducible representation Γ^S, thus having m and S as good quantum numbers. While these are not truly projection operators, they do achieve the goal of preparing a wave function with the desired quantum numbers.

The projected wave function is determined by minimizing the projected energy expression

$$E = \frac{\left\langle\Phi\right| \hat{H}\hat{P} \left|\Phi\right\rangle}{\left\langle\Phi\right| \hat{P} \left|\Phi\right\rangle} \tag{5.3}$$

where we have used the fact that $\hat{P}$ commutes with the Hamiltonian and that it is idempotent. The specific form of $\hat{P}$ and the representation of the broken-symmetry wave function will dictate how to minimize this function.

5.2.1 Spin-projection Operators

Spin symmetry can be restored by forcing the projected wave function to be invariant to the axis of spin quantitation.[295] The operator that accomplishes this is expressed as

$$\begin{aligned}\hat{P}^S_{mk} &= |S;m\rangle \langle S;k| \\ &= \frac{2S+1}{8\pi^2}\int_0^{2\pi}\int_0^{\pi}\int_0^{2\pi} d\alpha\, d\beta\, d\gamma \sin(\beta) D^{S*}_{mk}(\alpha,\beta,\gamma) e^{i\alpha\hat{S}_z} e^{i\beta\hat{S}_y} e^{i\gamma\hat{S}_z}\end{aligned} \tag{5.4}$$

where $D^S_{mk}(\alpha,\beta,\gamma)$ is a Wigner rotation matrix element.[296,297] The label S indicates the total spin of the projected wave function and m and k are different spin projections along the z-axis. This operator involves an integration over the rotation group $SO(3)$ and we will discuss how to efficiently discretize this integration in later sections.

This operator can be simplified for UHF wave functions as these retain $\hat{S}_z$ symmetry. This makes rotation about the z-axis trivial, so the above operator can be simplified to

$$\begin{aligned}\hat{P}^S_{mm} &= |S;m\rangle \langle S;m| \\ &= \frac{2S+1}{2}\int_0^{\pi} d\beta \sin(\beta) d^S_{mm}(\beta) e^{i\beta\hat{S}_y}\end{aligned} \tag{5.5}$$

where $d^s_{mm}(\beta)$ is an element of the Wigner small d-matrix.[296] In this case, it is a true projection operator. This work will focus exclusively on spin-projection as it has special significance in the context of chemical problems, but much of the later discussion is also applicable to the restoration of other symmetries as we will point out where appropriate.

5.2.2 Spin-projected Hartree-Fock

The PHF energy for a particular spin symmetry is expressed as

$$E^S = \sum_{mk}^{2S+1} f^*_m H_{mk} f_k \tag{5.6}$$

where the Hamiltonian matrix elements are

$$H_{mk} = \langle\Phi|\, \hat{H}\hat{P}^S_{mk}\, |\Phi\rangle \tag{5.7}$$

and this matrix is the dimension of the number of different spin projections $(2S+1)$. The energy expression is a function of the broken-symmetry density $\boldsymbol{\rho}$ defined in terms of the broken-symmetry molecular orbital coefficients

$$\rho_{\mu\nu} = \sum_{i}^{N_{occ}} C_{\mu i} C_{\nu i}^{*} \tag{5.8}$$

and the linear coefficients $\mathbf{f}$ defining the expansion of the projected wave function in terms of transfer operators. The stationary conditions for the variational problem are determined from the variation in a Lagrangian under the constraints that the broken-symmetry density remains idempotent and that the projected wave function is normalized

$$\mathcal{L}^{S}[\mathbf{f}, \boldsymbol{\rho}] = \sum_{mk} f_{m}^{*} H_{mk} f_{k} - \mathrm{Tr}\left[\boldsymbol{\Lambda}(\boldsymbol{\rho}^{2} - \boldsymbol{\rho})\right] - E^{S}\left(\sum_{mk} f_{m}^{*} S_{mk} f_{k} - \mathbf{1}\right) \tag{5.9}$$

where we have introduced the projected overlap matrix elements

$$S_{mk} = \langle \Phi | \, \hat{P}_{mk}^{S} \, | \Phi \rangle \, . \tag{5.10}$$

The stationary conditions resulting from variation of this Lagrangian with respect to the linear coefficients leads to the generalized eigenvalue problem

$$\mathbf{H}\mathbf{f} = \mathbf{S}\mathbf{f}E^{S}. \tag{5.11}$$

This is a small configuration interaction (CI) problem in the basis of different spin projections along the z-axis. The linear coefficients and the energy of the system are obtained by solving this problem. Variation of the Lagrangian with respect to the broken-symmetry density leads to a familiar stationary condition

$$[\boldsymbol{\mathcal{F}}, \boldsymbol{\rho}] = \mathbf{0} \tag{5.12}$$

where $\boldsymbol{\mathcal{F}}$ is not the standard Fock matrix but an effective Fock matrix. This matrix is defined as

$$\boldsymbol{\mathcal{F}} = \sum_{mk} f_{m}^{*} f_{k} \int dg \, w_{mk}(g) (\boldsymbol{\mathcal{F}}_{g} - E^{S} \mathbf{X}_{g}). \tag{5.13}$$

where $w_{mk}(g)$ is a weight at a rotation angle, $\boldsymbol{\mathcal{F}}_g$ is a matrix defined at a given rotation angle, and $\mathbf{X}_g$ is related to the derivative of the overlap matrix $\mathbf{S}$. Explicit expressions for these terms can be found in the Appendix B, but are left out of this section for brevity. The above stationary conditions can be satisfied by solving the PHF self-consistent field (SCF) equation

$$\boldsymbol{\mathcal{F}}\mathbf{C} = \mathbf{C}\boldsymbol{\epsilon} \tag{5.14}$$

much the same way as with ordinary HF, but while also solving Equation (5.11) to obtain the linear coefficients every SCF iteration.

5.3 Computational Details

Spin-projected generalized Hartree-Fock has been implemented in the Chronus Quantum software package.[298] This implementation forms new intermediates and limits memory usage in ways not discussed in previous works. It also takes a novel approach to incrementally forming Fock matrices.

The effective Fock matrix is a function of the linear coefficients $\mathbf{f}$, the energy E^S, and involves an integration over the rotation angles g (Equation (5.13)). The Hamiltonian $\mathbf{H}$ and overlap matrix $\mathbf{S}$ are also formed by integrating over the rotation angles and are used to determine the linear coefficients and energy, so the effective Fock matrix cannot be completely formed until Equation (5.11) is solved during each SCF iteration.

Previous implementations formed the Hamiltonian, diagonalized it, and then began the process of forming the effective Fock matrix. Code structured in this way requires many intermediate quantities used to form the Hamiltonian, overlap matrix, and effective Fock matrices to be stored in memory. These include all the rotated density matrices and rotated Fock matrices at each point in the integration over g (see Appendix B for explicit expressions). This structure also required multiple loops over the integration grid. We can remove the need to store these intermediate quantities and only loop over the integration grid once every SCF

cycle by forming new intermediate matrices

$$\mathfrak{F}_{mk} = \int dg\, w_{mk}(g) \boldsymbol{\mathcal{F}}_g \tag{5.15}$$

$$\mathfrak{X}_{mk} = \int dg\, w_{mk}(g) \mathbf{X}_g \tag{5.16}$$

The number of intermediate matrices scales with the size of the CI problem, so there will only be $(2S+1)(2S+2)/2$ matrices or the dimension of the lower triangle of the Hamiltonian. After this integration, we can solve Equation (5.11) to determine the linear coefficients and then contract them with these intermediate matrices to complete the formation of the effective Fock matrix. The general structure of this algorithm is presented in Figure 5.1.

```
Build integration grid and determine grid weights
while SCF not converged do
    Transform the broken-symmetry density to the NO basis
    for g = 0 to N_grid do
        Form X_g, and F_g
        for m, k = 0 to 2S + 1 do
            Add contributions to S_mk, H_mk, 𝔛_mk, and 𝔉_mk
        end
    end
    Solve the CI Problem
    Contract 𝔛_mk and 𝔉_mk with the CI vector
    Diagonalize F and evaluate convergence
end
```

Figure 5.1. Schematic of the algorithm for spin-projected GHF.

This scheme is advantageous for several reasons. For one, this structure makes it easier to limit memory usage in the case where all rotated densities, overlap matrices, and rotated

Fock matrices can't be stored in memory at one time. Although this is an unlikely scenario on most modern machines. Another advantage is that all integration points are independent, so the loop over g can easily be split over several cores and the collected quantities formed after each core has completed its task. This is advantageous over the previous implementation, which required multiple loops over g, since parallel processes would need to be spawned and reformed each SCF cycle, an undesirable trait in a parallel algorithm. This scheme is useful not just for spin projection, but for any form of projected HF.

Spin projection operators involve an integration over the rotation group $SO(3)$, which must be discretized in some way. Previous implementations of SGHF advocated using a Trapezoid grid for integration over α and γ and a Gauss-Legendre grid for integration over β.[282] These choices result in very dense integration grids since about 10 points for each angle are usually necessary to adequately restore spin symmetry. At each integration point, rotated densities, overlaps, and Fock matrices need to be constructed. These are computationally intensive operations so any reduction in the number of grid points would significantly reduce the cost of the calculation.

The integration over $SO(3)$ can be broken down to two surface integrals over a 2-sphere S^2 and one over S^1.[299] Lebedev integration grids discretize the surface integral of a 2-sphere and are commonly used when evaluating DFT exchange correlation functionals.[300,301]

$$I[f] = \int_0^{\pi} d\theta \sin(\theta) \int_0^{2\pi} d\phi \, f(\theta, \phi) \tag{5.17}$$

All integration points lie on the surface of a unit sphere and are invariant under the octahedral rotation group with inversion. Lebedev grids are efficient schemes to evaluate surface integrals and can be used to integrate over the α (or γ) and β rotation angles for spin-projected GHF. Compared to the mixed Trapezoid and Gauss-Legendre grid far fewer integration points are required to achieve the same accuracy in spin symmetry restoration. Our implementation uses a Lebedev grid for integration over S^2 and a Trapezoid grid for integration over S^1.

5.4 Results and Discussion

5.4.1 Lebedev Grid

We have compared two different schemes to discretize the spin-projection operator. The first scheme uses a Trapezoid grid for α and γ and a Gauss-Legendre grid for β denoted as TrapGaussLeg(n_α, n_β, n_γ) and the second uses a Lebedev grid for α and β with a Trapezoid grid for γ denoted as LebedevTrap($n_{\alpha\beta}$, n_γ). Table 5.1 shows the error in spin symmetry restoration and the error in the converged energy relative to a denser grid that yields the lowest energy solution. All calculations begin with a converged UHF or GHF solution as the guess for the SGHF calculation. The percent error of $\langle S^2 \rangle$ relative to that of the starting UHF/GHF solution is also included to show what percentage of the starting spin contamination remains.

Molecule	Basis Set	Grid	# Points	$\langle S^2 \rangle$ Error	Remaining Spin Cont.	Energy Error (E_h)
H_3	STO-3G	TrapGaussLeg(2,2,2)	8	8.234×10^{-2}	93.7 %	1.434×10^{-2}
		TrapGaussLeg(6,6,6)	216	3.197×10^{-6}	3.64×10^{-3} %	4.11×10^{-7}
		TrapGaussLeg(10,10,10)	1000	6.725×10^{-13}	7.65×10^{-10} %	
		LebedevTrap(6,4)	24	6.661×10^{-16}	7.58×10^{-13} %	
O_2	6-31G	TrapGaussLeg(10,10,10)	1000	5.869×10^{-12}	4.95×10^{-9} %	
		LebedevTrap(14,6)	84	8.760×10^{-10}	7.79×10^{-7} %	
		LebedevTrap(26,8)	208	-8.882×10^{-16}	7.49×10^{-13} %	

Table 5.1. Error of $\langle S^2 \rangle$ and energy for different integration grids.

Our comparison aims to determine the smallest grid required to restore the desired spin symmetry with an error $< 1.0 \times 10^{-10}$ (the energy convergence criteria in these calculations). In Table 5.1 the largest grid in each category is the smallest grid that meets this criteria. For H_3 the atoms were arranged in an equilateral triangle with 1 Å separation. The broken-symmetry GHF solution has $\langle S^2 \rangle = 0.838$ and spin projection restores the system to doublet symmetry. The O_2 bond length was optimized with UHF and the 6-31G basis set[211] ($\langle S^2 \rangle =$

2.034) using the Gaussian16 software package[302] and the projection operator restores triplet symmetry.

Minimal basis H_3 is an extreme example illustrating the benefit of Lebedev grids. The LebedevTrap(6,4) grid has ∼41.67 times fewer grid points than the TrapGaussLeg(10,10,10) grid, but does a better job of restoring the system to doublet symmetry. Both grids converge to the same energy within the convergence criteria, so no errors are reported. The smaller TrapGaussLeg grids show comparable errors in spin symmetry restoration to that of the converged energy. For O_2 with the 6-31G basis set, ∼4.8 times fewer points are required when using the Lebedev grid, which is more representative of the savings seen in other systems.

There are two notable problems that can arise when the integration grid is not dense enough. The first is that the error in forming the overlap matrix (Eq. (5.10)) may be so great that it is not positive definite making the generalized eigenvalue problem in Equation (5.11) ill-defined. The other problem concerns convergence when the integration error is greater than or comparable to the convergence criteria. Both of these problems present themselves when modeling triplet O_2. The overlap matrix is not positive definite when using the LebedevTrap(6,6) grid although an even smaller grid was successful at restoring spin symmetry for H_3. The three grids presented in Table 5.1 all converge in 12 SCF iterations, but small grids oscillate about the correct energy when the error in symmetry restoration is greater than the convergence criteria. Figure 5.2 shows the convergence behavior for smaller integration grids that did not converge within 200 iterations despite using the same initial guess and optimization scheme as the grids in Table 5.1.

The error in spin symmetry restoration may dictate whether self-consistency can be reached and should be used to determine whether a denser integration grid is necessary. This also means that sparser integration grids can likely be used if the energy convergence criteria is looser. This has implications beyond just spin-projection and should be an important consideration when using other projection operators that require discretization of an integration.

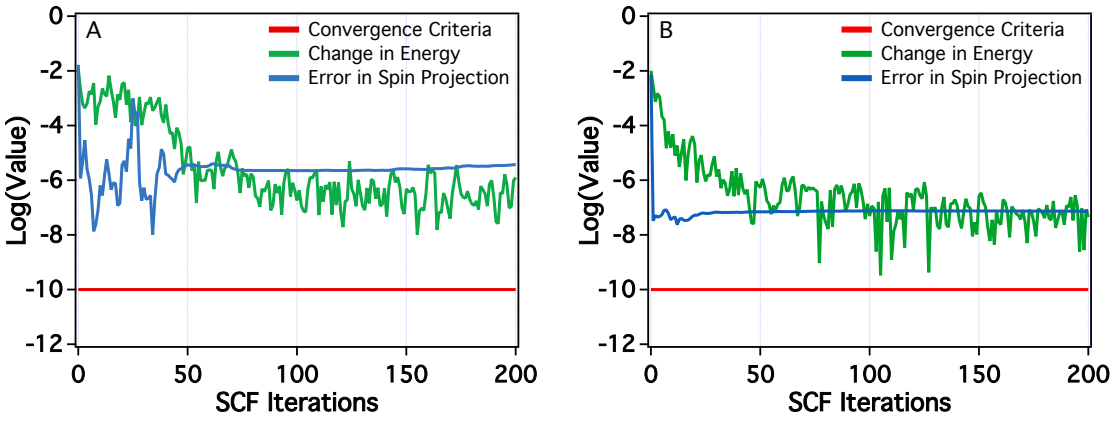

Figure 5.2. SGHF convergence behavior of triplet O_2 modeled with the 6-31G basis set with the TrapGaussLeg(6,6,6) (A) and TrapGaussLeg(8,8,8) (B) grids.

5.4.2 Incremental Fock Build

During the PHF SCF procedure, a rotated Fock matrix needs to be formed at each grid point in the integration over the rotation angles

$$\mathbf{F}[\boldsymbol{\rho}_g] = \mathbf{h} + \mathbf{G}[\boldsymbol{\rho}_g] \tag{5.18}$$

where $\mathbf{h}$ is the core Hamiltonian and $\mathbf{G}[\boldsymbol{\rho}_g]$ is the perturbation tensor defined as

$$(\mathbf{G}[\boldsymbol{\rho}_g])_{ij} = \sum_{kl} \langle ik| \, |jl\rangle \, (\boldsymbol{\rho}_g)_{lk}. \tag{5.19}$$

and $\langle ik| \, |jl\rangle$ are anti-symmetrized two-electron integrals. We can take advantage of the fact that this matrix is linear in the density to more effectively screen two-electron integrals and reduce the cost of forming this matrix.

For ordinary HF, if the two-electron integrals can't be stored in memory (or if writing/reading them from disk is too slow) they can be computed directly at each SCF iteration when forming the perturbation tensor. It is often advantageous to incrementally form the Fock matrix at SCF iteration k as

$$\mathbf{F}[\boldsymbol{\rho}^k] = \mathbf{F}[\boldsymbol{\rho}^{k-1}] + \mathbf{G}[\Delta\boldsymbol{\rho}^k] \tag{5.20}$$

where the change in $\mathbf{G}$ is calculated using the density difference $\Delta\boldsymbol{\rho}^k = \boldsymbol{\rho}^k - \boldsymbol{\rho}^{k-1}$. The two-electron integrals used to form $\mathbf{G}[\Delta\boldsymbol{\rho}^k]$ can be screened more effectively since the density difference should be very small between SCF cycles and will get even smaller as the calculation approaches convergence.[303] The two-electron integrals used to construct $\mathbf{G}$ can be screened using the Schwartz inequality

$$\langle ij \mid kl \rangle \, \rho_{lj} \leq \sqrt{\langle ij \mid ij \rangle} \sqrt{\langle kl \mid kl \rangle} \rho_{lj} \tag{5.21}$$

If the RHS of the above equation is below a particular threshold, then the $\langle ij \mid kl \rangle$ integral does not need to be evaluated. Obviously more integrals will fall below a given threshold and can be screened out if the argument to $\mathbf{G}$ is small.

This same approach can be used to build the rotated Fock matrix in Equation (5.18). All the rotated $\mathbf{G}$ matrices and all the density differences at each integration point can be stored and used to update the rotated Fock matrix during the next SCF cycle. A rotated Fock matrix at SCF cycle k can be calculated as

$$\mathbf{F}[\boldsymbol{\rho}_g^k] = \mathbf{F}[\boldsymbol{\rho}_g^{k-1}] + \mathbf{G}[\Delta\boldsymbol{\rho}_g^k] \tag{5.22}$$

where $\Delta\boldsymbol{\rho}_g^k = \boldsymbol{\rho}_g^k - \boldsymbol{\rho}_g^{k-1}$. It should be noted that storing many rotated matrices every SCF cycle does require a nontrivial amount of memory. However, on modern compute clusters and with the smaller grids presented in the previous section, this likely won't be an issue in most cases. Also this memory requirement is certainly smaller than that required to store all two-electron integrals in-core (the constraint that would prompt one to directly build Fock matrices).

For spin-projected HF, not only should densities be very similar between each SCF iteration, but many of the rotated densities at each SCF iteration should also be very similar to one another. This can be leveraged to screen even more integrals during the construction of each Fock matrix. Rotated Fock matrices can also be built incrementally as

$$\mathbf{F}[\boldsymbol{\rho}_g^k] = \mathbf{F}[\boldsymbol{\rho}_g^{k-1}] + \mathbf{G}[\boldsymbol{\rho}_{g'}^k] - \mathbf{G}[\boldsymbol{\rho}_{g'}^{k-1}] + \mathbf{G}[\Delta\Delta\boldsymbol{\rho}_g^k] \tag{5.23}$$

where g' denotes the previously evaluated grid point before g and the density difference

$$\begin{aligned} \Delta\Delta\boldsymbol{\rho}_g^k &= \Delta\boldsymbol{\rho}_g^k - \Delta\boldsymbol{\rho}_{g'}^k \\ &= (\boldsymbol{\rho}_g^k - \boldsymbol{\rho}_g^{k-1}) - (\boldsymbol{\rho}_{g'}^k - \boldsymbol{\rho}_{g'}^{k-1}) \end{aligned} \tag{5.24}$$

is between two SCF iterations and between two grid points. For this scheme to be advantageous, the rotated density matrices at consecutively evaluated grid points must be very similar. This is not guaranteed to be the case for any random ordering, so the grid points must be sorted to achieve this end. Unfortunately, sorting grid points to be in an optimal ordering is equivalent to solving the NP-hard traveling salesman problem.[304] This is obviously impractical and we have opted to use the greedy nearest neighbor approach to highlight the potential of this approach.[305] After the first SCF iteration, the differences between each rotated density are evaluated and the grid points are reordered to minimize the differences between consecutively evaluate grid points. Future works will attempt more optimal solutions to this problem, but this simple solution is sufficient to showcase the utility of the approach.

We have optimized the SGHF triplet wave function of *p*-benzyne with the STO-3G basis set and the LebedevTrap(50,10) grid using both screening approaches. When using the $\Delta\Delta\boldsymbol{\rho}_g^k$ matrix to incrementally build the Fock matrix we screen either significantly more integrals, a comparable number, or marginally fewer integrals than using $\Delta\boldsymbol{\rho}_g^k$ (Figure 5.3). We have denoted the two approaches as "Delta" density and "Delta-Delta" density screening. At some grid points in the early SCF iterations, twice as many integrals are screened using the Delta-Delta density during the formation of the perturbation tensor. The changes in the number of screened integrals at each grid point also vary more dramatically using the Delta-Delta density. This is due to the particular order in which the grid points are evaluated and would likely change with a more optimal ordering of the grid points. The advantages of this new approach are diminished near convergence where the norm of $\Delta\boldsymbol{\rho}_g^k$ approaches that of $\Delta\Delta\boldsymbol{\rho}_g^k$ and very near convergence these two approaches are comparable in how effectively they screen two-electron integrals. These results suggest that we should expect significant

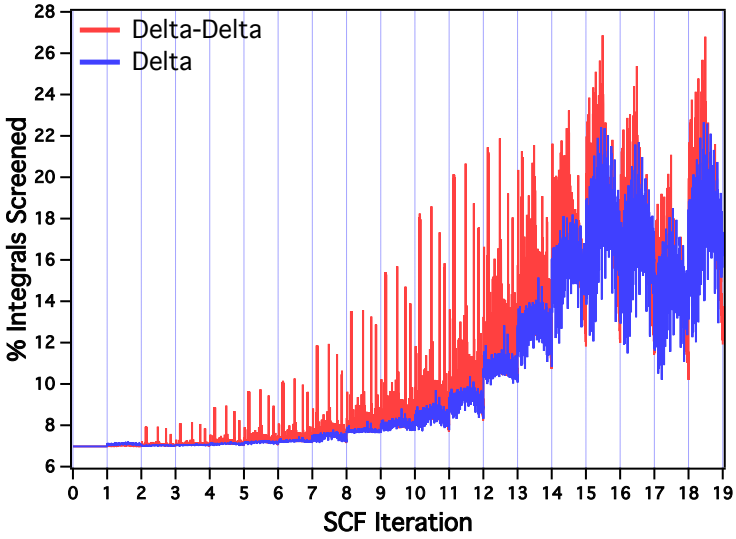

Figure 5.3. The percentage of two-electron integrals screened during the construction of each Fock matrix for triplet p-benzyne using the STO-3G basis and a LebedevTrap(50,10) grid. Using $\Delta\Delta\boldsymbol{\rho}_g^k$ (Delta-Delta) is either significantly better, comparable, or only marginally worse than screening using $\Delta\boldsymbol{\rho}_g^k$ (Delta).

computational savings for larger molecular systems.

5.5 Conclusions

Spin-projected Hartree-Fock is a powerful technique for describing molecular systems with a desired spin symmetry. It retains many of the advantages of broken-symmetry solutions, such as having lower energy than more constrained solutions while also preserving spin as a good quantum number. By projecting out contaminating spin states, this addresses the well-known "symmetry dilemma" and still scales as a mean-field approach.

This work builds off of previous developments from Scuseria and coworkers to develop an efficient scheme to build the effective Fock matrix of spin-projected generalized Hartree-Fock. We have formulated an algorithm that better limits memory usage and forms intermediate matrices not previously discussed in the literature. We also advocate using Lebedev integra-

tion grids to discretize the integration over $SO(3)$ when restoring spin symmetry. Far fewer grid points are required than previously proposed grids to achieve the same accuracy in spin symmetry restoration. Our investigation of different integration grids also revealed that the error in spin symmetry restoration can create a soft bound on the energy convergence. This means that an appropriate integration grid can be determined based on the SCF convergence criteria and this point should also be considered when discretizing integrations in other types of projection operators. We have also presented a novel way to incrementally build rotated Fock matrices in PHF using densities differences between two different SCF iterations and between two grid points. This scheme shows significant improvements in integral screening over just using the density difference between two SCF iterations. These improvements should make it possible to study more complex molecular systems with spin-projected GHF.

BIBLIOGRAPHY

[1] Liang, W.; Fischer, S. A.; Frisch, M. J.; Li, X. Energy-Specific Linear Response TDHF/TDDFT for Calculating High-Energy Excited States. *J. Chem. Theor. Comput.* **2011**, *7*, 3540–3547.

[2] Shelby, M. L.; Lestrange, P. J.; Jackson, N. E.; Haldrup, K.; Mara, M. W.; Stickrath, A. B.; Zhu, D.; Lemke, H.; Chollet, M.; Hoffman, B. M.; Li, X.; Chen, L. X. Ultrafast Excited State Relaxation of a Metalloporphyrin Revealed by Femtosecond X-ray Absorption Spectroscopy. *J. Am. Chem. Soc.* **2016**, *138*, 8752–8764.

[3] Bernadotte, S.; Atkins, A. J.; Jacob, C. R. Origin-independent Calculation of Quadrupole Intensities in X-ray Spectroscopy. *J. Chem. Phys.* **2012**, *137*, 204106.

[4] Roothaan, C. C. J. Self-consistent Field Theory for Open Shells of Electronic Systems. *Rev. Mod. Phys.* **1960**, *32*, 179–185.

[5] Szabo, A.; Ostlund, N. S. *Modern Quantum Chemistry : Introduction to Advanced Electronic Structure Theory*; Dover Publications: Mineola, N.Y., 1996.

[6] Fukutome, H. Unrestricted Hartree–Fock Theory and its Applications to Molecules and Chemical Reactions. *Int. J. Quant. Chem.* **1981**, *20*, 955–1065.

[7] Helgaker, T.; Jørgensen, P.; Olsen, J. *Molecular Electronic-Structure Theory*; John Wiley & Sons, 2002.

[8] Crawford, T. D.; Schaefer III, H. F. *Reviews in Computational Chemistry*; John Wiley & Sons, Inc., 2007; pp 33–136.

[9] Hohenberg, P.; Kohn, W. Inhomogeneous Electron Gas. *Phys. Rev.* **1964**, *136*, B864–B871.

[10] Casida, M. E. *Recent Advances in Density Functional Methods (Part I)*; World Scientific, 1995; pp 155–193.

[11] Stratmann, R. E.; Scuseria, G. E.; Frisch, M. J. An Efficient Implementation of Time-dependent Density-functional Theory for the Calculation of Excitation Energies of Large Molecules. *J. Chem. Phys.* **1998**, *109*, 8218–8224.

[12] Dreuw, A.; Head-Gordon, M. Single-Reference Ab Initio Methods for the Calculation of Excited States of Large Molecules. *Chem. Rev.* **2005**, *105*, 4009–4037.

[13] Schoenlein, R.; Chattopadhyay, S.; Chong, H.; Glover, T.; Heimann, P.; Shank, C.; Zholents, A.; Zolotorev, M. Generation of Femtosecond Pulses of Synchrotron Radiation. *Science* **2000**, *287*, 2237–2240.

[14] Tomov, I. V.; Oulianov, D. A.; Chen, P.; Rentzepis, P. M. Ultrafast Time-Resolved Transient Structures of Solids and Liquids Studied by Means of X-ray Diffraction and EXAFS. *J. Phys. Chem. B* **1999**, *103*, 7081–7091.

[15] Rose-Petruck, C.; Jimenez, R.; Guo, T.; Cavalleri, A.; Siders, C. W.; Rksi, F.; Squier, J. A.; Walker, B. C.; Wilson, K. R.; Barty, C. P. Picosecond–milliångström Lattice Dynamics Measured by Ultrafast X-ray Diffraction. *Nature* **1999**, *398*, 310–312.

[16] Rischel, C.; Rousse, A.; Uschmann, I.; Albouy, P.-A.; Geindre, J.-P.; Audebert, P.; Gauthier, J.-C.; Fröster, E.; Martin, J.-L.; Antonetti, A. Femtosecond Time-resolved X-ray Diffraction from Laser-heated Organic Films. *Nature* **1997**, *390*, 490–492.

[17] Mortensen, D. R.; Seidler, G. T.; Ditter, A. S.; Glatzel, P. Benchtop Nonresonant X-ray Emission Spectroscopy: Coming Soon to Laboratories and XAS Beamlines Near You. J. Phys.: Conf. Ser. 2016; p 012036.

[18] Stöhr, J. *NEXAFS Spectroscopy*; Springer-Verlag, 2003.

[19] Nilsson, A.; Pettersson, L. G. M. Chemical Bonding on Surfaces Probed by X-ray Emission Spectroscopy and Density Functional Theory. *Surf. Sci. Rep.* **2004**, *55*, 49–167.

[20] Kau, L. S.; Spira-Solomon, D. J.; Penner-Hahn, J. E.; Hodgson, K. O.; Solomon, E. I. X-ray Absorption Edge Determination of the Oxidation State and Coordination Number of Copper. Application to the Type 3 Site in *Rhus Vernicifera* Laccase and Its Reaction With Oxygen. *J. Am. Chem. Soc.* **1987**, *109*, 6433–6442.

[21] Hähner, G. Near Edge X-ray Absorption Fine Structure Spectroscopy as a Tool to Probe Electronic and Structural Properties of Thin Organic Films and Liquids. *Chem. Soc. Rev.* **2006**, *35*, 1244–1255.

[22] Lestrange, P. J.; Nguyen, P. D.; Li, X. Calibration of Energy-Specific TDDFT for Modeling K-edge XAS Spectra of Light Elements. *J. Chem. Theor. Comput.* **2015**, *11*, 2994–2999.

[23] Rehr, J. J.; Albers, R. C. Theoretical Approaches to X-ray Absorption Fine Structure. *Rev. Mod. Phys.* **2000**, *72*, 621–654.

[24] Rehr, J. J.; Ankudinov, A. L. Progress in the Theory and Interpretation of XANES. *Coord. Chem. Rev.* **2005**, *249*, 131–140.

[25] Bagus, P. S. Self-consistent-field Wave Functions for Hole States of Some Ne-like and Ar-like Ions. *Phys. Rev.* **1965**, *139*, A619–A634.

[26] Slater, J. C.; Johnson, K. H. Self-consistent-field Xα Cluster Method for Polyatomic Molecules and Solids. *Phys. Rev. B* **1972**, *5*, 844–853.

[27] Triguero, L.; Plashkevych, O.; Pettersson, L.; Ågren, H. Separate State vs. Transition

State Kohn-Sham Calculations of X-ray Photoelectron Binding Energies and Chemical Shifts. *J. Electron. Spectrosc. Relat. Phenom.* **1999**, *104*, 195–207.

[28] Evangelista, F. A.; Shushkov, P.; Tully, J. C. Orthogonality Constrained Density Functional Theory for Electronic Excited States. *J. Phys. Chem. A* **2013**, *117*, 7378–7392.

[29] Derricotte, W. D.; Evangelista, F. A. Simulation of X-ray Absorption Spectra With Orthogonality Constrained Density Functional Theory. *Phys. Chem. Chem. Phys.* **2015**, *17*, 14360–14374.

[30] Stener, M.; Fronzoni, G.; de Simone, M. Time Dependent Density Functional Theory of Core Electrons Excitations. *Chem. Phys. Lett.* **2003**, *373*, 115–123.

[31] Ray, K.; DeBeer George, S.; Solomon, E. I.; Wieghardt, K.; Neese, F. Description of the Ground-State Covalencies of the Bis(dithiolato) Transition-Metal Complexes From X-ray Absorption Spectroscopy and Time-Dependent Density-Functional Calculations. *Chem. Eur. J.* **2007**, *13*, 2783–2797.

[32] Besley, N. A.; Asmuruf, F. A. Time-dependent Density Functional Theory Calculations of the Spectroscopy of Core Electrons. *Phys. Chem. Chem. Phys.* **2010**, *12*, 12024–12039.

[33] Lopata, K.; Van Kuiken, B. E.; Khalil, M.; Govind, N. Linear-Response and Real-Time Time-Dependent Density Functional Theory Studies of Core-Level Near-Edge X-Ray Absorption. *J. Chem. Theor. Comput.* **2012**, *8*, 3284–3292.

[34] Asmuruf, F. A.; Besley, N. A. Time Dependent Density Functional Theory Study of the Near-edge X-ray Absorption Fine Structure of Benzene in Gas Phase and on Metal Surfaces. *J. Chem. Phys.* **2008**, *129*, 064705.

[35] Frisch, M. J.; Trucks, G. W.; Schlegel, H. B.; Scuseria, G. E.; Robb, M. A.; Cheeseman, J. R.; Scalmani, G.; Barone, V.; Petersson, G. A.; Nakatsuji, H.; Li, X.;

Caricato, M.; Marenich, A. V.; Bloino, J.; Janesko, B. G.; Gomperts, R.; Mennucci, B.; Hratchian, H. P.; Ortiz, J. V.; Izmaylov, A. F.; Sonnenberg, J. L.; Williams-Young, D.; Ding, F.; Lipparini, F.; Egidi, F.; Goings, J.; Peng, B.; Petrone, A.; Henderson, T.; Ranasinghe, D.; Zakrzewski, V. G.; Gao, J.; Rega, N.; Zheng, G.; Liang, W.; Hada, M.; Ehara, M.; Toyota, K.; Fukuda, R.; Hasegawa, J.; Ishida, M.; Nakajima, T.; Honda, Y.; Kitao, O.; Nakai, H.; Vreven, T.; Throssell, K.; Montgomery, J. A., Jr.; Peralta, J. E.; Ogliaro, F.; Bearpark, M. J.; Heyd, J. J.; Brothers, E. N.; Kudin, K. N.; Staroverov, V. N.; Keith, T. A.; Kobayashi, R.; Normand, J.; Raghavachari, K.; Rendell, A. P.; Burant, J. C.; Iyengar, S. S.; Tomasi, J.; Cossi, M.; Millam, J. M.; Klene, M.; Adamo, C.; Cammi, R.; Ochterski, J. W.; Martin, R. L.; Morokuma, K.; Farkas, O.; Foresman, J. B.; Fox, D. J. Gaussian Development Version Revision I.10++. Gaussian Inc., Wallingford CT 2016.

[36] Domke, M.; Xue, C.; Puschmann, A.; Mandel, T.; Hudson, E.; Shirley, D. A.; Kaindl, G. Carbon and Oxygen K-edge Photoionization of the CO Molecule. *Chem. Phys. Lett.* **1990**, *173*, 122–128.

[37] Remmers, G.; Domke, M.; Puschmann, A.; Mandel, T.; Xue, C.; Kaindl, G.; Hudson, E.; Shirley, D. High-resolution K-shell Photoabsorption in Formaldehyde. *Phys. Rev. A* **1992**, *46*, 3935–3944.

[38] Tronc, M.; King, G. C.; Read, F. H. Carbon K-shell Excitation in Small Molecules by High-resolution Electron Impact. *J. Phys. B* **1979**, *12*, 137–157.

[39] Shigemasa, E.; Ueda, K.; Sato, Y.; Sasaki, T.; Yagishita, A. Symmetry-resolved K-shell Photoabsorption Spectra of Free N_2 Molecules. *Phys. Rev. A* **1992**, *45*, 2915–2921.

[40] Schirmer, J.; Trofimov, AB,; Randall, K.; Feldhaus, J.; Bradshaw, A.; Ma, Y.; Chen, C.; Sette, F. K-shell Excitation of the Water, Ammonia, and Methane Molecules Using High-resolution Photoabsorption Spectroscopy. *Phys. Rev. A* **1993**, *47*, 1136–1147.

[41] Adachi, J.-i.; Kosugi, N.; Shigemasa, E.; Yagishita, A. Renner–Teller Effect and Rydberg-valence Mixing in the N and O K-edge Photoabsorption Spectra of N_2O. *J. Chem. Phys.* **1995**, *102*, 7369–7376.

[42] Püttner, R.; Dominguez, I.; Morgan, T. J.; Cisneros, C.; Fink, R. F.; Rotenberg, E.; Warwick, T.; Domke, M.; Kaindl, G.; Schlachter, A. S. Vibrationally Resolved O 1s Core-excitation Spectra of CO and NO. *Phys. Rev. A* **1999**, *59*, 3415–3423.

[43] Becke, A. D. A New Mixing of Hartree–Fock and Local Density functional Theories. *J. Chem. Phys.* **1993**, *98*, 1372–1377.

[44] Becke, A. D. Density Functional Thermochemistry. III. The Role of Exact Exchange. *J. Chem. Phys.* **1993**, *98*, 5648–5652.

[45] Stephens, P. J.; Devlin, F. J.; Chabalowski, C. F.; Frisch, M. J. Ab Initio Calculation of Vibrational Absorption and Circular Dichroism Spectra Using Density Functional Force Fields. *J. Phys. Chem.* **1994**, *98*, 11623–11627.

[46] Adamo, C.; Barone, V. Toward Reliable Density Functional Methods Without Adjustable Parameters: The PBE0 Model. *J. Chem. Phys.* **1999**, *110*, 6158–6170.

[47] Perdew, J. P.; Burke, K.; Ernzerhof, M. Generalized Gradient Approximation Made Simple. *Phys. Rev. Lett.* **1996**, *77*, 3865–3868.

[48] Becke, A. D. Density Functional Calculations of Molecular Bond Energies. *J. Chem. Phys.* **1986**, *84*, 4524–4529.

[49] Perdew, J. Density-functional Approximation for the Correlation Energy of the Inhomogeneous Electron Gas. *Phys. Rev. B* **1986**, *33*, 8822–8824.

[50] Heyd, J.; Scuseria, G. E. Efficient Hybrid Density Functional Calculations in Solids: Assessment of the Heyd–Scuseria–Ernzerhof Screened Coulomb Hybrid Functional. *J. Chem. Phys.* **2004**, *121*, 1187–1192.

[51] Heyd, J.; Scuseria, G. E. Assessment and Validation of a Screened Coulomb Hybrid Density Functional. *J. Chem. Phys.* **2004**, *120*, 7274–7280.

[52] Krukau, A. V.; Vydrov, O. A.; Izmaylov, A. F.; Scuseria, G. E. Influence of the Exchange Screening Parameter on the Performance of Screened Hybrid Functionals. *J. Chem. Phys.* **2006**, *125*, 224106.

[53] Vydrov, O. A.; Scuseria, G. E. Assessment of a Long-range Corrected Hybrid Functional. *J. Chem. Phys.* **2006**, *125*, 234109.

[54] McWeeny, R. *Methods of Molecular Quantum Mechanics*, 2nd ed.; Academic Press: London, 1992.

[55] Krishnan, R.; Binkley, J. S.; Seeger, R.; Pople, J. A. Self-consistent Molecular Orbital Methods. XX. A Basis Set for Correlated Wave Functions. *J. Chem. Phys.* **1980**, *72*, 650–654.

[56] Clark, T.; Chandrasekhar, J.; Spitznagel, G. W.; Schleyer, P. v. R. Efficient Diffuse Function-augmented Basis Sets for Anion Calculations. III. The 3-21+G Basis Set for First-row Elements, LiF. *J. Comput. Chem.* **1983**, *4*, 294–301.

[57] Weigend, F.; Ahlrichs, R. Balanced Basis Sets of Split Valence, Triple Zeta Valence and Quadruple Zeta Valence Quality for H to Rn: Design and Assessment of Accuracy. *Phys. Chem. Chem. Phys.* **2005**, *7*, 3297–3305.

[58] Rappoport, D.; Furche, F. Property-optimized Gaussian Basis Sets for Molecular Response Calculations. *J. Chem. Phys.* **2010**, *133*, 134105.

[59] Feller, D. The Role of Databases in Support of Computational Chemistry Calculations. *J. Comput. Chem.* **1996**, *17*, 1571–1586.

[60] Schuchardt, K. L.; Didier, B. T.; Elsethagen, T.; Sun, L.; Gurumoorthi, V.; Chase, J.;

Li, J.; Windus, T. L. Basis Set Exchange: A Community Database for Computational Sciences. *J. Chem. Inf. Model* **2007**, *47*, 1045–1052.

[61] Dunning, T. H. Gaussian Basis Sets for Use in Correlated Molecular Calculations. I. The Atoms Boron Through Neon and Hydrogen. *J. Chem. Phys.* **1989**, *90*, 1007–1023.

[62] Kendall, R. A.; Dunning, T. H.; Harrison, R. J. Electron Affinities of the First-row Atoms Revisited. Systematic Basis Sets and Wave Functions. *J. Chem. Phys.* **1992**, *96*, 6796–6806.

[63] Woon, D. E.; Dunning, T. H. Gaussian Basis Sets for Use in Correlated Molecular Calculations. IV. Calculation of Static Electrical Response Properties. *J. Chem. Phys.* **1994**, *100*, 2975–2988.

[64] Woon, D. E.; Dunning, T. H. Gaussian Basis Sets for Use in Correlated Molecular Calculations. V. Core-valence Basis Sets for Boron Through Neon. *J. Chem. Phys.* **1995**, *103*, 4572–4585.

[65] DeBeer George, S.; Petrenko, T.; Neese, F. Prediction of Iron K-Edge Absorption Spectra Using Time-Dependent Density Functional Theory. *J. Phys. Chem. A* **2008**, *112*, 12936–12943.

[66] Fronzoni, G.; De Francesco, R.; Stener, M. Time Dependent Density Functional Theory of X-ray Absorption Spectroscopy of Alkaline-Earth Oxides. *J. Phys. Chem. B* **2005**, *109*, 10332–10340.

[67] DeBeer George, S.; Petrenko, T.; Neese, F. Time-dependent Density Functional Calculations of Ligand K-edge X-ray Absorption Spectra. *Inorg. Chim. Acta* **2008**, *361*, 965–972.

[68] Song, J.-W.; Watson, M. A.; Nakata, A.; Hirao, K. Core-excitation Energy Calculations With a Long-range Corrected Hybrid Exchange-correlation Functional Including a Short-range Gaussian Attenuation (LCgau-BOP). *J. Chem. Phys.* **2008**, *129*, 184113.

[69] Besley, N. A.; Peach, M. J.; Tozer, D. J. Time-dependent Density Functional Theory Calculations of Near-edge X-ray Absorption Fine Structure With Short-range Corrected Functionals. *Phys. Chem. Chem. Phys.* **2009**, *11*, 10350–10358.

[70] Wiberg, K. B.; de Oliveira, A. E.; Trucks, G. A Comparison of the Electronic Transition Energies for Ethene, Isobutene, Formaldehyde, and Acetone Calculated Using RPA, TDDFT, and EOM-CCSD. Effect of Basis Sets. *J. Phys. Chem. A* **2002**, *106*, 4192–4199.

[71] Caricato, M.; Trucks, G. W.; Frisch, M. J.; Wiberg, K. B. Electronic Transition Energies: A Study of the Performance of a Large Range of Single Reference Density Functional and Wave Function Methods on Valence and Rydberg States Compared to Experiment. *J. Chem. Theor. Comput.* **2010**, *6*, 370–383.

[72] Chen, L. X.; Zhang, X.; Wasinger, E. C.; Attenkofer, K.; Jennings, G.; Muresan, A. Z.; Lindsey, J. S. Tracking Electrons and Atoms in a Photoexcited Metalloporphyrin by X-ray Transient Absorption Spectroscopy. *J. Am. Chem. Soc.* **2007**, *129*, 9616–9618.

[73] Chen, L. X.; Zhang, X.; Wasinger, E. C.; Lockard, J. V.; Stickrath, A. B.; Mara, M. W.; Attenkofer, K.; Jennings, G.; Smolentsev, G.; Soldatov, A. X-ray Snapshots for Metalloporphyrin Axial Ligation. *Chem. Sci.* **2010**, *1*, 642–650.

[74] Alstrum-Acevedo, J. H.; Brennaman, M. K.; Meyer, T. J. Chemical Approaches to Artificial Photosynthesis. 2. *Inorg. Chem.* **2005**, *44*, 6802–6827.

[75] Ardo, S.; Meyer, G. J. Photodriven Heterogeneous Charge Transfer with Transition-metal Compounds Anchored to TiO_2 Semiconductor Surfaces. *Chem. Soc. Rev.* **2009**, *38*, 115–164.

[76] Kalyanasundaram, K.; Grätzel, M. Applications of Functionalized Transition Metal Complexes in Photonic and Optoelectronic Devices. *Coord. Chem. Rev.* **1998**, *177*, 347–414.

[77] Andersson, J.; Puntoriero, F.; Serroni, S.; Yartsev, A.; Pascher, T.; Polıvka, T.; Campagna, S.; Sundström, V. Ultrafast Singlet Energy Transfer Competes with Intersystem Crossing in a Multi-center Transition Metal Polypyridine Complex. *Chem. Phys. Lett.* **2004**, *386*, 336–341.

[78] Benkö, G.; Kallioinen, J.; Korppi-Tommola, J. E.; Yartsev, A. P.; Sundström, V. Photoinduced Ultrafast Dye-to-semiconductor Electron Injection from Nonthermalized and Thermalized Donor States. *J. Am. Chem. Soc.* **2002**, *124*, 489–493.

[79] Diamantis, P.; Gonthier, J. F.; Tavernelli, I.; Rothlisberger, U. Study of the Redox Properties of Singlet and Triplet Tris(2,2'-bipyridine)ruthenium(II) ($[Ru(bpy)_3]^{2+}$) in Aqueous Solution by Full Quantum and Mixed Quantum/Classical Molecular Dynamics Simulations. *J. Phys. Chem. B* **2014**, *118*, 3950–3959.

[80] Henry, W.; Coates, C. G.; Brady, C.; Ronayne, K. L.; Matousek, P.; Towrie, M.; Botchway, S. W.; Parker, A. W.; Vos, J. G.; Browne, W. R.; McGarvey, J. J. The Early Picosecond Photophysics of Ru(II) Polypyridyl Complexes: A Tale of Two Timescales. *J. Phys. Chem. A* **2008**, *112*, 4537–4544.

[81] Shaw, G. B.; Styers-Barnett, D. J.; Gannon, E. Z.; Granger, J. C.; Papanikolas, J. M. Interligand Electron Transfer Dynamics in $[Os(bpy)_3]^{2+}$: Exploring the Excited State Potential Surfaces with Femtosecond Spectroscopy. *J. Phys. Chem. A* **2004**, *108*, 4998–5006.

[82] Yoon, S.; Kukura, P.; Stuart, C. M.; Mathies, R. A. Direct Observation of the Ultrafast Intersystem Crossing in Tris(2,2'-bipyridine) Ruthenium(II) using Femtosecond Stimulated Raman Spectroscopy. *Mol. Phys.* **2006**, *104*, 1275–1282.

[83] Cho, S.; Mara, M. W.; Wang, X.; Lockard, J. V.; Rachford, A. A.; Castellano, F. N.; Chen, L. X. Coherence in Metal–Metal-to-Ligand-Charge-Transfer Excited States of

a Dimetallic Complex Investigated by Ultrafast Transient Absorption Anisotropy. *J. Phys. Chem. A* **2011**, *115*, 3990–3996.

[84] Hua, L.; Iwamura, M.; Takeuchi, S.; Tahara, T. The Substituent Effect on the MLCT Excited State Dynamics of Cu(I) Complexes Studied by Femtosecond Time-resolved Absorption and Observation of Coherent Nuclear Wavepacket Motion. *Phys. Chem. Chem. Phys.* **2015**, *17*, 2067–2077.

[85] Iwamura, M.; Watanabe, H.; Ishii, K.; Takeuchi, S.; Tahara, T. Coherent Nuclear Dynamics in Ultrafast Photoinduced Structural Change of Bis(diimine)copper(I) Complex. *J. Am. Chem. Soc.* **2011**, *133*, 7728–7736.

[86] Mance, J.; Felver, J.; Dexheimer, S. Optical and Acoustic Phonon Dynamics of Exciton Self-Trapping in a Nondegenerate Quasi-One-Dimensional Charge Density Wave System. *J. Phys. Chem. C* **2014**, *118*, 11186–11192.

[87] Rury, A. S.; Sension, R. J. Broadband Ultrafast Transient Absorption of Iron(III) Tetraphenylporphyrin Chloride in the Condensed Phase. *Chem. Phys.* **2013**, *422*, 220–228.

[88] Schrauben, J. N.; Dillman, K. L.; Beck, W. F.; McCusker, J. K. Vibrational Coherence in the Excited State Dynamics of $Cr(acac)_3$: Probing the Reaction Coordinate for Ultrafast Intersystem Crossing. *Chem. Sci.* **2010**, *1*, 405–410.

[89] van der Veen, R. M.; Cannizzo, A.; van Mourik, F.; Vlček Jr, A.; Chergui, M. Vibrational Relaxation and Intersystem Crossing of Binuclear Metal Complexes in Solution. *J. Am. Chem. Soc.* **2010**, *133*, 305–315.

[90] Wächtler, M.; Guthmuller, J.; Kupfer, S.; Maiuri, M.; Brida, D.; Popp, J.; Rau, S.; Cerullo, G.; Dietzek, B. Ultrafast Intramolecular Relaxation and Wave-Packet Motion in a Ruthenium-Based Supramolecular Photocatalyst. *Chem. Eur. J.* **2015**, *21*, 7668–7674.

[91] Zheldakov, I. L.; N. Ryazantsev, M.; Tarnovsky, A. N. Wavepacket Motion via a Conical Intersection in the Photochemistry of Aqueous Transition-metal Dianions. *J. Phys. Chem. Lett.* **2011**, *2*, 1540–1545.

[92] Chen, L.; Zhang, X.; Shelby, M. Recent Advances on Ultrafast X-ray Spectroscopy in the Chemical Sciences. *Chem. Sci.* **2014**, *5*, 4136–4152.

[93] Chen, L. X.; Zhang, X. Photochemical Processes Revealed by X-ray Transient Absorption Spectroscopy. *J. Phys. Chem. Lett.* **2013**, *4*, 4000–4013.

[94] Dell'Angela, M.; Anniyev, T.; Beye, M.; Coffee, R.; Föhlisch, A.; Gladh, J.; Katayama, T.; Kaya, S.; Krupin, O.; LaRue, J.; Møgelhøj, A.; Nordlund, D.; Nørskov, J. K.; berg, H.; Ogasawara, H.; strm, H.; Pettersson, L. G. M.; Schlotter, W. F.; Sellberg, J. A.; Sorgenfrei, F.; Turner, J. J.; Wolf, M.; Wurth, W.; Nilsson, A. Real-time Observation of Surface Bond Breaking with an X-ray Laser. *Science* **2013**, *339*, 1302–1305.

[95] Ferrer, A.; Johnson, J.; Huber, T.; Mariager, S.; Trant, M.; Grübel, S.; Zhu, D.; Chollet, M.; Robinson, J.; Lemke, H.; Ingold, G.; Milne, C.; Staub, U.; Beaud, P.; Johnson, S. L. Nonlinear Delayed Symmetry Breaking in a Solid Excited by Hard X-ray Free Electron Laser Pulses. *Appl. Phys. Lett.* **2015**, *106*, 154101.

[96] Kern, J.; Tran, R.; Alonso-Mori, R.; Koroidov, S.; Echols, N.; Hattne, J.; Ibrahim, M.; Gul, S.; Laksmono, H.; Sierra, R. G.; Gildea, R. J.; Han, G.; Hellmich, J.; Lassalle-Kaiser, B.; Chatterjee, R.; Brewster, A. S.; Stan, C. A.; Glöckner, C.; Lampe, A.; DiFiore, D.; Milathianaki, D.; Fry, A. R.; Seibert, M. M.; Koglin, J. E.; Gallo, E.; Uhlig, J.; Sokaras, D.; Weng, T.-C.; Zwart, P. H.; Skinner, D. E.; Bogan, M. J.; Messerschmidt, M.; Glatzel, P.; Williams, G. J.; Boutet, S.; Adams, P. D.; Zouni, A.; Messinger, J.; Sauter, N. K.; Bergmann, U.; Yano, J.; Yachandra, V. K. Taking Snapshots of Photosynthetic Water Oxidation using Femtosecond X-ray Diffraction and Spectroscopy. *Nat. Chem.* **2014**, *5*, 4371.

[97] Kim, K. H.; Kim, J. G.; Nozawa, S.; Sato, T.; Oang, K. Y.; Kim, T. W.; Ki, H.; Jo, J.; Park, S.; Song, C.; Sato, T.; Ogawa, K.; Togashi, T.; Tono, K.; Yabashi, M.; Ishikawa, T.; Kim, J.; Ryoo, R.; Kim, J.; Ihee, H.; Adachi, S.-i. Direct Observation of Bond Formation in Solution with Femtosecond X-ray Scattering. *Nature* **2015**, *518*, 385–389.

[98] Lemke, H. T.; Bressler, C.; Chen, L. X.; Fritz, D. M.; Gaffney, K. J.; Galler, A.; Gawelda, W.; Haldrup, K.; Hartsock, R. W.; Ihee, H.; Kim, J.; Kim, K. H.; Lee, J. H.; Nielsen, M. M.; Stickrath, A. B.; Zhang, W.; Zhu, D.; Cammarata, M. Femtosecond X-ray Absorption Spectroscopy at a Hard X-ray Free Electron Laser: Application to Spin Crossover Dynamics. *J. Phys. Chem. A* **2013**, *117*, 735–740.

[99] Mitzner, R.; Rehanek, J.; Kern, J.; Gul, S.; Hattne, J.; Taguchi, T.; Alonso-Mori, R.; Tran, R.; Weniger, C.; Schröder, H.; Quevedo, W.; Laksmono, H.; Sierra, R. G.; Han, G.; Lassalle-Kaiser, B.; Koroidov, S.; Kubicek, K.; Schreck, S.; Kunnus, K.; Brzhezinskaya, M.; Firsov, A.; Minitti, M. P.; Turner, J. J.; Moeller, S.; Sauter, N. K.; Bogan, M. J.; Nordlund, D.; Schlotter, W. F.; Messinger, J.; Borovik, A.; Techert, S.; de Groot, F. M. F.; Föhlisch, A.; Erko, A.; Bergmann, U.; Yachandra, V. K.; Wernet, P.; Yano, J. L-Edge X-ray Absorption Spectroscopy of Dilute Systems Relevant to Metalloproteins Using an X-ray Free-Electron Laser. *J. Phys. Chem. Lett.* **2013**, *4*, 3641–3647.

[100] Zhang, W.; Alonso-Mori, R.; Bergmann, U.; Bressler, C.; Chollet, M.; Galler, A.; Gawelda, W.; Hadt, R. G.; Hartsock, R. W.; Kroll, T.; Kjær, K. S.; Kubicek, K.; Lemke, H. T.; Liang, H. W.; Meyer, D. A.; Nielsen, M. M.; Purser, C.; Robinson, J. S.; Solomon, E. I.; Sun, Z.; Sokaras, D.; van Driel, T. B.; Vankó, G.; Weng, T.-C.; Zhu, D.; Gaffney, K. J. Tracking Excited-state Charge and Spin Dynamics in Iron Coordination Complexes. *Nature* **2014**, *509*, 345–348.

[101] Berrah, N.; Bozek, J.; Costello, J.; Düsterer, S.; Fang, L.; Feldhaus, J.; Fukuzawa, H.;

Hoener, M.; Jiang, Y.; Johnsson, P.; Kennedy, E. T.; Meyer, M.; Moshammer, R.; Radcliffe, P.; Richter, M.; Rouzee, A.; Rudenko, A.; Sorokin, A. A.; Tiedtke, K.; Ueda, K.; Ullrich, J.; Vrakking, M. J. J. Non-linear Processes in the Interaction of Atoms and Molecules with Intense EUV and X-ray Fields from SASE Free Electron Lasers (FELs). *J. Mod. Opt.* **2010**, *57*, 1015–1040.

[102] Emma, P.; Akre, R.; Arthur, J.; Bionta, R.; Bostedt, C.; Bozek, J.; Brachmann, A.; Bucksbaum, P.; Coffee, R.; Decker, F. J.; Ding, Y.; Dowell, D.; Edstrom, S.; Fisher, A.; Frisch, J.; Gilevich, S.; Hastings, J.; Hays, G.; Hering, P.; Huang, Z.; Iverson, R.; Loos, H.; Messerschmidt, M.; Miahnahri, A.; Moeller, S.; Nuhn, H. D.; Pile, G.; Ratner, D.; Rzepiela, J.; Schultz, D.; Smith, T.; Stefan, P.; Tompkins, H.; Turner, J.; Welch, J.; White, W.; Wu, J.; Yocky, G.; Galayda, J. First Lasing and Operation of Ångstrom-wavelength Free-electron Laser. *Nat. Phys.* **2010**, *4*, 641–647.

[103] Šesták, Z. Blankenship, RE: Molecular Mechanisms of Photosynthesis. *Photosynthetica* **2002**, *40*, 12–12.

[104] Gust, D.; Moore, T. A.; Moore, A. L. Mimicking Photosynthetic Solar Energy Transduction. *Acc. Chem. Res.* **2001**, *34*, 40–48.

[105] Frauenfelder, H.; McMahon, B.; Fenimore, P. Myoglobin: The Hydrogen Atom of Biology and a Paradigm of Complexity. *Proc. Natl. Acad. Sci. U.S.A.* **2003**, *100*, 8615–8617.

[106] Camilli, A.; Bassler, B. L. Bacterial Small-molecule Signaling Pathways. *Science* **2006**, *311*, 1113–1116.

[107] Rosenthal, J.; Bachman, J.; Dempsey, J. L.; Esswein, A. J.; Gray, T. G.; Hodgkiss, J. M.; Manke, D. R.; Luckett, T. D.; Pistorio, B. J.; Veige, A. S.; Nocera, D. G. Oxygen and Hydrogen Photocatalysis by Two-electron Mixed-valence Coordination Compounds. *Coord. Chem. Rev.* **2005**, *249*, 1316–1326.

[108] Graham, D. J.; Nocera, D. G. Electrocatalytic H_2 Evolution by Proton-Gated Hangman Iron Porphyrins. *Organometallics* **2014**, *33*, 4994–5001.

[109] Yang, J. Y.; Nocera, D. G. Catalase and Epoxidation Activity of Manganese Salen Complexes Bearing Two Xanthene Scaffolds. *J. Am. Chem. Soc.* **2007**, *129*, 8192–8198.

[110] Holten, D.; Bocian, D. F.; Lindsey, J. S. Probing Electronic Communication in Covalently Linked Multiporphyrin Arrays. A Guide to the Rational Design of Molecular Photonic Devices. *Acc. Chem. Res.* **2002**, *35*, 57–69.

[111] Zamyatin, A. V.; Gusev, A. V.; Rodgers, M. A. Two-Pump- One-Probe Femtosecond Studies of Ni(II) Porphyrins Excited States. *J. Am. Chem. Soc.* **2004**, *126*, 15934–15935.

[112] Kim, D.; Kirmaier, C.; Holten, D. Nickel Porphyrin Photophysics and Photochemistry. A Picosecond Investigation of Ligand Binding and Release in the Excited State. *Chem. Phys.* **1983**, *75*, 305–322.

[113] Retsek, J. L.; Drain, C. M.; Kirmaier, C.; Nurco, D. J.; Medforth, C. J.; Smith, K. M.; Sazanovich, I. V.; Chirvony, V. S.; Fajer, J.; Holten, D. Photoinduced Axial Ligation and Deligation Dynamics of Nonplanar Nickel Dodecaarylporphyrins. *J. Am. Chem. Soc.* **2003**, *125*, 9787–9800.

[114] Gentemann, S.; Nelson, N. Y.; Jaquinod, L.; Nurco, D. J.; Leung, S. H.; Medforth, C. J.; Smith, K. M.; Fajer, J.; Holten, D. Variations and Temperature Dependence of the Excited State Properties of Conformationally and Electronically Perturbed Zinc and Free Base Porphyrins. *J. Phys. Chem. B* **1997**, *101*, 1247–1254.

[115] Jia, S.-L.; Jentzen, W.; Shang, M.; Song, X.-Z.; Ma, J.-G.; Scheidt, W. R.; Shelnutt, J. A. Axial Coordination and Conformational Heterogeneity of Nickel(II)

Tetraphenylporphyrin Complexes with Nitrogenous Bases. *Inorg. Chem.* **1998**, *37*, 4402–4412.

[116] Song, Y.; Haddad, R. E.; Jia, S.-L.; Hok, S.; Olmstead, M. M.; Nurco, D. J.; Schore, N. E.; Zhang, J.; Ma, J.-G.; Smith, K. M.; Gazeau, S.; Pécaut, J.; Marchon, J.-C.; Medforth, C. J.; Shelnutt, J. A. Energetics and structural consequences of axial ligand coordination in nonplanar nickel porphyrins. *J. Am. Chem. Soc.* **2005**, *127*, 1179–1192.

[117] Shelnutt, J.; Majumder, S.; Sparks, L.; Hobbs, J.; Medforth, C.; Senge, M.; Smith, K.; Miura, M.; Luo, L.; Quirke, J. Resonance Raman Spectroscopy of Non-planar Nickel Porphyrins. *J. Raman Spectrosc.* **1992**, *23*, 523–529.

[118] Jeong, D. H.; Kim, D.; Cho, D. W.; Jeoung, S. C. Picosecond Transient Resonance Raman Study on the Excited-state Conformational Dynamic of a Highly Ruffled Nickel Porphyrin. *J. Raman Spectrosc.* **2001**, *32*, 487–493.

[119] van Bokhoven, J.; Lamberti, C. *X-ray Absorption and X-ray Emission Spectroscopy: Theory and Applications*; Wiley & Sons: New York, 2015.

[120] Chen, L. X. Probing Transient Molecular Structures with Time-resolved Pump/probe XAFS using Synchrotron X-ray Sources. *J. Electron. Spectrosc. Relat. Phenom.* **2001**, *119*, 161–174.

[121] Katayama, T.; Inubushi, Y.; Obara, Y.; Sato, T.; Togashi, T.; Tono, K.; Hatsui, T.; Kameshima, T.; Bhattacharya, A.; Ogi, Y.; Kurahashi, N.; Misawa, K.; Suzuki, T.; Yabashi, M. Femtosecond X-ray Absorption Spectroscopy with Hard X-ray Free Electron Laser. *Appl. Phys. Lett.* **2013**, *103*, 131105.

[122] Guerra, C. F.; Snijders, J.; Te Velde, G.; Baerends, E. Towards an Order-N DFT Method. *Theor. Chem. Acc.* **1998**, *99*, 391–403.

[123] Te Velde, G.; Bickelhaupt, F. M.; Baerends, E. J.; Fonseca Guerra, C.; van Gisbergen, S. J.; Snijders, J. G.; Ziegler, T. Chemistry With ADF. *J. Comput. Chem.* **2001**, *22*, 931–967.

[124] Patchkovskii, S.; Kozlowski, P. M.; Zgierski, M. Z. Theoretical Analysis of Singlet and Triplet Excited States of Nickel Porphyrins. *J. Chem. Phys.* **2004**, *121*, 1317–1324.

[125] Rassolov, V. A.; Pople, J. A.; Ratner, M. A.; Windus, T. L. 6-31G* Basis Set for Atoms K Through Zn. *J. Chem. Phys.* **1998**, *109*, 1223–1229.

[126] Hariharan, P.; Pople, J. The Influence of Polarization Functions on Molecular Orbital Hydrogenation Energies. *Theor. Chem. Acc.* **1973**, *28*, 213–222.

[127] Chen, L. X.; Jäger, W. J.; Jennings, G.; Gosztola, D. J.; Munkholm, A.; Hessler, J. P. Capturing a Photoexcited Molecular Structure Through Time-Domain X-ray Absorption Fine Structure. *Science* **2001**, *292*, 262–264.

[128] Westre, T. E.; Kennepohl, P.; DeWitt, J. G.; Hedman, B.; Hodgson, K. O.; Solomon, E. I. A Multiplet Analysis of Fe K-edge 1s $\rightarrow$ 3d Pre-edge Features of Iron Complexes. *J. Am. Chem. Soc.* **1997**, *119*, 6297–6314.

[129] Campbell, L.; Tanaka, S.; Mukamel, S. Ligand Effects on the X-ray Absorption of a Nickel Porphyrin Complex: A Simulation Study. *Chem. Phys.* **2004**, *299*, 225–231.

[130] Rodriguez, J.; Holten, D. Ultrafast Vibrational Dynamics of a Photoexcited Metalloporphyrin. *J. Chem. Phys.* **1989**, *91*, 3525–3531.

[131] Gilbert, A. T. B.; Besley, N. A.; Gill, P. M. W. Self-Consistent Field Calculations of Excited States Using the Maximum Overlap Method (MOM). *J. Phys. Chem. A* **2008**, *112*, 13164–13171.

[132] Davidson, E. R. Single-Configuration Calculations on Excited States of Helium. *J. Chem. Phys.* **1964**, *41*, 656–658.

[133] Peng, B.; Kuiken, B. E. V.; Ding, F.; Li, X. A Guided Self-Consistent-Field Method for Excited State Wave Function Optimization: Applications to Ligand Field Transitions in Transition Metal Complexes. *J. Chem. Theor. Comput.* **2013**, *9*, 3933–3938.

[134] Martin, R. L. Natural Transition Orbitals. *J. Chem. Phys.* **2003**, *118*, 4775–4777.

[135] Bacskay, G. B. A Quadratically Convergent Hartree-Fock (QC-SCF) Method. Application to Closed Shell Systems. *Chem. Phys.* **1981**, *61*, 385–404.

[136] Ha-Thi, M.-H.; Shafizadeh, N.; Poisson, L.; Soep, B. First Observation in the Gas Phase of the Ultrafast Electronic Relaxation Pathways of the S_2 States of Heme and Hemin. *Phys. Chem. Chem. Phys.* **2010**, *12*, 14985–14993.

[137] Sorgues, S.; Poisson, L.; Raffael, K.; Krim, L.; Soep, B.; Shafizadeh, N. Femtosecond Electronic Relaxation of Excited Metalloporphyrins in the Gas Ghase. *J. Chem. Phys.* **2006**, *124*, 114302.

[138] Mizutani, Y.; Uesugi, Y.; Kitagawa, T. Intramolecular Vibrational Energy Redistribution and Intermolecular Energy Transfer in the (d,d) Excited State of Nickel Octaethylporphyrin. *J. Chem. Phys.* **1999**, *111*, 8950–8962.

[139] Fadley, C. S.; Hagstrom, S. B. M.; Klein, M. P.; Shirley, D. A. Chemical Effects on Core-Electron Binding Energies in Iodine and Europium. *J. Chem. Phys.* **1968**, *48*, 3779–3794.

[140] Sarangi, R.; DeBeer George, S.; Rudd, D. J.; Szilagyi, R. K.; Ribas, X.; Rovira, C.; Almeida, M.; Hodgson, K. O.; Hedman, B.; Solomon, E. I. Sulfur K-Edge X-ray Absorption Spectroscopy as a Probe of Ligand-Metal Bond Covalency: Metal vs Ligand Oxidation in Copper and Nickel Dithiolene Complexes. *J. Am. Chem. Soc.* **2007**, *129*, 2316–2326.

[141] Gu, W.; Wang, H.; Wang, K. Nickel L-edge and K-edge X-ray Absorption Spectroscopy of Non-innocent Ni$[S_2C_2(CF_3)_2]_2^n$ Series (N = -2, -1, 0): Direct Probe of Nickel Fractional Oxidation State Changes. *Dalton Trans.* **2014**, *43*, 6406–6413.

[142] Peng, B.; Lestrange, P. J.; Goings, J. J.; Caricato, M.; Li, X. Energy-Specific Equation-of-Motion Coupled-Cluster Methods for High-Energy Excited States: Application to K-edge X-ray Absorption Spectroscopy. *J. Chem. Theor. Comput.* **2015**, *11*, 4146–4153.

[143] Monkhorst, H. J. Calculation of Properties With the Coupled-cluster Method. *Int. J. Quant. Chem.* **1977**, *12*, 421–432.

[144] Koch, H.; Jørgensen, P. Coupled Cluster Response Functions. *J. Chem. Phys.* **1990**, *93*, 3333–3344.

[145] Stanton, J. F.; Bartlett, R. J. The Equation of Motion Coupled-cluster Method. A Systematic Biorthogonal Approach to Molecular Excitation Energies, Transition Probabilities, and Excited State Properties. *J. Chem. Phys.* **1993**, *98*, 7029–7039.

[146] Comeau, D. C.; Bartlett, R. J. The Equation-of-motion Coupled-cluster Method. Applications to Open-and Closed-shell Reference States. *Chem. Phys. Lett.* **1993**, *207*, 414–423.

[147] Shavitt, I.; Bartlett, R. J. *Many-Body Methods in Chemistry and Physics*; MBPT and Coupled-Cluster Theory; Cambridge University Press, 2009.

[148] Stanton, J. F.; Gauss, J. Perturbative Treatment of the Similarity Transformed Hamiltonian in Equation-of-motion Coupled-cluster Approximations. *J. Chem. Phys.* **1995**, *103*, 1064–1076.

[149] Goings, J. J.; Caricato, M.; Frisch, M. J.; Li, X. Assessment of Low-scaling Approximations to the Equation of Motion Coupled-Cluster Singles and Doubles Equations. *J. Chem. Phys.* **2014**, *141*, 164116.

[150] Gwaltney, S. R.; Nooijen, M.; Bartlett, R. J. Simplified Methods for Equation-of-motion Coupled-cluster Excited State Calculations. *Chem. Phys. Lett.* **1996**, *248*, 189–198.

[151] Gwaltney, S. R.; Bartlett, R. J. Gradients for the Partitioned Equation-of-motion Coupled-cluster Method. *J. Chem. Phys.* **1999**, *110*, 62–71.

[152] Head-Gordon, M.; Oumi, M.; Maurice, D. Quasidegenerate Second-order Perturbation Corrections to Single-excitation Configuration Interaction. *Mol. Phys.* **1999**, *96*, 593–602.

[153] Trofimov, A. B.; Schirmer, J. An Efficient Polarization Propagator Approach to Valence Electron Excitation Spectra. *J. Phys. B* **1995**, *28*, 2299–2324.

[154] Trofimov, A. B.; Moskovskaya, T. E.; Gromov, E. V.; Vitkovskaya, N. M.; Schirmer, J. Core-level Electronic Spectra in ADC(2) Approximation for Polarization Propagator: Carbon Monoxide and Nitrogen Molecules. *J. Struct. Chem.* **2000**, *41*, 483–494.

[155] Plekan, O.; Feyer, V.; Richter, R.; Coreno, M.; de Simone, M.; Prince, K. C.; Trofimov, A. B.; Gromov, E. V.; Zaytseva, I. L.; Schirmer, J. A Theoretical and Experimental Study of the Near Edge X-ray Absorption Fine Structure (NEXAFS) and X-ray Photoelectron Spectra (XPS) of Nucleobases: Thymine and Adenine. *Chem. Phys.* **2008**, *347*, 360–375.

[156] Cederbaum, L. S.; Domcke, W.; Schirmer, J. Many-body Theory of Core Holes. *Phys. Rev. A* **1980**, *22*, 206–222.

[157] Wenzel, J.; Wormit, M.; Dreuw, A. Calculating X-ray Absorption Spectra of Open-shell Molecules with the Unrestricted Algebraic-diagrammatic Construction Scheme for the Polarization Propagator. *J. Chem. Theor. Comput.* **2014**, *10*, 4583–4598.

[158] Wenzel, J.; Wormit, M.; Dreuw, A. Calculating Core-level Excitations and X-ray Absorption Spectra of Medium-sized Closed-shell Molecules with the Algebraic-diagrammatic Construction Scheme for the Polarization Propagator. *J. Comput. Chem.* **2014**, *35*, 1900–1915.

[159] Foresman, J. B.; Head-Gordon, M.; Pople, J. A.; Frisch, M. J. Toward a Systematic Molecular Orbital Theory for Excited States. *J. Phys. Chem.* **1992**, *96*, 135–149.

[160] Head-Gordon, M.; Rico, R. J.; Oumi, M.; Lee, T. J. A Doubles Correction to Electronic Excited States From Configuration Interaction in the Space of Single Substitutions. *Chem. Phys. Lett.* **1994**, *219*, 21–29.

[161] Asmuruf, F. A.; Besley, N. A. Calculation of Near-edge X-ray Absorption Fine Structure With the CIS(D) Method . *Chem. Phys. Lett.* **2008**, *463*, 267–271.

[162] Nooijen, M.; Bartlett, R. J. Description of Core-excitation Spectra by the Open-shell Electron-attachment Equation-of-motion Coupled Cluster Method. *J. Chem. Phys.* **1995**, *102*, 6735–6756.

[163] Brabec, J.; Bhaskaran-Nair, K.; Govind, N.; Pittner, J.; Kowalski, K. Communication: Application of State-specific Multireference Coupled Cluster Methods to Core-level Excitations. *J. Chem. Phys.* **2012**, *137*, 171101.

[164] Sen, S.; Shee, A.; Mukherjee, D. A Study of the Ionisation and Excitation Energies of Core Electrons Using a Unitary Group Adapted State Universal Approach. *Mol. Phys.* **2013**, *111*, 2625–2639.

[165] Dutta, A. K.; Gupta, J.; Vaval, N.; Pal, S. Intermediate Hamiltonian Fock Space Multireference Coupled Cluster Approach to Core Excitation Spectra. *J. Chem. Theor. Comput.* **2014**, *10*, 3656–3668.

[166] Coriani, S.; Fransson, T.; Christiansen, O.; Norman, P. Asymmetric-Lanczos-Chain-Driven Implementation of Electronic Resonance Convergent Coupled-Cluster Linear Response Theory. *J. Chem. Theor. Comput.* **2012**, *8*, 1616–1628.

[167] Fransson, T.; Coriani, S.; Christiansen, O.; Norman, P. Carbon X-ray Absorption Spectra of Fluoroethenes and Acetone: A Study at the Coupled Cluster, Density Functional, and Static-exchange Levels of Theory. *J. Chem. Phys.* **2013**, *138*, 124311.

[168] Kauczor, J.; Norman, P.; Christiansen, O.; Coriani, S. Communication: A Reduced-space Algorithm for the Solution of the Complex Linear Response Equations Used in Coupled Cluster Damped Response Theory. *J. Chem. Phys.* **2013**, *139*, 211102.

[169] Crawford, T. D.; Schaefer, H. An Introduction to Coupled Cluster Theory for Computational Chemists. *Rev. Comp. Chem.* **2000**, *14*, 33–136.

[170] Löwdin, P. O. Studies in Perturbation Theory: Part I. An Elementary Iteration-variation Procedure for Solving the Schrödinger Equation by Partitioning Technique. *J. Mol. Spectrosc.* **1963**, *10*, 12–33.

[171] Davidson, E. R. The Iterative Calculation of a Few of the Lowest Eigenvalues and Corresponding Eigenvectors of Large Real-symmetric Matrices. *J. Comput. Phys.* **1975**, *17*, 87–94.

[172] Hirao, K.; Nakatsuji, H. A Generalization of the Davidson's Method to Large Nonsymmetric Eigenvalue Problems. *J. Comput. Phys.* **1982**, *45*, 246–254.

[173] Caricato, M.; Trucks, G. W.; Frisch, M. J. A Comparison of Three Variants of the Generalized Davidson Algorithm for the Partial Diagonalization of Large Non-Hermitian Matrices. *J. Chem. Theor. Comput.* **2010**, *6*, 1966–1970.

[174] Rettrup, S. An Iterative Method for Calculating Several of the Extreme Eigensolutions of Large Real Non-symmetric Matrices. *J. Comput. Phys.* **1982**, *45*, 100–107.

[175] Wang, Z.; Tu, Z.; Wang, F. Equation-of-Motion Coupled-Cluster Theory for Excitation Energies of Closed-Shell Systems With Spin!Orbit Coupling. *J. Chem. Theor. Comput.* **2014**, *10*, 5567–5576.

[176] Weigend, F.; Ahlrichs, R. Balanced Basis Sets of Split Valence, Triple Zeta Valence and Quadruple Zeta Valence Quality for H to Rn: Design and Assessment of Accuracy. *Phys. Chem. Chem. Phys.* **2005**, *7*, 3297–3305.

[177] Kauczor, J.; Norman, P.; Christiansen, O.; Coriani, S. Coupled-cluster Response Theory for Near-edge X-ray-absorption Fine Structure of Atoms and Molecules. *Phys. Rev. A* **2012**, *85*, 022507.

[178] Bartlett, R. J.; Stanton, J. F. Applications of Post-Hartree-Fock Methods: A Tutorial. *Rev. Comp. Chem.* **1994**, *5*, 65–169.

[179] Rittby, M.; Bartlett, R. J. An Open-shell Spin-restricted Coupled Cluster Method: Application to Ionization Potentials in Nitrogen. *J. Phys. Chem.* **1988**, *92*, 3033–3036.

[180] Stanton, J. F.; Gauss, J.; Bartlett, R. J. On the Choice of Orbitals for Symmetry Breaking Problems with Application to Nitrogen Oxide (NO_3). *J. Chem. Phys.* **1992**, *97*, 5554–5559.

[181] Hitchcock, A. P.; Brion, C. E. K-shell Excitation Spectra of Carbon Monoxide, Nitrogen, and Oxygen. *J. Electron. Spectrosc. Relat. Phenom.* **1980**, *18*, 1–21.

[182] Ma, Y.; Chen, C. T.; Meigs, G.; Randall, K.; Sette, F. High-resolution K-shell Photoabsorption Measurements of Simple Molecules. *Phys. Rev. A* **1991**, *44*, 1848–1858.

[183] Tronc, M.; King, G. C.; Read, F. H. Nitrogen K-shell Excitation in N_2, NO and N_2O by High-resolution Electron Energy-loss Spectroscopy. *J. Phys. B* **1980**, *13*, 999–1008.

[184] Mijovilovich, A.; Pettersson, L. G. M.; Mangold, S.; Janousch, M.; Susini, J.; Salome, M.; de Groot, F. M. F.; Weckhuysen, B. M. The Interpretation of Sulfur K-Edge

XANES Spectra: A Case Study on Thiophenic and Aliphatic Sulfur Compounds. *J. Phys. Chem. A* **2009**, *113*, 2750–2756.

[185] Lestrange, P. J.; Egidi, F.; Li, X. The Consequences of Improperly Describing Oscillator Strengths Beyond the Electric Dipole Approximation. *J. Chem. Phys.* **2015**, *143*, 234103.

[186] Davidson, E. R. Some Perspectives on Quantum Calculations. *Israel J. Chem.* **1993**, *33*, 243–252.

[187] Jackson, J. D. *Classical Electrodynamics*; Wiley, 1998.

[188] Raab, R. E.; de Lange, O. L. *Multipole Theory In Electromagnetism: Classical, Quantum, And Symmetry Aspects, With Applications*; Oxford University Press, 2005.

[189] Anelli, M.; Jonsson, D.; Fliegl, H.; Ruud, K. The Origin Dependence of the Material Constants: The Permittivity and the Inverse Permeability. *Mol. Phys.* **2015**, *113*, 1–15.

[190] Vidal, L. N.; Egidi, F.; Barone, V.; Cappelli, C. Origin Invariance in Vibrational Resonance Raman Optical Activity. *J. Chem. Phys.* **2015**, *142*, 174101.

[191] List, N. H.; Kauczor, J.; Saue, T.; Jensen, H. J. A.; Norman, P. Beyond the Electric-dipole Approximation: A Formulation and Implementation of Molecular Response Theory for the Description of Absorption of Electromagnetic Field Radiation. *J. Chem. Phys.* **2015**, *142*, 244111.

[192] Cohen, M.; McEachran, R. P.; Rosenthal, D. Length and Velocity Matrix Elements in Quadrupole Transition Calculations (For Transitions in He and Li^+). *J. Phys. B* **1972**, *5*, 184–192.

[193] Alexander, S. A.; Coldwell, R. L. Electric Quadrupole Oscillator Strengths of Helium. *Int. J. Quant. Chem.* **2008**, *108*, 2813–2818.

[194] Bethe, H. A.; Salpeter, E. E. *Quantum Mechanics of One- and Two-electron Atoms*; Academic Press Inc. New York, NY, 1957.

[195] Schatz, G. C.; Ratner, M. A. *Quantum Mechanics in Chemistry*; Dover Publications, 2002.

[196] Ding, F.; Liang, W.; Chapman, C. T.; Isborn, C. M.; Li, X. On the Gauge Invariance of Nonperturbative Electronic Dynamics Using the Time-dependent Hartree-Fock and Time-dependent Kohn-Sham. *J. Chem. Phys.* **2011**, *135*, 164101.

[197] Barron, L. D. *Molecular Light Scattering and Optical Activity*; Cambridge University Press, 2004.

[198] Shulman, R. G.; Yafet, Y.; Eisenberger, P.; Blumberg, W. E. Observation and Interpretation of X-Ray Absorption Edges in Iron Compounds and Proteins. *Proc. Natl. Acad. Sci. U.S.A.* **1976**, *73*, 1384–1388.

[199] Dräger, G.; Frahm, R.; Materlik, G.; Brümmer, O. On the Multipole Character of the X–Ray Transitions in the Pre–Edge Structure of Fe K Absorption Spectra. An Experimental Study. *Phys. Status Solidi B* **1988**, *146*, 287–294.

[200] Yamamoto, T. Assignment of Pre-edge Peaks in K-edge X-ray Absorption Spectra of 3d Transition Metal Compounds: Electric Dipole or Quadrupole? *X-ray Spectrom.* **2008**, *37*, 572–584.

[201] Jacob, C. R.; Reiher, M. Spin in Density-Functional Theory. *Int. J. Quant. Chem.* **2012**, *112*, 3661–3684.

[202] Chandrasekhar, S. On the Continuous Absorption Coefficient of the Negative Hydrogen Ion. *Astrophys. J.* **1945**, *102*, 223–231.

[203] Starace, A. F. Length and Velocity Formulas in Approximate Oscillator-Strength Calculations. *Phys. Rev. A* **1971**, *3*, 1242–1245.

[204] Cohen, M.; McEachran, R. P. Length and Velocity Formulae in Approximate Oscillator Strength Calculations. *Chem. Phys. Lett.* **1972**, *14*, 201–204.

[205] Starace, A. F. Comment on "Length and Velocity Formulas in Approximate Oscillator-Strength Calculations". *Phys. Rev. A* **1973**, *8*, 1141–1142.

[206] Thomas, W. Über die Zahl der Dispersionselektronen, die einem stationren Zustande zugeordnet sind. (Vorläufige Mitteilung). *Naturwissenschaften* **1925**, *13*, 627–627.

[207] Reiche, F.; Thomas, W. Über die Zahl der Dispersionselektronen, die einem stationären Zustand zugeordnet sind. *Z. Phys.* **1925**, *34*, 510–525.

[208] Kuhn, W. Über die Gesamtstärke der von einem Zustande ausgehenden Absorptionslinien. *Z. Phys.* **1925**, *33*, 408–412.

[209] Foresman, J. B.; Head-Gordon, M.; Pople, J. A. Toward a Systematic Molecular Orbital Theory for Excited States. *J. Phys. Chem.* **1992**, *96*, 135–149.

[210] Hirata, S.; Head-Gordon, M. Time-dependent Density Functional Theory Within the Tamm–Dancoff Approximation. *Chem. Phys. Lett.* **1999**, *314*, 291–299.

[211] Hehre, W. J.; Ditchfield, R.; Pople, J. A. Self-Consistent Molecular Orbital Methods. XII. Further Extensions of Gaussian-Type Basis Sets for Use in Molecular Orbital Studies of Organic Molecules. *J. Chem. Phys.* **1972**, *56*, 2257–2261.

[212] Francl, M. M.; Pietro, W. J.; Hehre, W. J.; Binkley, J. S.; Gordon, M. S.; DeFrees, D. J.; Pople, J. A. Self-consistent Molecular Orbital Methods. XXIII. A Polarization-type Basis Set for Second-row Elements. *J. Chem. Phys.* **1982**, *77*, 3654–3665.

[213] Clark, T.; Chandrasekhar, J.; Spitznagel, G. W.; Schleyer, P. V. R. Efficient diffuse function-augmented basis sets for anion calculations. III. The 3-21+G basis set for first-row elements, LiF. *J. Comput. Chem.* **1983**, *4*, 294–301.

[214] McLachlan, A. D.; Ball, M. A. Time-Dependent Hartree–Fock Theory for Molecules. *Rev. Mod. Phys.* **1964**, *36*, 844–855.

[215] Aygül, U.; Batchelor, D.; Dettinger, U.; Yilmaz, S.; Allard, S.; Scherf, U.; Peisert, H.; Chassé, T. Molecular Orientation in Polymer Films for Organic Solar Cells Studied by NEXAFS. *J. Phys. Chem. C* **2012**, *116*, 4870–4874.

[216] Gliboff, M.; Sulas, D.; Nordlund, D.; deQuilettes, D. W.; Nguyen, P. D.; Seidler, G. T.; Li, X.; Ginger, D. S. Direct Measurement of Acceptor Group Localization on DonorAcceptor Polymers Using Resonant Auger Spectroscopy. *J. Phys. Chem. C* **2014**, *118*, 5570–5578.

[217] Parratt, L. G. Electronic Band Structure of Solids by X-ray Spectroscopy. *Rev. Mod. Phys.* **1959**, *31*, 616–645.

[218] DeBeer George, S.; Brant, P.; Solomon, E. I. Metal and Ligand K-Edge XAS of Organotitanium Complexes: Metal 4p and 3d Contributions to Pre-edge Intensity and Their Contributions to Bonding. *J. Am. Chem. Soc.* **2005**, *127*, 667–674.

[219] Casarin, M.; Finetti, P.; Vittadini, A.; Wang, F.; Ziegler, T. Spin-Orbit Relativistic Time-Dependent Density Functional Calculations of the Metal and Ligand Pre-Edge XAS Intensities of Organotitanium Complexes: $TiCl_4$, Ti(η^5-C_5H_5)Cl_3, and Ti(η^5-C_5H_5)$_2Cl_2$. *J. Phys. Chem. A* **2007**, *111*, 5270–5279.

[220] Sørensen, L. K.; Guo, M.; Lindh, R.; Lundberg, M. Applications to Metal K Pre-edges of Transition Metal Dimers Illustrate the Approximate Origin Independence for the Intensities in the Length Representation. *Mol. Phys.* **2016**, 1–16.

[221] Sørensen, L. K.; Guo, M.; Lindh, R.; Lundberg, M. Applications to Metal K pre-edges of Transition Metal Dimers Illustrate the Approximate Origin Independence for the Intensities in the Length Representation. *Mol. Phys.* **2017**, *115*, 174–189.

[222] Krausz, F.; Ivanov, M. Attosecond Physics. *Rev. Mod. Phys.* **2009**, *81*, 163–234.

[223] Salières, P.; Maquet, A.; Haessler, S.; Caillat, J.; Taïeb, R. Imaging Orbitals with Attosecond and Ångström Resolutions: Toward Attochemistry? *Rep. Prog. Phys.* **2012**, *75*, 062401.

[224] Shafir, D.; Soifer, H.; Bruner, B. D.; Dagan, M.; Mairesse, Y.; Patchkovskii, S.; Ivanov, M. Y.; Smirnova, O.; Dudovich, N. Resolving the Time when an Electron Exits a Tunnelling Barrier. *Nature* **2012**, *485*, 343–346.

[225] Ott, C.; Kaldun, A.; Raith, P.; Meyer, K.; Laux, M.; Evers, J.; Keitel, C. H.; Greene, C. H.; Pfeifer, T. Lorentz meets Fano in Spectral Line Shapes: A Universal Phase and its Laser Control. *Science* **2013**, *340*, 716–720.

[226] Orr, B. J.; Ward, J. F. Perturbation Theory of the Non-linear Optical Polarization of an Isolated System. *Mol. Phys.* **1971**, *20*, 513.

[227] Li, X.; Smith, S. M.; Markevitch, A. N.; Romanov, D. A.; Levis, R. J.; Schlegel, H. B. A Time-dependent Hartree-Fock Approach for Studying the Electronic Optical Response of Molecules in Intense Fields. *Phys. Chem. Chem. Phys.* **2005**, *7*, 233–239.

[228] Tussupbayev, S.; Govind, N.; Lopata, K.; Cramer, C. J. Comparison of Real-Time and Linear-Response Time-Dependent Density Functional Theories for Molecular Chromophores Ranging from Sparse to High Densities of States. *J. Chem. Theor. Comput.* **2015**, *11*, 1102–1109.

[229] Goings, J. J.; Li, X. An Atomic Orbital Based Real-time Time-dependent Density Functional Theory for Computing Electronic Circular Dichroism Band Spectra. *J. Chem. Phys.* **2016**, *144*, 234102.

[230] Takimoto, Y.; Vila, F. D.; Rehr, J. J. Real-time Time-dependent Density Functional Theory Approach for Frequency-dependent Nonlinear Optical Response in Photonic Molecules. *J. Chem. Phys.* **2007**, *127*, 154114.

[231] Ding, F.; Kuiken, B. E. V.; Eichinger, B. E.; Li, X. An Efficient Method for Calculating Dynamical Hyperpolarizabilities Using Real-Time Time-Dependent Density Functional Theory. *J. Chem. Phys.* **2013**, *138*, 064104.

[232] Ding, F.; Goings, J. J.; Frisch, M. J.; Li, X. Ab initio Non-relativistic Spin Dynamics. *J. Chem. Phys.* **2014**, *141*, 214111.

[233] Peralta, J. E.; Hod, O.; Scuseria, G. E. Magnetization Dynamics from Time-Dependent Noncollinear Spin Density Functional Theory Calculations. *J. Chem. Theor. Comput.* **2015**, *11*, 3661–3668.

[234] Ding, F.; Chapman, C. T.; Liang, W.; Li, X. Mechanisms of Bridge-mediated Electron Transfer: A TDDFT Electronic Dynamics Study. *J. Chem. Phys.* **2012**, *137*, 22A512.

[235] Petrone, A.; Lingerfelt, D. B.; Rega, N.; Li, X. From Charge-transfer to a Charge-separated State: A Perspective From the Real-Time TDDFT Excitonic Dynamics. *Phys. Chem. Chem. Phys.* **2014**, *16*, 24457–24465.

[236] Thiele, M.; Gross, E. K. U.; Kümmel, S. Adiabatic Approximation in Nonperturbative Time-Dependent Density-Functional Theory. *Phys. Rev. Lett.* **2008**, *100*, 153004.

[237] De Giovannini, U.; Brunetto, G.; Castro, A.; Walkenhorst, J.; Rubio, A. Simulating Pump-Probe Photoelectron and Absorption Spectroscopy on the Attosecond Timescale with Time-Dependent Density Functional Theory. *ChemPhysChem* **2013**, *14*, 1363–1376.

[238] Provorse, M. R.; Habenicht, B. F.; Isborn, C. M. Peak-Shifting in Real-Time Time-Dependent Density Functional Theory. *J. Chem. Theor. Comput.* **2015**, *11*, 4791–4802.

[239] Fischer, S. A.; Cramer, C. J.; Govind, N. Excited State Absorption from Real-Time Time-Dependent Density Functional Theory. *J. Chem. Theor. Comput.* **2015**, *11*, 4294–4303.

[240] Fuks, J. I.; Luo, K.; Sandoval, E. D.; Maitra, N. T. Time-Resolved Spectroscopy in Time-Dependent Density Functional Theory: An Exact Condition. *Phys. Rev. Lett.* **2015**, *114*, 183002.

[241] Greenman, L.; Ho, P. J.; Pabst, S.; Kamarchik, E.; Mazziotti, D. A.; Santra, R. Implementation of the Time-dependent Configuration-interaction Singles Method for Atomic Strong-field Processes. *Phys. Rev. A* **2010**, *82*, 023406.

[242] Krause, P.; Sonk, J. A.; Schlegel, H. B. Strong Field Ionization Rates Simulated with Time-dependent Configuration Interaction and an Absorbing Potential. *J. Chem. Phys.* **2014**, *140*, 174113.

[243] Krause, P.; Klamroth, T.; Saalfrank, P. Molecular Response Properties from Explicitly Time-dependent Configuration Interaction Methods. *J. Chem. Phys.* **2007**, *127*, 034107.

[244] Sonk, J. A.; Caricato, M.; Schlegel, H. B. TD-CI Simulation of the Electronic Optical Response of Molecules in Intense Fields: Comparison of RPA, CIS, CIS(D), and EOM-CCSD. *J. Phys. Chem. A* **2011**, *115*, 4678–4690.

[245] Sonk, J. A.; Schlegel, H. B. TD-CI Simulation of the Electronic Optical Response of Molecules in Intense Fields II: Comparison of DFT Functionals and EOM-CCSD. *J. Phys. Chem. A* **2011**, *115*, 11832–11840.

[246] Luppi, E.; Head-Gordon, M. Computation of High-harmonic Generation Spectra of H_2 and N_2 in Intense Laser Pulses Using Quantum Chemistry Methods and Time-dependent Density Functional Theory. *Mol. Phys.* **2012**, *110*, 909–923.

[247] White, A. F.; Heide, C. J.; Saalfrank, P.; Head-Gordon, M.; Luppi, E. Computation of High-harmonic Generation Spectra of the Hydrogen Molecule using Time-dependent Configuration-interaction. *Mol. Phys.* **2015**, *114*, 947–956.

[248] Miyagi, H.; Madsen, L. B. Time-dependent Restricted-active-space Self-consistent-field Theory for Laser-driven Many-electron Dynamics. II. Extended Formulation and Numerical Analysis. *Phys. Rev. A* **2014**, *89*, 063416.

[249] Handy, N. C. Multi-root Configuration Interaction Calculations. *Chem. Phys. Lett.* **1980**, *74*, 280–283.

[250] Knowles, P. J.; Handy, N. C. A New Determinant-based Full Configuration Interaction Method. *Chem. Phys. Lett.* **1984**, *111*, 315–321.

[251] Olsen, J.; Roos, B. O.; Jørgensen, P.; Jensen, H. J. A. Determinant Based Configuration Interaction Algorithms for Complete and Restricted Configuration Interaction Spaces. *J. Chem. Phys.* **1988**, *89*, 2185–2192.

[252] Hohenstein, E. G.; Luehr, N.; Ufimtsev, I. S.; Martínez, T. J. An Atomic Orbital-based Formulation of the Complete Active Space Self-consistent Field Method on Graphical Processing Units. *J. Chem. Phys.* **2015**, *142*, 224103.

[253] Paldus, J. Group Theoretical Approach to the Configuration Interaction and Perturbation Theory Calculations for Atomic and Molecular Systems. *J. Chem. Phys.* **1974**, *61*, 5321.

[254] Werner, H.-J.; Knowles, P. J. An Efficient Internally Contracted Multiconfiguration–reference Configuration Interaction Method. *J. Chem. Phys.* **1988**, *89*, 5803.

[255] Maurice, D.; Head-Gordon, M. Configuration Interaction with Single Substitutions for Excited States of Open-shell Molecules. *Int. J. Quant. Chem.* **1995**, *29*, 361–370.

[256] Yamaki, D.; Shigeta, Y.; Yamanaka, S.; Nagao, H.; Yamaguchi, K. MP2, TammDancoff, and RPA Methods Based on the Generalized HF Solution. *Int. J. Quant. Chem.* **2000**, *80*, 701–707.

[257] Goings, J. J.; Ding, F.; Davidson, E. R.; Li, X. Approximate Singly Excited States from a Two-component Hartree-Fock Reference. *J. Chem. Phys.* **2015**, *143*, 144106.

[258] Ipatov, A.; Cordova, F.; Doriol, L. J.; Casida, M. E. Excited-state Spin-contamination in Time-dependent Density-functional Theory for Molecules With Open-shell Ground States. *J. Mol. Struct.* **2009**, *914*, 60–73.

[259] Roemelt, M.; Neese, F. Excited States of Large Open-Shell Molecules: An Efficient, General, and Spin-Adapted Approach Based on a Restricted Open-Shell Ground State Wave function. *J. Phys. Chem. A* **2013**, *117*, 3069–3083.

[260] Shavitt, I. Graph Theoretical Concepts for the Unitary Group Approach to the Many-electron Correlation Problem. *Int. J. Quant. Chem.* **1977**, *12*, 131–148.

[261] Shavitt, I. Matrix Element Evaluation in the Unitary Group Approach to the Electron Correlation Problem. *Int. J. Quant. Chem.* **1978**, *14*, 5–32.

[262] Brooks, B. R.; Schaefer III, H. F. The Graphical Unitary Group Approach to the Electron Correlation Problem. Methods and Preliminary Applications. *J. Chem. Phys.* **1979**, *70*, 5092–5106.

[263] Brooks, B. R.; Laidig, W. D.; Saxe, P.; Handy, N. C.; Schaefer III, H. F. The Loop-Driven Graphical Unitary Group Approach: A Powerful Method for the Variational Description of Electron Correlation. *Phys. Scripta* **1980**, *21*, 312–322.

[264] Jiang, W.; Khait, Y. G.; Hoffmann, M. R. Configuration-Driven Unitary Group Approach for Generalized Van Vleck Variant Multireference Perturbation Theory. *J. Phys. Chem. A* **2009**, *113*, 4374–4380.

[265] Leforestier, C.; Bisseling, R. H.; Cerjan, C.; Feit, M. D.; Friesner, R.; Guldberg, A.; Hammerich, A.; Jolicard, G.; Karrlein, W.; Meyer, H.-D.; Lipkin, N.; Roncero, O.; Kosloff, R. A Comparison of Different Propagation Schemes for the Time Dependent Schrödinger Equation. *J. Chem. Phys.* **1991**, *94*, 59–80.

[266] Butcher, P. N.; Cotter, D. *The Elements of Nonlinear Optics*; Cambridge University Press, 1990.

[267] Keldysh, L. V. Ionization in the Field of a Strong Electromagnetic Wave. *Sov. Phys. JETP* **1965**, *20*, 1307–1314.

[268] Aidas, K.; Angeli, C.; Bak, K. L.; Bakken, V.; Bast, R.; Boman, L.; Christiansen, O.; Cimiraglia, R.; Coriani, S.; Dahle, P.; Dalskov, E. K.; Ekström, U.; Enevoldsen, T.; Eriksen, J. J.; Ettenhuber, P.; Fernández, B.; Ferrighi, L.; Fliegl, H.; Frediani, L.; Hald, K.; Halkier, A.; Hättig, C.; Heiberg, H.; Helgaker, T.; Hennum, A. C.; Hettema, H.; Hjertenaes, E.; Høst, S.; Høyvik, I.-M.; Iozzi, M. F.; Jansik, B.; Jensen, H. J. A.; Jonsson, D.; Jørgensen, P.; Kauczor, J.; Kirpekar, S.; Kjaergaard, T.; Klopper, W.; Knecht, S.; Kobayashi, R.; Koch, H.; Kongsted, J.; Krapp, A.; Kristensen, K.; Ligabue, A.; Lutnaes, O. B.; Melo, J. I.; Mikkelsen, K. V.; Myhre, R. H.; Neiss, C.; Nielsen, C. B.; Norman, P.; Olsen, J.; Olsen, J. M. H.; Osted, A.; Packer, M. J.; Pawlowski, F.; Pedersen, T. B.; Provasi, P. F.; Reine, S.; Rinkevicius, Z.; Ruden, T. A.; Ruud, K.; Rybkin, V. V.; Sałek, P.; Samson, C. C. M.; de Merás, A. S.; Saue, T.; Sauer, S. P. A.; Schimmelpfennig, B.; Sneskov, K.; Steindal, A. H.; Sylvester-Hvid, K. O.; Taylor, P. R.; Teale, A. M.; Tellgren, E. I.; Tew, D. P.; Thorvaldsen, A. J.; Thøgersen, L.; Vahtras, O.; Watson, M. A.; Wilson, D. J. D.; Ziolkowski, M.; Ågren, H. The Dalton Quantum Chemistry Program System. *WIREs Comput. Mol. Sci.* **2014**, *4*, 269–284.

[269] Dalton, a Molecular Electronic Structure Program, Release Dalton2016.2 (2016), see http://daltonprogram.org.

[270] Herzberg, G.; Howe, L. L. The Lyman Bands of Molecular Hydrogen. *Can. J. Phys.* **1959**, *37*, 636–659.

[271] Bridge, N. J.; Buckingham, A. D. The Polarization of Laser Light Scattered by Gases. *Proc. Roy. Soc. A* **1966**, *295*, 334–349.

[272] Hasted, J. B. In *Water a Comprehensive Treatise*; Franks, F., Ed.; Plenum, New York, 1972; pp 255–309.

[273] Murphy, W. F. The Rayleigh Depolarization Ratio and Rotational Raman Spectrum of Water Vapor and the Polarizability Components for the Water Molecule. *J. Chem. Phys.* **1977**, *67*, 5877–5882.

[274] Huber, K. P.; Herzberg, G. *Constants of Diatomic Molecules*; Van Nostrand Reinhold, New York, 1979.

[275] Lykos, P.; Pratt, G. W. Discussion on the Hartree-Fock Approximation. *Rev. Mod. Phys.* **1963**, *35*, 496–501.

[276] McDouall, J. J.; Schlegel, H. B. Analytical Gradients for Unrestricted Hartree–Fock and Second Order Møller–Plesset Perturbation Theory with Single Ppin Annihilation. *J. Chem. Phys.* **1989**, *90*, 2363–2369.

[277] Hratchian, H. P. Communication: An Efficient Analytic Gradient Theory for Approximate Spin Projection Methods. *J. Chem. Phys.* **2013**, *138*, 101101.

[278] Thompson, L. M.; Hratchian, H. P. Second Derivatives for Approximate Spin Projection Methods. *J. Chem. Phys.* **2015**, *142*, 054106.

[279] Schlegel, H. B. Potential Energy Curves using Unrestricted Møller–Plesset Perturbation Theory with Spin Annihilation. *J. Chem. Phys.* **1986**, *84*, 4530–4534.

[280] Löwdin, P.-O. Quantum Theory of Many-particle Systems. II. Study of the Ordinary Hartree-Fock Approximation. *Phys. Rev.* **1955**, *97*, 1490–1508.

[281] Mayer, I. The Spin-projected Extended Hartree-Fock Method. *Adv. Quantum Chem.* **1980**, *12*, 189–262.

[282] Scuseria, G. E.; Jiménez-Hoyos, C. A.; Henderson, T. M.; Samanta, K.; Ellis, J. K. Projected Quasiparticle Theory for Molecular Electronic Etructure. *J. Chem. Phys.* **2011**, *135*, 124108.

[283] Jiménez-Hoyos, C. A.; Henderson, T. M.; Tsuchimochi, T.; Scuseria, G. E. Projected Hartree–Fock theory. *J. Chem. Phys.* **2012**, *136*, 164109.

[284] Schmid, K. W.; Grümmer, F.; Faessler, A. Hartree-Fock-Bogoliubov Theory with Spin and Number Projection Before the Variation: An Application to ^{20}Ne and ^{22}Ne. *Nuc. Phys. A* **1984**, 205–229.

[285] Sheikh, J. A.; Ring, P. Symmetry-projected Hartree–Fock–Bogoliubov Equations. *Nuc. Phys. A* **2000**, *665*, 71–91.

[286] Sugimoto, S.; Ikeda, K.; Toki, H. Charge- and Parity-projected Hartree–Fock Method for the Strong Tensor Correlation and its Application to the Alpha Particle. *Nuc. Phys. A* **2004**, *740*, 77–94.

[287] Garza, A. J.; Jiménez-Hoyos, C. A.; Scuseria, G. E. Electronic Correlation without Double Counting via a Combination of Spin Projected Hartree-Fock and Density Functional Theories. *J. Chem. Phys.* **2014**, *140*, 244102.

[288] Wahlen-Strothman, J. M.; Henderson, T. M.; Hermes, M. R.; Degroote, M.; Qiu, Y.; Zhao, J.; Dukelsky, J.; Scuseria, G. E. Merging symmetry projection methods with coupled cluster theory: Lessons from the Lipkin model Hamiltonian. *J. Chem. Phys.* **2017**, *146*, 054110.

[289] Qiu, Y.; Henderson, T. M.; Scuseria, G. E. Projected Hartree-Fock Theory as a Polynomial of Particle-hole Excitations and its Combination with Variational Coupled Cluster Theory. *J. Chem. Phys.* **2017**, *146*, 184105.

[290] Tsuchimochi, T.; Van Voorhis, T. Extended Møller-Plesset perturbation theory for dynamical and static correlations. *J. Chem. Phys.* **2014**, *141*, 164117.

[291] Tsuchimochi, T.; Ten-no, S. Communication: Configuration interaction combined with spin-projection for strongly correlated molecular electronic structures. *J. Chem. Phys.* **2016**, *144*, 011101.

[292] Tsuchimochi, T.; Ten-no, S. Black-Box Description of Electron Correlation with the Spin-Extended Configuration Interaction Model: Implementation and Assessment. *J. Chem. Theor. Comput.* **2016**, *12*, 1741–1759.

[293] Joshi, A. W. *Elements of Group Theory for Physicists*; New Age International, 1997.

[294] Tinkham, M. *Group Theory and Quantum Mechanics*; Courier Corporation, 2003.

[295] Percus, J.; Rotenberg, A. Exact Eigenfunctions of Angular Momentum by Rotational Projection. *J. Math. Phys.* **1962**, *3*, 928–932.

[296] Wigner, E. *Group Theory: And its Application to the Quantum Mechanics of Atomic Spectra*; Academic Press, 1959.

[297] Corbett, J. A Note on Angular Momentum Projection Operators. *Nuc. Phys. A* **1971**, *169*, 426–428.

[298] Li, X.; Valeev, E. F.; Williams-Young, D.; Ding, F.; Liu, H.; Goings, J.; Petrone, A.; Lestrange, P. Chronus Quantum, Beta Version. 2016; `http://www.chronusquantum.org`.

[299] Yershova, A.; Jain, S.; LaValle, S. M.; Mitchell, J. C. Generating Uniform Incremental Grids on $SO(3)$ Using the Hopf Fibration. *Int. J. Rob. Res.* **2010**, *29*, 801–812.

[300] Lebedev, V. I. Values of the Nodes and Weights of Ninth to Seventeenth Order Gauss-Markov Quadrature Formulae Invariant Under the Octahedron Group with Inversion. *USSR Comp. Mat. Mat. Phys.* **1975**, *15*, 44–51.

[301] Becke, A. D. A Multicenter Numerical Integration Scheme for Polyatomic Molecules. *J. Chem. Phys.* **1988**, *88*, 2547–2553.

[302] Frisch, M. J.; Trucks, G. W.; Schlegel, H. B.; Scuseria, G. E.; Robb, M. A.; Cheeseman, J. R.; Scalmani, G.; Barone, V.; Petersson, G. A.; Nakatsuji, H.; Li, X.; Caricato, M.; Marenich, A. V.; Bloino, J.; Janesko, B. G.; Gomperts, R.; Mennucci, B.; Hratchian, H. P.; Ortiz, J. V.; Izmaylov, A. F.; Sonnenberg, J. L.; Williams-Young, D.; Ding, F.; Lipparini, F.; Egidi, F.; Goings, J.; Peng, B.; Petrone, A.; Henderson, T.; Ranasinghe, D.; Zakrzewski, V. G.; Gao, J.; Rega, N.; Zheng, G.; Liang, W.; Hada, M.; Ehara, M.; Toyota, K.; Fukuda, R.; Hasegawa, J.; Ishida, M.; Nakajima, T.; Honda, Y.; Kitao, O.; Nakai, H.; Vreven, T.; Throssell, K.; Montgomery, J. A., Jr.; Peralta, J. E.; Ogliaro, F.; Bearpark, M. J.; Heyd, J. J.; Brothers, E. N.; Kudin, K. N.; Staroverov, V. N.; Keith, T. A.; Kobayashi, R.; Normand, J.; Raghavachari, K.; Rendell, A. P.; Burant, J. C.; Iyengar, S. S.; Tomasi, J.; Cossi, M.; Millam, J. M.; Klene, M.; Adamo, C.; Cammi, R.; Ochterski, J. W.; Martin, R. L.; Morokuma, K.; Farkas, O.; Foresman, J. B.; Fox, D. J. Gaussian 16 Revision A.03. Gaussian Inc. Wallingford CT 2016.

[303] Schwegler, E.; Challacombe, M. Linear Scaling Computation of the Fock Matrix. III. Formation of the Exchange Matrix with Permutational Symmetry. *Theor. Chem. Acc.* **2000**, *104*, 344–349.

[304] Reinelt, G. *The Traveling Salesman: Computational Solutions for TSP Applications*; Springer-Verlag, 1994.

[305] Gutin, G.; Yeo, A.; Zverovich, A. Traveling Salesman Should Not be Greedy: Domination Analysis of Greedy-type Heuristics for the TSP. *Discrete Appl. Math.* **2002**, *117*, 81–86.

[306] Shavitt, I. The Graphical Representation in GUGA. 2005.

Appendix A

INTRODUCTION TO THE GRAPHICAL UNITARY GROUP APPROACH

An introduction to configuration interaction and the nonrelativistic electronic Hamiltonian can be found in Section 4.2.1. This section focuses on the important aspects of the Graphical Unitary Group Approach.

A unitary group $U(n)$ contains all unitary matrices of order n. The set of all CSFs is a basis that can be used to describe the irreducible representation of $U(n)$. The elements of this group can be generated by a finite set of operators called "generators". The excitation operators E_{ij} satisfy the conditions of these generators,[253,306] namely their commutation relationships. We can use the matrix elements of these generators to represent any "particle number conserving operator" in the same basis, such as the spin-independent electronic Hamiltonian.[253]

For GUGA, all the CSFs of a given spin and number of orbitals and electrons are organized in a graph. Every different path that traverses from the top to the bottom of the graph represents a unique CSF. The values for the coupling coefficients are determined by how two paths differ from each other. Their differences form a "loop". There have been several different algorithms used to evaluate these loops.[262,263] They are the CSF, integral, loop, and shape driven methods. They all take advantage of the similarities between the loop shapes in different ways. The following sections will detail the construction of the graph and how the coupling coefficients can be calculated in an efficient manner.

A.0.1 The Distinct Row Table

The distinct row table (DRT) contains all the information about the different CSFs included in the model.[260,261] The graphical component of the technique, introduced by Shavitt, only gives a more convenient manner in which to visualize the DRT. The graph does not introduce any new information. The DRT has several unique sections that will be explained in detail.

A.0.1.1 The Paldus Array

A Paldus array is a 3-column array of non-negative integers.

$$[p] = \begin{bmatrix} a_n & b_n & c_n \\ a_{n-1} & b_{n-1} & c_{n-1} \\ \cdots & \cdots & \cdots \\ a_1 & b_1 & c_1 \\ 0 & 0 & 0 \end{bmatrix} \tag{A.1}$$

It has $n+1$ rows where n is the number of spatial orbitals where the bottom row is just zeros and is referred to as the null row. The a, b, and c values keep track of the number of doubly, singly, and unoccupied orbitals respectively. They also have the property that

$$a_i + b_i + c_i = i \tag{A.2}$$

where i is the orbital number.

The CSF is built from the bottom up and the difference in a, b, and c values between rows determines the occupancy of that orbital. The total number of electrons and spin at any orbital level is determined by

$$2a_i + b_i \quad = N_i \tag{A.3}$$

$$b_i \quad = 2S_i. \tag{A.4}$$

There are only 4 different ways that two rows in the Paldus array can differ from each other assigned the step numbers d: 0-3.

Step number (d)	Δa_i	Δb_i	Δc_i	ΔN_i	ΔS_i
0	0	0	1	0	0
1	0	1	0	1	$\frac{1}{2}$
2	1	-1	1	1	$-\frac{1}{2}$
3	1	0	0	2	0

Table A.1. All possible connections between adjacent Paldus rows.

Cases 0, 1, 2, and 3 relate to unoccupied, singly occupied spin-uncoupled, singly occupied spin-coupled, and doubly occupied orbitals respectively.

The top row of the array defines the electronic state fully in terms of spin and the number of electrons and orbitals. Each CSF with the appropriate spin will have the same top row but will have taken different steps to get there. These different steps just correspond to different orbital occupations. Looking at all possible ways to pass from the null row to this top row using these different cases, there will be many CSFs that have rows in common. Instead of separating each CSF and storing all of their rows, we will instead store only the rows that are "distinct" (Table A.2).

The ways that the different rows can be connected are stored as the downward chaining indices or links. The link index k_{dj} identifies which step number connects a lower row to the current row.

A.0.1.2 Lexical Ordering

The downward counting indices y_{dj} and x_j can be used to assign a sequential index for the different CSFs in the table. All the rows for a certain orbital i are arranged in "lexical order"

i	j	a_j	b_j	c_j	k_{0j}	k_{1j}	k_{2j}	k_{3j}	y_{0j}	y_{1j}	y_{2j}	y_{3j}	x_j	x'_j
6	1	2	1	3	2	3	4	5	0	75	125	170	210	1
5	2	2	1	2	6	7	8	9	0	20	40	55	75	1
	3	2	0	3	7		9	10	0		20	40	50	1
	4	1	2	2	8	9	11	12	0	15	35	39	45	1
	5	1	1	3	9	10	12	13	0	20	30	36	40	1
4	6	2	1	1	14	15	16	17	0	3	9	12	20	1
	7	2	0	2	15		17	18	0		6	14	20	2
	8	1	2	1	16	17	19	20	0	3	11	12	15	2
	9	1	1	2	17	18	20	21	0	8	14	17	20	4
	10	1	0	3	18		21	22	0		6	9	10	2
	11	0	3	1	19	20			0	1			4	1
	12	0	2	2	20	21			0	3			6	2
	13	0	1	3	21	22			0	3			4	1
3	14	2	1	0		23		24		0		1	3	1
	15	2	0	1	23		24	25	0		1	3	6	3
	16	1	2	0		24		26		0		2	3	3
	17	1	1	1	24	25	26	27	0	2	5	6	8	9
	18	1	0	2	25		27	28	0		3	5	6	8
	19	0	3	0		26				0			1	3
	20	0	2	1	26	27			0	1			3	9
	21	0	1	2	27	28			0	2			3	9
	22	0	0	3	28				0				1	3
2	23	2	0	0				29				0	1	4
	24	1	1	0		29		30		0		1	2	16
	25	1	0	1	29		30	31	0		1	2	3	20
	26	0	2	0		30				0			1	24
	27	0	1	1	30	31			0	1			2	35
	28	0	0	2	31				0				1	20
1	29	1	0	0				32				0	1	40
	30	0	1	0		32				0			1	95
	31	0	0	1	32				0				1	75
0	32	0	0	0									1	210

Table A.2. DRT for n=6, N=5, S=1/2.

such that if $j < j'$.

$$a_j > a_{j'} \tag{A.5}$$

or

$$a_j = a_{j'} \quad , b_j > b_{j'}. \tag{A.6}$$

The index x_j is the weight of the row and y_{dj} is the weight of the link at that row. These are computed recursively from the bottom up with $x_j = 1$ for the null row and

$$y_{dj} = 0 \tag{A.7}$$

where k_{dj} is the first existing link for row j,

$$y_{d''j} = y_{d'j} + x_{k_{d'j}} \tag{A.8}$$

where $k_{d'j}$ is the last link preceding link $k_{d''j}$, and

$$x_j = y_{d'''j} + x_{k_{d'''j}} \tag{A.9}$$

where $k_{d'''j}$ is the last link for row j.

The lexical index m for each CSF is determined by adding up all the link weights y_{dj} plus 1. The index is used to keep track of which Hamiltonian matrix element the coupling coefficient should be applied to.

A.0.1.3 Graphical Representation

Shavitt reformed the DRT as a graph in which each node corresponds to a distinct row.[260,261] The lines connecting each node have a slope dependent on the connecting link:

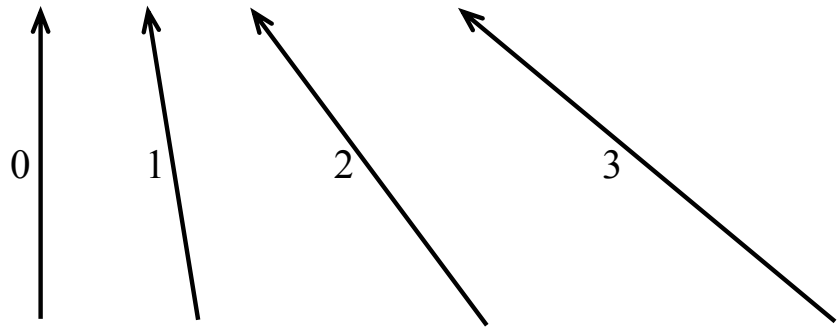

Figure A.1. Slopes for different link types.[306]

Each unique path between the head and tail nodes corresponds to a single CSF (Figure A.2). The graph is often organized such that the doubly occupied orbitals are on the top, the active orbitals are in the middle, and the virtual orbitals are on the bottom.

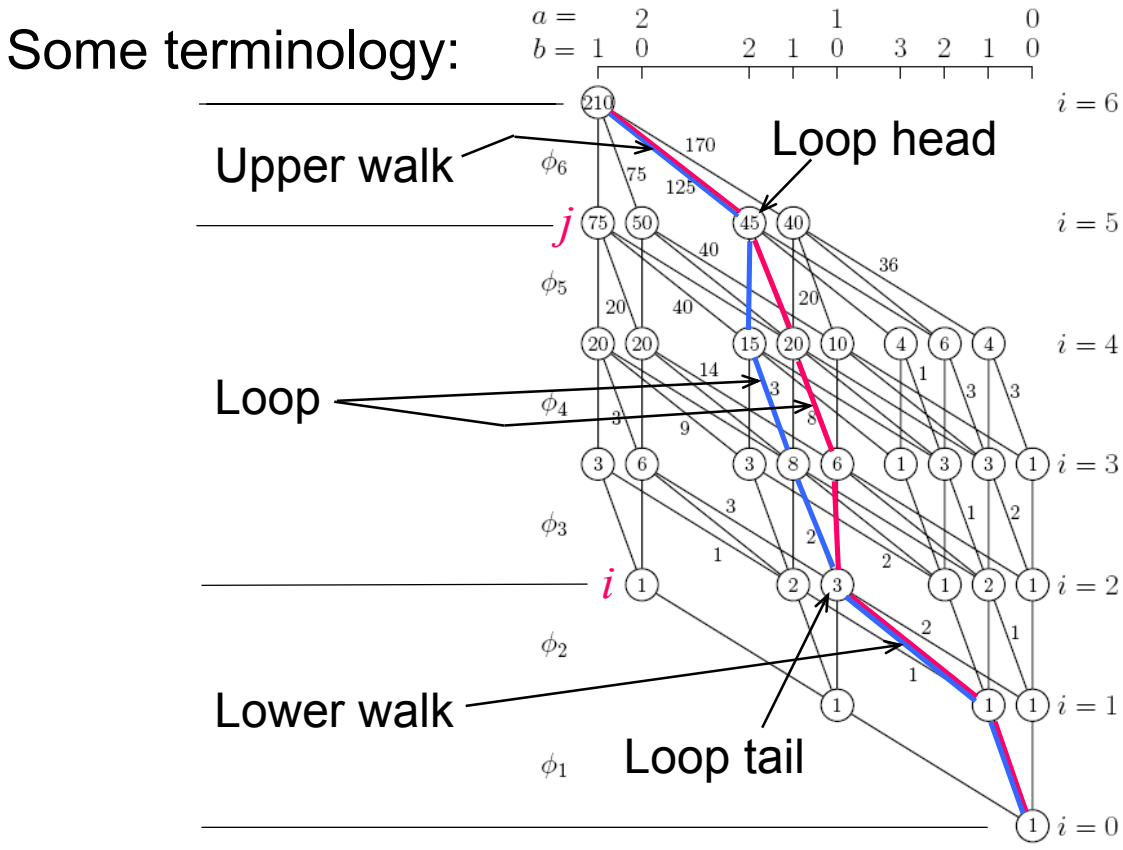

Figure A.2. Graphical representation of the DRT for n=6, N=5, S=1/2.[306]

A.0.2 Evaluating the Matrix Elements

The generator E_{ij} acts on a CSF to promote an electron from orbital j to orbital i. The generator can be a weight generator ($i = j$), a raising generator ($i < j$), or a lowering generator ($i > j$). The values for the coupling coefficients from these generators are all determined by loops formed between CSFs. A loop is defined by the segments where two

CSFs differ (Figure A.2) meaning the orbitals where they have different occupations.

A.0.2.1 One-body generator matrix elements

The loop value can be determined by evaluating the segment value between each orbital level. These different segments are often represented by the function W and the coupling coefficient is the product of each segment value,

$$\langle m'| E_{ij} |m\rangle = \prod_{k=i}^{j} W(T_k, b_k) \tag{A.10}$$

where T_k denotes the segment shape type and b_k is the b value for the m' CSF.

There are only 18 nonzero segment shapes for the one-body generators $\langle m'| E_{ij} |m\rangle$. Any other shapes that can be made are zero valued as the two corresponding CSFs will differ by more than one orbital occupancy.

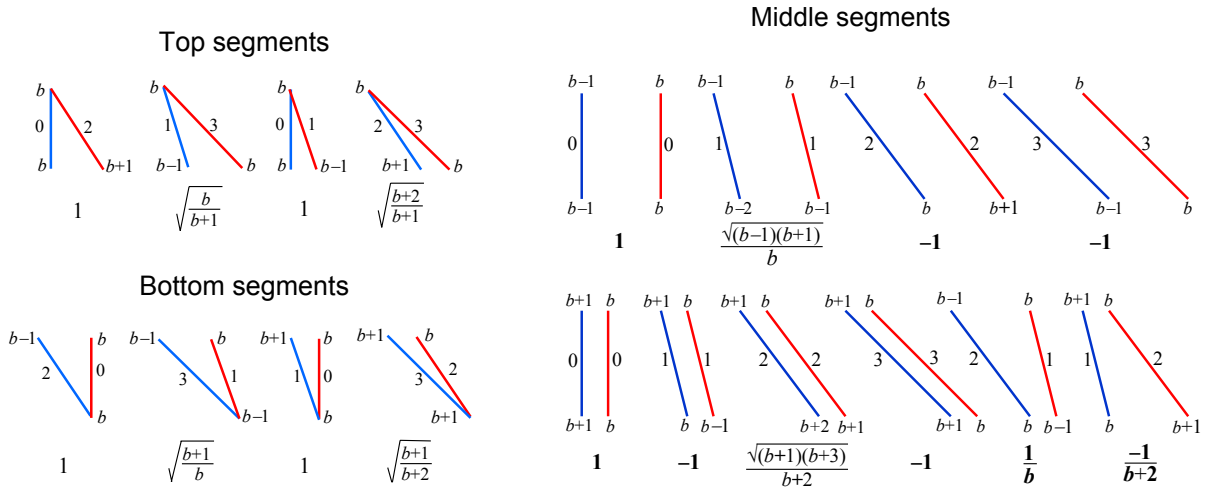

Figure A.3. All nonzero segment shapes for one-body generator matrix elements.[306]

A.0.2.2 Two-body generator matrix elements

For a coupling coefficient that contains the product of two generators a sum over intermediate states is introduced

$$\langle m'| E_{ij}E_{kl} |m\rangle = \sum_{m''} \langle m'| E_{ij} |m''\rangle \langle m''| E_{kl} |m\rangle . \tag{A.11}$$

It can also be written in terms of the different segment values in a similar form to that of the one-body generator

$$\langle m'| e_{ijkl} |m\rangle = \left[\prod_{k \text{ (no overlap)}} W(T_k, b_k) \right] \sum_{X=0,1} \left[\prod_{k \text{ (overlap)}} W(T_k, b_k, X) \right] \tag{A.12}$$

where $X = 0, 1$ either relates to direct and exchange matrix elements[263] or to singlet and triplet coupling[306] depending on what you're reading.

In the no overlap region the segment values are the same as for the one-body generator, but the overlap region must be treated differently. The overlap region is treated implicitly based on the different paths that can be taken by the intermediate states (Figure A.4). The intermediate paths for m'' are never defined at any step.

A.0.3 Loop-driven Method

Any two CSFs that differ by more than 2 orbital occupancies will have a zero Hamiltonian matrix element. Instead of finding all the zero-valued loops, we can just create the loops corresponding to non-zero matrix elements.[262,263]

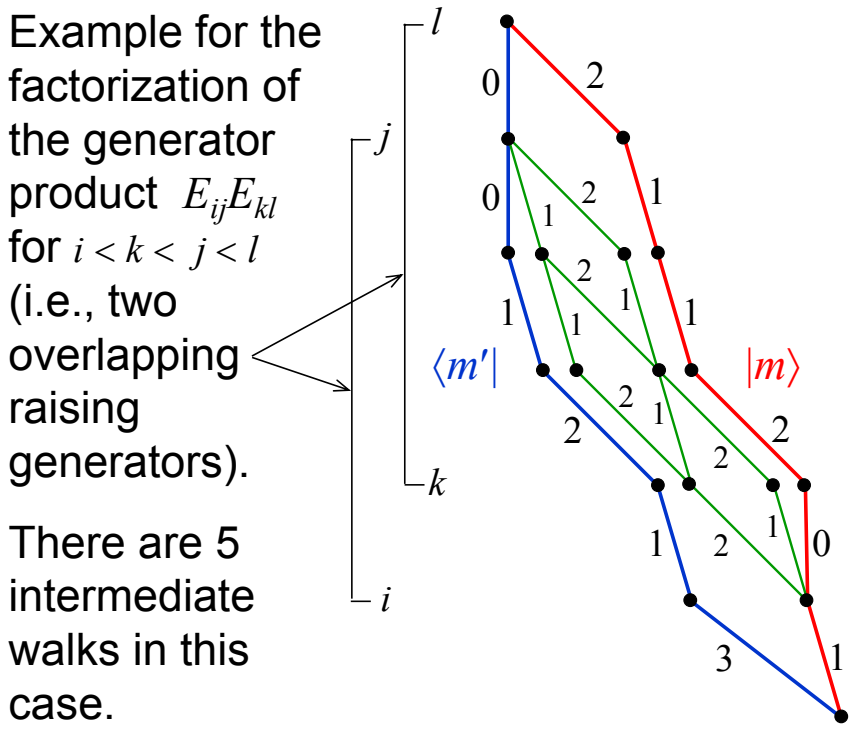

Figure A.4. Graph showing the regions with overlap and no overlap for a two-body generator.[306]

There are 14 different loop types:[262]

$$(1)\ \langle m'|\,(ik|jl)E_{jl}E_{ki} + (ij|kl)E_{kl}E_{ji}\,|m\rangle \qquad (i<j<k<l) \tag{A.13}$$

$$(2)\ \langle m'|\,(il|jk)E_{il}E_{kj} + (ij|kl)E_{kl}E_{ij}\,|m\rangle \qquad (i<j<k<l) \tag{A.14}$$

$$(3)\ \langle m'|\,(ik|jl)E_{jl}E_{ik} + (il|jk)E_{il}E_{jk}\,|m\rangle \qquad (i<j<k<l) \tag{A.15}$$

$$(4)\ \langle m'|\,(ij|jl)E_{jl}E_{ji}\,|m\rangle \qquad (i<j<l) \tag{A.16}$$

$$(5)\ \langle m'|\,(ij|jl)E_{jl}E_{ij} + (jj|il)E_{il}E_{jj}\,|m\rangle \qquad (i<j<l) \tag{A.17}$$

$$(6)\ \langle m'|\,(ij|il)E_{il}E_{ij}\,|m\rangle \qquad (i<j<l) \tag{A.18}$$

$$(7)\ \langle m'|\,(ij|il)E_{il}E_{ji} + (ii|jl)E_{jl}E_{ii}\,|m\rangle \qquad (i<j<l) \tag{A.19}$$

$$(8)\ \langle m'|\,(il|jl)E_{jl}E_{il}\,|m\rangle \qquad (i<j<l) \tag{A.20}$$

$$(9)\ \langle m'|\,(il|jl)E_{jl}E_{li}\,|m\rangle \qquad (i<j<l) \tag{A.21}$$

$$(10)\,\langle m'|\,(il|jl)E_{il}E_{lj} + (ij|ll)E_{ij}E_{ll}\,|m\rangle \qquad (i<j<l) \qquad \text{(A.22)}$$

$$(11)\,\langle m'|\,(il|ll)E_{ll}E_{il} + (ii|il)E_{il}E_{ii} + \left(\langle i|\,h\,|l\rangle - \sum_{a>l}(ia|la)\right)E_{il}\,|m\rangle \qquad (i<l) \qquad \text{(A.23)}$$

$$(12)\,\langle m'|\,(il|il)E_{il}^2/2\,|m\rangle \qquad (i<l) \qquad \text{(A.24)}$$

$$(13)\,\langle m'|\,(il|il)E_{il}E_{li} + (ii|ll)E_{ii}E_{ll}\,|m\rangle \qquad (i<l) \qquad \text{(A.25)}$$

$$(14)\,\langle m'|\,(ll|ll)E_{ll}(E_{ll}-1)/2 + \left(\langle l|\,h\,|l\rangle - \sum_{a>l}(la|la)\right)E_{ll}\,|m\rangle \qquad \text{(A.26)}$$

Several of the loop types have sections in common. For example, types 1-7 are identical between level l and k. Several other loop types have commonality between levels l and j. These similarities can easily be taken advantage of to avoid recalculating segment values.

The loops can also be classified and identified based on the different in orbital occupation between the bra and ket paths (Table A.3).

A.0.3.1 Upper/Lower Walks

For each loop type between 1 and 4 orbital indices are given ($i<j<k<l$). The l level corresponds to the head of the loop and the $i-1$ level is the tail. For each value of l a valid loop is made that connects to every other orbital level. If the loop does not connect to the highest and lowest orbital level, then various "walks" need to be performed.

There are several different CSFs that the found loop can contribute to. Every unique path that connects the loop head to the graph head and every path that connects the loop tail to the graph tail points toward different matrix elements. Once the loop value is determined the lexical index from the different upper and lower walks can be used to determine which matrix elements the found loop will contribute to.

Loop	Δ_l	Δ_k	Δ_j	Δ_i
1	1	-1	-1	1
2	1	-1	1	-1
3	1	1	-1	-1
4	1		-2	1
5	1		0	-1
6	1		1	-2
7	1		-1	0
8	2		-1	-1
9	0		-1	1
10	0		1	-1
11	1			-1
12	2			-2
13	0			0
14	0			

Table A.3. Differences in orbital occupations for the bra and ket paths: $\Delta_x = N_{ket} - N_{bra}$.

Appendix B

DETAILED SPIN-PROJECTED HARTREE-FOCK ALGORITHM

This section provides explicit expressions for all terms presented in Figure 5.1 and walks through each step of the algorithm in detail. This implementation of projected Hartree-Fock requires using matrices in the atomic orbital (AO), orthonormal atomic orbital (OAO), and the natural orbital (NO) bases. Matrices in the OAO basis are denoted with a prime and those in the NO basis have a tilde to differentiate them from AO matrices.

The first step is to combine the grid weights at each integration point with the Wigner D-matrix elements for all necessary spin-projections m and k

$$x(\alpha,\beta,\gamma)_{mk} = G(\alpha,\beta,\gamma)D^{S*}_{mk}(\alpha,\beta,\gamma) \tag{B.1}$$

where $G(\alpha,\beta,\gamma)$ is the weight at a particular grid point. In the following discussion each grid point will be denoted by $g = (\alpha,\beta,\gamma)$. These quantities can be formed once and used throughout the SCF procedure.

The broken-symmetry density must be transformed to the NO basis. The AO density matrix is first transformed to the OAO basis using the transformation matrix $\mathbf{X}$.

$$\boldsymbol{\rho}^{\sigma\tau} = \mathbf{C}^{\sigma}_{occ}\mathbf{C}^{\tau\dagger}_{occ} \tag{B.2}$$

$$\boldsymbol{\rho} = \begin{pmatrix} \boldsymbol{\rho}^{\alpha\alpha} & \boldsymbol{\rho}^{\alpha\beta} \\ \boldsymbol{\rho}^{\beta\alpha} & \boldsymbol{\rho}^{\beta\beta} \end{pmatrix} \tag{B.3}$$

$$\boldsymbol{\rho}' = \begin{pmatrix} \mathbf{X}^{\dagger} & \mathbf{0} \\ \mathbf{0} & \mathbf{X}^{\dagger} \end{pmatrix} \begin{pmatrix} \boldsymbol{\rho}^{\alpha\alpha} & \boldsymbol{\rho}^{\alpha\beta} \\ \boldsymbol{\rho}^{\beta\alpha} & \boldsymbol{\rho}^{\beta\beta} \end{pmatrix} \begin{pmatrix} \mathbf{X} & \mathbf{0} \\ \mathbf{0} & \mathbf{X} \end{pmatrix} \tag{B.4}$$

The OAO density matrix is then diagonalized and the NO transformation matrix $\mathbf{O}$ (formed

from the eigenvectors of the OAO density) is used during the current SCF iteration.

$$\tilde{\boldsymbol{\rho}} = \mathbf{O}^{\dagger}\boldsymbol{\rho}'\mathbf{O} \tag{B.5}$$

$$= \begin{pmatrix} \tilde{\boldsymbol{\rho}}_{oo} & \tilde{\boldsymbol{\rho}}_{ov} \\ \tilde{\boldsymbol{\rho}}_{vo} & \tilde{\boldsymbol{\rho}}_{vv} \end{pmatrix} = \begin{pmatrix} \mathbf{1} & \mathbf{0} \\ \mathbf{0} & \mathbf{0} \end{pmatrix} \tag{B.6}$$

Note that in the AO and OAO bases the density matrix is spin blocked, but in the NO basis it has occupied and virtual blocks.

At this point, we start the loop over all grid points g. The rotation matrix is constructed from three separate matrices defined by each rotation angle. This is trivially done in the OAO basis and then transformed to the NO basis.

$$\mathbf{R}'_g = \mathbf{R}'(\alpha, \hat{S}_z)\mathbf{R}'(\beta, \hat{S}_y)\mathbf{R}'(\gamma, \hat{S}_z) \tag{B.7}$$

$$\mathbf{R}'(\alpha, \hat{S}_z) = \begin{pmatrix} \mathrm{e}^{i\alpha/2}\mathbf{1} & \mathbf{0} \\ \mathbf{0} & \mathrm{e}^{-i\alpha/2}\mathbf{1} \end{pmatrix} \tag{B.8}$$

$$\mathbf{R}'(\beta, \hat{S}_y) = \begin{pmatrix} \cos(\beta/2)\mathbf{1} & \sin(\beta/2)\mathbf{1} \\ -\sin(\beta/2)\mathbf{1} & \cos(\beta/2)\mathbf{1} \end{pmatrix} \tag{B.9}$$

$$\tilde{\mathbf{R}}_g = \mathbf{O}^{\dagger}\mathbf{R}'_g\mathbf{O} \tag{B.10}$$

The overlap between the broken-symmetry determinant and the rotated determinant can now be evaluated using the rotation matrix and the NO density. This can then be used to renormalize the grid weights determined above.

$$\tilde{\mathbf{N}}_g = \left[\begin{pmatrix} \tilde{\boldsymbol{\rho}}_{oo} & \tilde{\boldsymbol{\rho}}_{ov} \end{pmatrix} \tilde{\mathbf{R}}_g \begin{pmatrix} \tilde{\boldsymbol{\rho}}_{oo} \\ \tilde{\boldsymbol{\rho}}_{vo} \end{pmatrix} \right]^{-1} \tag{B.11}$$

$$w_{mk}(g) = x_{mk}(g)/\det(\tilde{\mathbf{N}}_g\tilde{\boldsymbol{\rho}}_{oo}) \tag{B.12}$$

The rotated density matrix in the NO basis can now be constructed.

$$\tilde{\boldsymbol{\rho}}_g = \tilde{\mathbf{R}}_g \begin{pmatrix} \tilde{\boldsymbol{\rho}}_{oo} \\ \tilde{\boldsymbol{\rho}}_{vo} \end{pmatrix} \tilde{\mathbf{N}}_g \begin{pmatrix} \tilde{\boldsymbol{\rho}}_{oo} & \tilde{\boldsymbol{\rho}}_{ov} \end{pmatrix} \tag{B.13}$$

The rotated density matrix is then used to construct the rotated Fock matrix. This must be formed in the AO basis and then transformed back to the NO basis.

$$\boldsymbol{\rho}'_g = \mathbf{O}\tilde{\boldsymbol{\rho}}_g\mathbf{O}^\dagger \tag{B.14}$$

$$\begin{pmatrix} \boldsymbol{\rho}_g^{\alpha\alpha} & \boldsymbol{\rho}_g^{\alpha\beta} \\ \boldsymbol{\rho}_g^{\beta\alpha} & \boldsymbol{\rho}_g^{\beta\beta} \end{pmatrix} = \begin{pmatrix} \mathbf{X} & \mathbf{0} \\ \mathbf{0} & \mathbf{X} \end{pmatrix} \begin{pmatrix} \boldsymbol{\rho}_g^{\prime\alpha\alpha} & \boldsymbol{\rho}_g^{\prime\alpha\beta} \\ \boldsymbol{\rho}_g^{\prime\beta\alpha} & \boldsymbol{\rho}_g^{\prime\beta\beta} \end{pmatrix} \begin{pmatrix} \mathbf{X}^\dagger & \mathbf{0} \\ \mathbf{0} & \mathbf{X}^\dagger \end{pmatrix} \tag{B.15}$$

$$(\mathbf{G}_g^{\sigma\tau})_{ij} = \delta_{\sigma\tau}\sum_{kl}\langle ik \mid jl\rangle\left((\boldsymbol{\rho}_g^{\alpha\alpha})_{lk} + (\boldsymbol{\rho}_g^{\beta\beta})_{lk}\right) - \sum_{kl}\langle ik \mid lj\rangle\,(\boldsymbol{\rho}_g^{\sigma\tau})_{lk} \tag{B.16}$$

$$\mathbf{G}'_g = \begin{pmatrix} \mathbf{X}^\dagger & \mathbf{0} \\ \mathbf{0} & \mathbf{X}^\dagger \end{pmatrix} \begin{pmatrix} \mathbf{G}_g^{\alpha\alpha} & \mathbf{G}_g^{\alpha\beta} \\ \mathbf{G}_g^{\beta\alpha} & \mathbf{G}_g^{\beta\beta} \end{pmatrix} \begin{pmatrix} \mathbf{X} & \mathbf{0} \\ \mathbf{0} & \mathbf{X} \end{pmatrix} \tag{B.17}$$

$$\tilde{\mathbf{G}}_g = \mathbf{O}^\dagger\mathbf{G}'_g\mathbf{O} \tag{B.18}$$

$$\tilde{\mathbf{F}}_g = \tilde{\mathbf{h}} + \tilde{\mathbf{G}}_g \tag{B.19}$$

We now have all the necessary quantities to build the CI matrix elements by looping over the different spin projections m, k. Note that this step is not necessary for singlet states since the spin projection is always 0. We can update S_{mk}, H_{mk}, $\boldsymbol{\mathfrak{X}}_{mk}$, and $\boldsymbol{\mathfrak{F}}_{mk}$ for the current grid point.

$$S_{mk} \mathrel{+}= w_{mk}(g) \tag{B.20}$$

$$H_{mk} \mathrel{+}= \frac{1}{2}w_{mk}(g)\left[\mathrm{Tr}[(\tilde{\mathbf{h}} + \tilde{\mathbf{F}}_g)\tilde{\boldsymbol{\rho}}_g]\right] \tag{B.21}$$

$$\tilde{\boldsymbol{\mathfrak{X}}}_{mk} \mathrel{+}= w_{mk}(g)\tilde{\mathbf{X}}_g \tag{B.22}$$

$$\tilde{\mathbf{X}}_g = \tilde{\mathbf{R}}_g \begin{pmatrix} \tilde{\boldsymbol{\rho}}_{oo} \\ \tilde{\boldsymbol{\rho}}_{vo} \end{pmatrix} \tilde{\mathbf{N}}_g + \tilde{\mathbf{N}}_g \begin{pmatrix} \tilde{\boldsymbol{\rho}}_{oo} & \tilde{\boldsymbol{\rho}}_{ov} \end{pmatrix} \tilde{\mathbf{R}}_g \tag{B.23}$$

$$\tilde{\boldsymbol{\mathfrak{F}}}_{mk} \mathrel{+}= w_{mk}(g)\tilde{\boldsymbol{\mathcal{F}}}_g \tag{B.24}$$

$$\begin{aligned} \tilde{\boldsymbol{\mathcal{F}}}_g = {} & \frac{1}{2}\tilde{\mathbf{X}}_g\mathrm{Tr}[(\tilde{\mathbf{h}} + \tilde{\mathbf{F}}_g)\tilde{\boldsymbol{\rho}}_g] + \tilde{\mathbf{N}}_g \begin{pmatrix} \tilde{\boldsymbol{\rho}}_{oo} & \tilde{\boldsymbol{\rho}}_{ov} \end{pmatrix} \tilde{\mathbf{F}}_g(\mathbf{1} - \tilde{\boldsymbol{\rho}}_g)\tilde{\mathbf{R}}_g \\ & + (\mathbf{1} - \tilde{\boldsymbol{\rho}}_g)\tilde{\mathbf{F}}_g\tilde{\mathbf{R}}_g \begin{pmatrix} \tilde{\boldsymbol{\rho}}_{oo} \\ \tilde{\boldsymbol{\rho}}_{vo} \end{pmatrix} \tilde{\mathbf{N}}_g \end{aligned} \tag{B.25}$$

The CI problem can now be solved to obtain the linear coefficients and energy. These can then be contracted with $\boldsymbol{\mathfrak{X}}_{mk}$ and $\boldsymbol{\mathfrak{F}}_{mk}$ to finish forming the effective Fock matrix

$$\mathbf{Hf} = \mathbf{Sf}E^S \tag{B.26}$$

$$\tilde{\boldsymbol{\mathcal{F}}} = \sum_{mk} f_m^* f_k \left(\tilde{\boldsymbol{\mathfrak{F}}}_{mk} - E^S \tilde{\boldsymbol{\mathfrak{X}}}_{mk} \right) \tag{B.27}$$

The occupied-occupied and virtual-virtual blocks of the effective Fock matrix are always $\mathbf{0}$ and at convergence the off-diagonal blocks vanish as well due to the Brillouin condition (Equation (5.12)). To ensure smooth convergence and separation of the occupied and virtual spaces, the diagonal blocks of the effective Fock matrix can be modified to use the blocks of the broken-symmetry Fock matrix. The choice was proposed by Scuseria and coworkers and has proven to be effective in practice.

$$\tilde{\boldsymbol{\mathcal{F}}} = \begin{pmatrix} \mathbf{0} & \tilde{\boldsymbol{\mathcal{F}}}_{ov}^{PHF} \\ \tilde{\boldsymbol{\mathcal{F}}}_{vo}^{PHF} & \mathbf{0} \end{pmatrix} \rightarrow \begin{pmatrix} \tilde{\mathbf{F}}_{oo}^{GHF} & \tilde{\boldsymbol{\mathcal{F}}}_{ov}^{PHF} \\ \tilde{\boldsymbol{\mathcal{F}}}_{vo}^{PHF} & \tilde{\mathbf{F}}_{vv}^{GHF} \end{pmatrix} \tag{B.28}$$

The effective Fock matrix can then be transformed to the OAO basis, diagonalized, and convergence evaluated. If the system has not converged, we return to the step where the broken-symmetry density is transformed to the NO basis and proceed through the other steps.